ALTERNATING SSFP PERMITS RAPID, BANDING-ARTIFACT-FREE BALANCED SSFP FMRI

by

Steve Patterson

Submitted in partial fulfillment of the
requirements for the degree of
Doctor of Philosophy

at

Dalhousie University
Halifax, Nova Scotia
December 2013

Table of Contents

List of Tables . . . . . **vi**

List of Figures . . . . . **vii**

Abstract . . . . . **x**

List of Abbreviations and Symbols Used . . . . . **xi**

Acknowledgements . . . . . **xv**

Chapter 1 Introduction **1**

1.1 Functional Magnetic Resonance Imaging 1

1.2 Limitations of Conventional fMRI 2

1.3 Approaches to Overcome the Limitations of Conventional fMRI . . . 2
1.3.1 Mitigating Signal Dropout in GRE fMRI 2
1.3.2 Alternatives to GRE for fMRI 5

1.4 Project Overview and Hypothesis 10
1.4.1 Thesis Outline 11

1.5 Contributions to Research 11

Chapter 2 Background: Magnetic Resonance Imaging (MRI) . . . **13**

2.1 Overview 13

2.2 Spin and the Magnetic Moment of the Proton 13

2.3 Equilibrium Magnetization 14

2.4 Semi-Classical Equations of Motion 16

2.5 Excitation 17
2.5.1 The Rotating Reference Frame 18

2.6 Signal Detection 19

2.7 Relaxation 21
2.7.1 Spin-lattice relaxation 21
2.7.2 Spin-spin relaxation 23

2.7.3 Relaxation due to macroscopic magnetic field inhomogeneities . . . 24

2.8 The Bloch Equations . . . 24
2.8.1 Piecewise solution of the Bloch equations . . . 25

2.9 Basic Pulse Sequences . . . 26
2.9.1 Free Induction Decay . . . 26
2.9.2 The Spin-Echo . . . 27

2.10 Selective Excitation . . . 30
2.10.1 Selective Excitation: Theory . . . 30

2.11 Imaging . . . 33

2.12 Balanced Steady State Free Precession . . . 38
2.12.1 Derivation of the b-SSFP Signal Equations . . . 40
2.12.2 Phase Cycling . . . 42
2.12.3 The Approach to Steady State . . . 45

Chapter 3 Background: functional Magnetic Resonance Imaging (fMRI) . . . 49

3.1 The BOLD Effect . . . 49

3.2 BOLD Contrast Mechanisms . . . 50

3.3 The Temporal Resolution of BOLD . . . 55

3.4 The Spatial Resolution of BOLD . . . 57

3.5 The Optimum T_E for GRE and SE fMRI . . . 61

3.6 Overview of fMRI Analysis . . . 62

3.7 Balanced SSFP fMRI . . . 63

Chapter 4 Theoretical Modeling . . . 68

4.1 Introduction . . . 68

4.2 Methods . . . 69
4.2.1 Monte Carlo Simulations . . . 69
4.2.2 RF catalyzation . . . 71
4.2.3 Pulse Sequences . . . 71

4.3 Results . . . 74
4.3.1 Bloch Simulations . . . 74

4.3.2 Monte Carlo Simulations . . . 77

4.4 Discussion . . . 80
4.4.1 Signal vs. BOLD Contrast Behavior . . . 80
4.4.2 Recommended Implementation . . . 80
4.4.3 Drawbacks . . . 82
4.4.4 Model Limitations . . . 82
4.4.5 Conclusion . . . 83

Chapter 5 Experimental Confirmation of Alternating SSFP Signal Behavior . . . 84

5.1 Introduction . . . 84

5.2 Methods . . . 84
5.2.1 Equipment . . . 84
5.2.2 Pulse sequences . . . 84
5.2.3 Phantom Measurements . . . 86
5.2.4 Human Images . . . 86
5.2.5 SNR . . . 86

5.3 Results . . . 87
5.3.1 Signal timecourses . . . 87
5.3.2 Images . . . 87

5.4 Discussion . . . 87
5.4.1 Conclusion . . . 91

Chapter 6 Rat Hypercapnia Studies . . . 92

6.1 Introduction . . . 92

6.2 Methods . . . 93
6.2.1 Alternating and balanced SSFP sequences . . . 93
6.2.2 Acquisition . . . 95
6.2.3 Analysis . . . 96

6.3 Results . . . 99

6.4 Discussion . . . 103
6.4.1 Comparison with Monte Carlo Simulations . . . 103
6.4.2 Alternating SSFP vs. balanced SSFP . . . 104
6.4.3 Conclusion . . . 105

Chapter 7 Human Studies . . . 106

7.1 Introduction . . . 106

7.2 Methods . . . 107
7.2.1 Data Acquisition . . . 107
7.2.2 Data Analysis . . . 108

7.3 Results . . . 112
7.3.1 Individual- and Group-level Activation Maps . . . 112
7.3.2 Alternating SSFP vs. balanced SSFP in the Occipital ROI . . . 112
7.3.3 Alternating SSFP vs. balanced SSFP in the Stop-band ROI . . . 115

7.4 Discussion . . . 116
7.4.1 Conclusion . . . 119

Chapter 8 Future Work and Conclusion . . . 120

8.1 Future Work . . . 120
8.1.1 Suppression of Fat Signal . . . 120
8.1.2 Eddy-current reduction with segmented EPI . . . 121
8.1.3 Acceleration . . . 121
8.1.4 BOLD contrast maximization with a variable flip angle scheme . . . 124

8.2 Conclusion . . . 124

Appendix A . . . 126

A.1 Alternating SSFP Contrast Growth . . . 126

Bibliography . . . 127

List of Tables

Table 3.1 PSF of BOLD fMRI 59

Table 6.1 Acquisition parameters - rat hypercapnia study 96
Table 6.2 Summary statistics - rat hypercapnia study 103

Table 7.1 Summary statistics - human study - occipital ROI (ind.) 115
Table 7.2 Summary statistics - human study - occipital ROI (group) . . . 116
Table 7.3 Summary statistics - human study - stop-band ROI 117

List of Figures

Figure 1.1 Off-resonance frequency map 3

Figure 1.2 Signal dropout in GRE fMRI 4

Figure 1.3 Banding artifacts in pass-band SSFP 7

Figure 1.4 Two-acquisition pass-band SSFP fMRI 8

Figure 1.5 The transition between steady states 9

Figure 2.1 Precession 17

Figure 2.2 Magnetization trajectory during an RF pulse 19

Figure 2.3 Magnetization relaxation following a 90° RF pulse 22

Figure 2.4 FID signal and frequency spectrum 27

Figure 2.5 Isochromat behavior during a spin-echo sequence 29

Figure 2.6 Slice selection 31

Figure 2.7 Slice selection refocus gradient 33

Figure 2.8 k-space sampling requirements 35

Figure 2.9 Properties of **k**-space 36

Figure 2.10 3D GRE-EPI pulse sequence 37

Figure 2.11 2D balanced SSFP pulse sequence 38

Figure 2.12 SNR-efficiency: SSFP vs. SPGR 39

Figure 2.13 Signal vs. off-resonance frequency for SSFP and SPGR 39

Figure 2.14 Balanced SSFP signal magnitude and phase 43

Figure 2.15 Maximum intensity projection (MIP) 44

Figure 2.16 Signal behaviour during the approach to steady state 46

Figure 2.17 Effect of signal oscillations on point spread function 47

Figure 2.18 Balanced SSFP catalyzation pulse sequences 48

Figure 3.1 Local coordinate system for a cylindrical field perturber 52

Figure 3.2 The magnetic field offset surrounding a cylinder 53
Figure 3.3 The canonical hemodynamic response function 56
Figure 3.4 Tissue and vascular contributions to SE BOLD signal 59
Figure 3.5 Tissue and vascular contributions to GRE BOLD signal 60
Figure 3.6 Techniques for fMRI using balanced SSFP 65

Figure 4.1 Alternating SSFP pulse sequence schematic 72
Figure 4.2 Alternating SSFP signal timecourses: Bloch simulations 75
Figure 4.3 Alternating SSFP signal timecourses: MC simulations 76
Figure 4.4 Alternating SSFP contrast timecourses: MC simulations . . . 78
Figure 4.5 Alternating SSFP image combination strategies 79

Figure 5.1 Alternating SSFP pulse sequence diagram: 4 T 85
Figure 5.2 Alternating SSFP signal timecourses: phantom 88
Figure 5.3 Phantom images: alternating vs. pass-band SSFP 89
Figure 5.4 Human images: alternating vs. pass-band SSFP 89
Figure 5.5 Artifact-free imaging: alternating vs. pass-band SSFP 90

Figure 6.1 Alternating SSFP pulse sequence diagram: 3 T 94
Figure 6.2 Automated stop-band ROI identification method 97
Figure 6.3 Rat images: alternating vs. pass-band SSFP 99
Figure 6.4 Alternating SSFP: SNR and BOLD CNR vs. flip angle 100
Figure 6.5 Rat fMRI maps: alternating vs. balanced SSFP 101
Figure 6.6 Rat fMRI maps: stop-band sensitivity recovery 101
Figure 6.7 BOLD sensitivity: alternating vs. balanced SSFP 102

Figure 7.1 Occipital ROI identification 110
Figure 7.2 Stop-band ROI identification 111
Figure 7.3 Human fMRI maps: individual analysis 113

Figure 7.4 Human fMRI maps: group analysis 114
Figure 7.5 Elimination of stop-bands with alternating SSFP 118

Figure 8.1 Eddy current-induced image artifacts 122
Figure 8.2 Spiral vs. EPI for balanced SSFP 123
Figure 8.3 Alternating SSFP BOLD contrast growth vs. flip angle 124

Abstract

Blood oxygenation level dependent (BOLD) functional magnetic resonance imaging (fMRI) is the dominant tool used for mapping human brain function because it is non-invasive, does not use ionizing radiation, and offers relatively high spatial and temporal resolution compared to other neuroimaging techniques. Unfortunately, conventional fMRI techniques cannot map brain function in the inferior temporal cortex (ITC) and orbitofrontal cortex (OFC). These brain regions experience severe magnetic field distortions due to magnetic susceptibility mismatch with the neighboring air-filled ear-canals (ITC) or sinus cavities (OFC), causing loss of the fMRI signal. Functional imaging capability is important for gaining a better understanding of these brain regions and the diseases that commonly affect them (Alzheimer's disease and epilepsy (ITC), Parkinson's disease and schizophrenia (OFC)).

Balanced steady state free precession (balanced SSFP) is a relatively new fMRI technique that can measure function in all brain regions. Rather than diffuse signal loss, balanced SSFP images exhibit signal loss in spatially periodic, narrow bands. Banding artifacts cannot be eliminated in a single scan, but the phase of the banding artifacts can be controlled by the experimenter, permitting the combination of two antiphase balanced SSFP images to produce a single image free of banding artifacts. Unfortunately, image-corrupting transient signal oscillations limit the rate at which the banding artifact phase can be modified, such that the banding-artifact-free image acquisition rate is prohibitively slow for most clinical and neuroscience applications.

This work describes the development of a modified balanced SSFP fMRI technique, alternating SSFP, which permits rapid, banding-artifact-free balanced SSFP fMRI. Theoretical modeling was used to find a rapid transition between antiphase balanced SSFP images with minimal transient signal oscillations. Monte Carlo simulations were used to optimize alternating SSFP acquisition parameters for BOLD sensitivity, with comparison to established balanced SSFP acquisitions. Rat fMRI was used to confirm these predictions. Finally, the ability of alternating SSFP to provide rapid, banding-artifact-free balanced SSFP fMRI in humans at 4 T was demonstrated.

List of Abbreviations and Symbols Used

Abbreviations

b-SSFP	balanced steady state free precession
BOLD	blood oxygenation level dependent
CBF	cerebral blood flow
CBV	cerebral blood volume
CINE	cinematographic
$CMRO_2$	cerebral metabolic rate of oxygen
CNR	contrast to noise ratio
CPMG	Carr Purcell Meiboom Gill
DFT	discrete Fourier transform
EEG	electroencephalography
EPI	echo planar imaging
FEAT	fMRI expert analysis tool
FID	free induction decay
FLIRT	FMRIB's linear image registration tool
fMRI	functional magnetic resonance imaging
FMRIB	centre for functional magnetic resonance imaging of the brain (Oxford, UK)
FOV	field of view
FSL	FMRIB software library
FWHM	full-width at half-maximum
GLM	general linear model
GRE	gradient echo
Hct	hematocrit
HRF	hemodynamic response function
ITC	inferior temporal cortex
IDFT	inverse discrete Fourier transform

MC	Monte Carlo
MEG	magnetoencephalography
MIP	maximum intensity projection
MRI	magnetic resonance imaging
NMR	nuclear magnetic resonance
OFC	orbitofrontal cortex
pc0	0°-RF-phase-cycled
pc180	180°-RF-phase-cycled
PET	position emission tomography
PSF	point spread function
RF	radio frequency
ROI	region of interest
SE	spin echo
SFG	susceptibility-induced magnetic field gradient
SNR	signal to noise ratio
SOS	sum-of-squares
SPECT	single photon emission computed tomography
SPGR	spoiled gradient echo
SPM	statistical parametric mapping
SSFP	steady state free precession
STFR	small-tip fast recovery

Symbols

α	flip angle
θ	off-resonance precession angle
E	energy
f	blood volume fraction
$\vec{G}$	magnetic field gradient
i	$\sqrt{-1}$
$\mathbf{k}$	reciprocal lattice vector
$\vec{B}_0$	static (polarizing) magnetic field
$\vec{B}_1$	oscillating (perturbing) magnetic field
$\vec{L}$	angular momentum
$\vec{M}_0$	equilibrium magnetization
$\vec{S}$	spin angular momentum
$\vec{\mu}$	magnetic moment
$\vec{\Omega}$	angular velocity
ω_0	Larmor frequency
ω_1	RF precession frequency (in the rotating frame)
$\Delta\omega$	off-resonance frequency
ϕ	phase angle
P	probability
ρ_0	spin density
ρ	effective spin density
$\vec{r}$	position
R	radius
R_2	irreversible spin-spin relaxation rate ($1/T_2$)
S	signal
$\vec{\tau}$	torque
τ	time-duration
t	time
T	temperature

T_1	spin-lattice relaxation time
T_2	irreversible spin-spin relaxation time
T_2'	reversible spin-spin relaxation time
T_2^*	effective spin-spin relaxation time
T_E	echo time
T_R	repetition time
T_{vol}	volume acquisition time
V	volume
χ	magnetic susceptibility
Y	blood oxygen saturation fraction
Z	partition function

Acknowledgements

First and foremost I would like to thank my supervisor Chris Bowen for introducing me to the fascinating topic of SSFP, and for patiently encouraging me throughout my studies. Next I would like to thank Erin Mazerolle for her unwavering support; the list of things that Erin *didn't* help me with is pretty short.

I am grateful to have received expert guidance over the years from my supervisory committee: Steven Beyea, Kevin Hewitt, and Gerhard Stroink. Drew DeBay, David McAllindon, and Tynan Stevens provided much-appreciated assistance with my experiments, and Kirk Feindel gave helpful comments on early drafts of my thesis.

My research would not have been possible without the generous support of NSERC, The Killam Trusts, The Walter C. Sumner Memorial Fellowship, and the NSHRF. Finally I would like to thank Shenna LaPointe for her love and encouragement.

Chapter 1

Introduction

1.1 Functional Magnetic Resonance Imaging

Blood oxygenation level dependent (BOLD) functional magnetic resonance imaging (fMRI) has become the dominant tool used for mapping human brain function because it offers a favorable combination of spatial resolution (millimeter), temporal resolution (second), and safety to the subject under investigation, relative to other neuroimaging techniques. Electrophysiological methods such as electroencephalography (EEG) and magnetoencephalography (MEG) offer high (millisecond) temporal resolution, but poor spatial resolution (at best, centimeter; at worst, undefined due to an ill-posed inverse problem) and an inability to measure neural activity deep within the brain. Nuclear imaging techniques such as position emission tomography (PET) and single photon emission computed tomography (SPECT) can measure hemodynamic changes associated with neural activity, similar to fMRI, and provide complementary information, such as mapping glucose metabolism. However, nuclear imaging techniques offer reduced spatial (centimeter) and temporal (ten second) resolution, and expose the subject to harmful ionizing radiation.

Functional MRI has led to major advances in cognitive neuroscience, including the discovery that brain regions function together in networks, and the demonstration of the brain's ability to rewire following injury, referred to as neural plasticity. While to date the clinical impact of fMRI has been modest, the clinical applications of fMRI are expected to increase [1]. Functional MRI is already establishing itself as an important tool for pre-surgical planning of brain tumor resection. Tumor resection cannot be planned based on anatomical information alone, as anatomically similar brains may differ considerably in functional organization. Functional MRI can aid surgeons by identifying routes thorough the brain by which a tumor can be removed while leaving key brain functions intact.

1.2 Limitations of Conventional fMRI

BOLD fMRI indirectly measures neural activity by measuring the local increase in blood oxygenation that accompanies it. Deoxygenated blood is paramagnetic because it contains iron atoms with unpaired electrons. Oxygenated blood is diamagnetic because it contains iron-oxygen complexes with no unpaired electrons. Deoxygenated blood perturbs the local magnetic field, causing signal loss in fMRI scans. Neural activity results in an increase in blood oxygenation, and therefore a increase in signal intensity in fMRI scans.

The majority of fMRI studies are conducted using gradient echo (GRE) pulse sequences. GRE pulse sequences are very sensitive to magnetic field inhomogeneities, such as those involved in the BOLD effect. Unfortunately, conventional GRE fMRI cannot map brain function in the inferior temporal cortex (ITC) and orbitofrontal cortex (OFC). These brain regions experience magnetic field inhomogeneities much larger than those involved in the BOLD effect, due to magnetic susceptibility mismatch with the neighboring air-filled ear-canals (ITC) or sinus cavities (OFC) (Fig. 1.1). The use of a GRE sequence, tuned to produce maximal variations in signal intensity from small variations in magnetic field homogeneity (such as those associated with the BOLD effect), results in the total loss of the MRI signal in regions of severe magnetic field inhomogeneity such as the ITC and OFC (Fig. 1.2). Functional imaging capability in the ITC and OFC is important to gain a better understanding of these brain regions and the diseases that commonly affect them (Alzheimer's disease and epilepsy (ITC), Parkinson's disease and schizophrenia (OFC)). New fMRI techniques capable of whole-brain coverage are needed.

1.3 Approaches to Overcome the Limitations of Conventional fMRI

1.3.1 Mitigating Signal Dropout in GRE fMRI

Several approaches have been taken to reduce signal dropout in GRE fMRI.

One simple approach is to reduce the thickness of the imaging slices, which decreases the phase spread across the imaging voxels, reducing signal cancellation [5]. However, acquisition time is inversely proportional to slice thickness (for fixed volume coverage); the small slice thickness needed to eliminate signal dropout in regions of

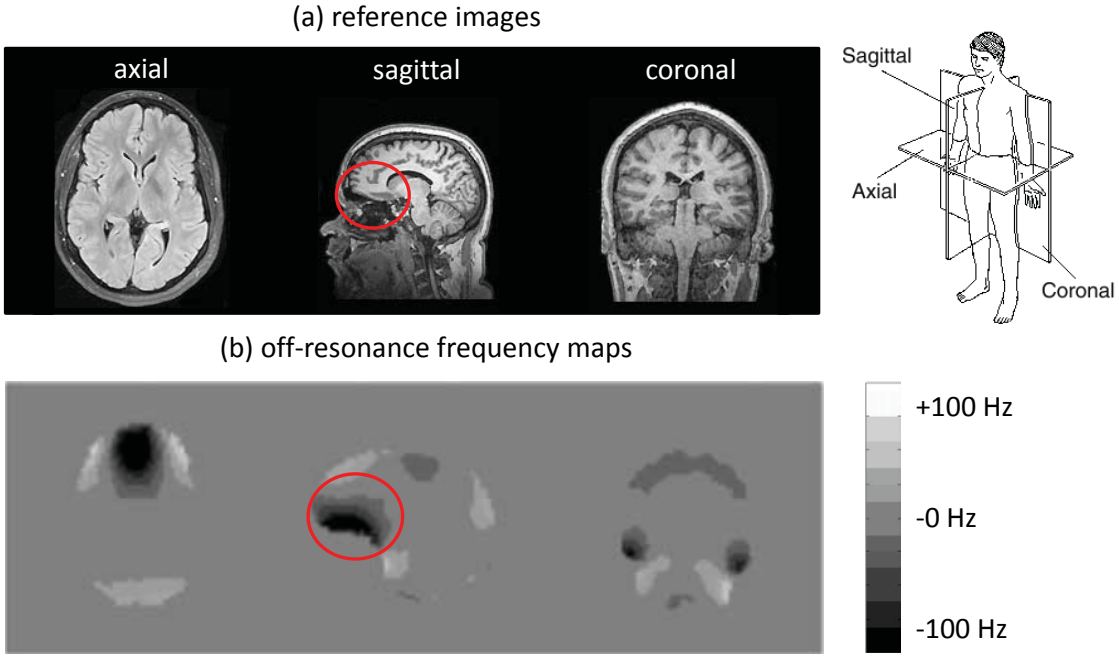

Figure 1.1: (a) Axial, sagittal, and coronal views from an anatomic MR image of a human head from [2]. (b) Corresponding off-resonance frequency maps from [3]. Note that off-resonance frequency is proportional to magnetic field inhomogeneity. Large magnetic field inhomogeneities occur in brain regions near air-tissue interfaces, such as in the OFC bordering the nasal and sinus cavities (circled in red). Note that the frequency variations associated with BOLD activity (a few Hz at 4 T) are much smaller than those associated with air-tissue interfaces.

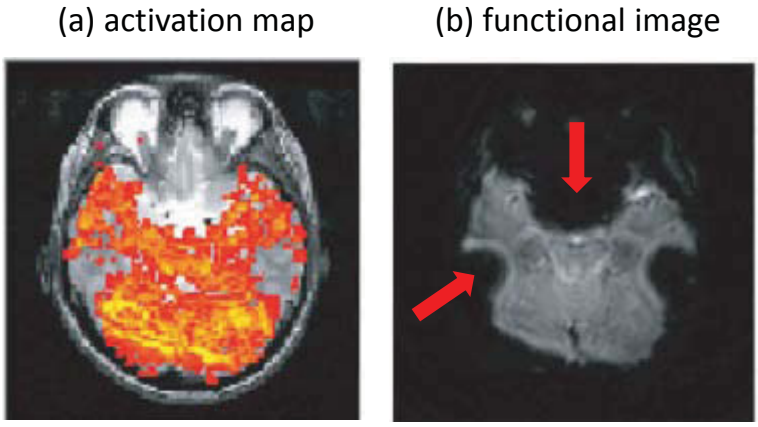

Figure 1.2: (a) BOLD activation map (red-yellow) from a breathold task (expected to elicit whole-brain changes in blood oxygenation) obtained with a GRE sequence, overlaid on an axial anatomic (high spatial resolution, BOLD insensitive) MR image (greyscale). BOLD activation is not observed in the OFC (top, near the eyes), nor in the ITC (middle left and right, near the ears). (b) Example image from the timeseries of low-spatial-resolution GRE images used to generate the BOLD activation map in (a). Total loss of the MRI signal is observed in the OFC (upper red arrow) and ITC (lower red arrow), corresponding to the voids in BOLD sensitivity observed in (a). Images from [4].

severe magnetic field inhomogeneity exceeds practical limits on acquisition time [6]. Another simple approach is to reduce the time between perturbing the magnetization and encoding the MRI signal, referred to as the echo time, T_E. This allows less time for signal dephasing, again reducing the phase spread across the imaging voxels, reducing signal cancellation. However, GRE sequences derive BOLD sensitivity from signal dephasing; at the short T_E values required to eliminate signal dropout, insufficient BOLD sensitivity remains with GRE sequences [7].

Z-shim approaches involve the application of additional z-directed magnetic field gradients to counter those caused by magnetic susceptibility mismatch [6,8,9]. Slices are acquired at multiple compensation-gradient values, which produce a uniform magnetic field at different regions of the slice, and combined to produce a single, dropout-free slice. Z-shim approaches have reduced efficiency, however, as slices in regions of severe magnetic field inhomogeneity must be acquired four or more times per image volume [8]. Alternatively, a 3D technique with twice the image volume time of an uncorrected acquisition can be used [6]. Even so, z-shim methods cannot correct for non-linear phase variations, nor for non-z-directed magnetic field gradients.

Tailored radio frequency (RF) pulses [10–12] involve acquiring an off-resonance frequency map at the beginning of the fMRI experiment and using this map to compute the spatially-varying phase expected at the echo time. An RF pulse is then designed to impart the opposite of this spatially-varying phase to the perturbed magnetization. As a result, signal dephasing from static magnetic field inhomogeneities is refocused at the echo time, while dephasing from time-varying magnetic field inhomogeneities, such as those responsible for the BOLD effect, remain. 1D tailored RF pulses (imparting a phase variation in the z-direction), however, require multiple acquisitions per slice, similar to z-shim techniques. 3D tailored RF pulses can eliminate signal loss with a single image volume acquisition [12] but can be prohibitively long (60 ms, such that the duration of the RF pulse precludes acquisition of the fMRI signal at the optimal (for BOLD sensitivity) echo time (about 30 ms at 4 T), reducing BOLD sensitivity). Nonetheless improvements in pulse design [13] and the incorporation of parallel transmit technology [14] may make tailored RF pulses the method of choice in the future. At present, however, signal dropout continues to be a limitation for GRE fMRI.

1.3.2 Alternatives to GRE for fMRI

Other methods for whole-brain fMRI involve abandoning GRE altogether.

Perfusion fMRI techniques measure the changes in blood flow (rather than oxygenation) that accompany neural activity and, unlike BOLD fMRI techniques, do not rely on signal dephasing to attain functional contrast. Signal dropout can therefore be avoided by using short echo times in perfusion fMRI. However, perfusion fMRI techniques are limited by low functional sensitivity [15], and reduced spatial coverage (whole brain coverage is difficult or impossible) compared to GRE BOLD.

Spin-echo (SE) pulse sequences involve the application of an additional RF pulse to refocus the signal dephasing caused by large-scale magnetic field inhomogeneities, producing images without signal dropout. However, the additional RF pulse also refocuses some of the signal dephasing caused by the BOLD effect itself, reducing BOLD sensitivity compared to GRE sequences. The BOLD effect is small, and this loss in sensitivity can be prohibitive [16].

Recently (2005 [17]), fMRI has been demonstrated using the pass-band balanced

steady state free precession (pass-band SSFP) pulse sequence. Unlike GRE and SE sequences, pass-band SSFP maintains BOLD sensitivity at arbitrarily short T_E [7, 17], permitting a higher data acquisition duty cycle[1] and reduced image distortion compared to GRE and SE methods [18]. Pass-band SSFP may offer enhanced BOLD sensitivity over SE methods, particularly given that BOLD sensitivity is proportional to SNR-efficiency, and pass-band SSFP is the most SNR-efficient of all known pulse sequences [18].

Rather than diffuse signal loss, pass-band SSFP images exhibit signal loss in spatially periodic, narrow bands (Fig. 1.3a). Banding artifacts cannot be eliminated in a single scan, but they can be shifted in space by modifying a user-controlled image acquisition parameter called the RF phase cycling increment (Fig. 1.3b). Thus two pass-band SSFP images acquired with complementary RF phase cycling increments can be combined to produce a single, banding artifact-free image (Fig. 1.3c). This technique was coined the two-acquisition method by Lee [4], who used it to demonstrate the efficacy of pass-band SSFP for whole-brain fMRI with a breath hold task in 2008 (Fig. 1.4).

Unfortunately, two-acquisition pass-band SSFP is prohibitively slow for most clinical and neuroscience applications. To dynamically track blood oxygenation changes in the brain, functional images must be acquired roughly every 3 s; two-acquisition pass-band SSFP is limited to producing one banding-artifact-free image every 10 s. The two images required for banding-artifact removal with pass-band SSFP are derived from different steady states. Once in a given steady state, functional images can be acquired in rapid succession. However, transitioning between steady states takes about 3 s. This adds 6 s of dead-time to the acquisition of each image pair needed to produce one banding-artifact-free image (Fig. 1.5).

The study demonstrating whole-brain pass-band SSFP fMRI using the two-acquisition method [4] avoided dead-time by acquiring an entire timecourse of 180°-RF-phase-cycled images, then repeating the four minute breathold functional paradigm to acquire an entire timecourse of 0°-RF-phase-cycled images. A single, artifact-free image

[1] i.e., in GRE fMRI one must wait about 30 ms after every RF pulse before data acquisition, to allow BOLD contrast to develop. For a 32-slice, single-shot (i.e., all of the data required to reconstruct one image slice is acquired following a single RF pulse), whole-brain acquisition, this increases the time required to encode each image volume by about one second. This is not the case in pass-band SSFP; data acquisition can commence immediately after the RF pulse.

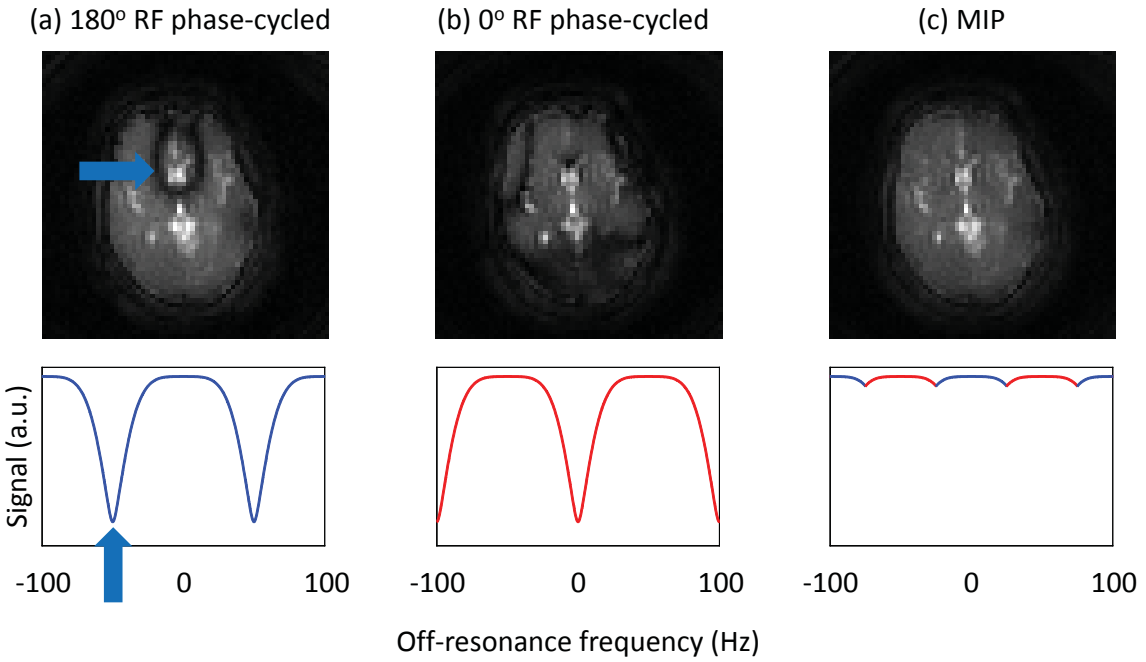

Figure 1.3: Pass-band SSFP images (top row) with corresponding signal vs. off-resonance frequency profiles shown directly below (bottom row). Pass-band SSFP images exhibit banding artifacts separated by $1/T_R$ in off-resonance frequency (100 Hz in this example). Banding artifacts cannot be eliminated, but they can be translated in off-resonance frequency by incrementing the phase of the RF pulses in a process known as phase cycling. Thus two pass-band SSFP images acquired with complementary RF phase cycling increments (a) and (b) can be combined, via maximum intensity projection (MIP), to produce a single, banding artifact-free image (c).

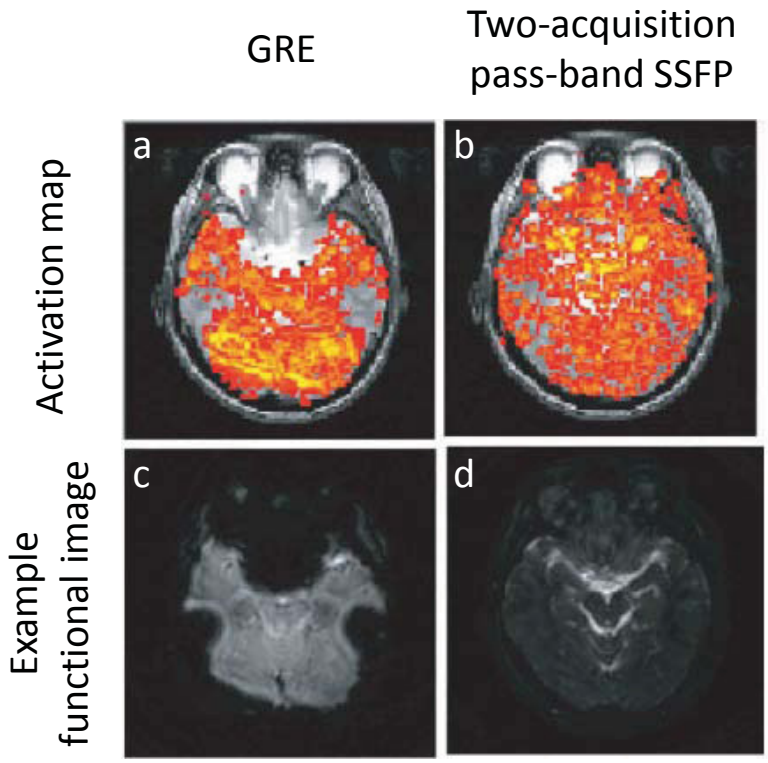

Figure 1.4: BOLD activation maps (red-yellow) from a breathold task for GRE (a) and two-acquisition pass-band SSFP (b) overlaid on an axial anatomic MR image (greyscale). BOLD activation is observed in the OFC and ITC with two-acquisition pass-band SSFP, but not with GRE. Example image from the timeseries of low-spatial-resolution images used to generate the correpsonding BOLD activation maps for GRE (c) and two-acquisition pass-band SSFP (d). Signal loss is observed in the OFC and ITC for GRE, but not for two-acquisition pass-band SSFP. Images from [4].

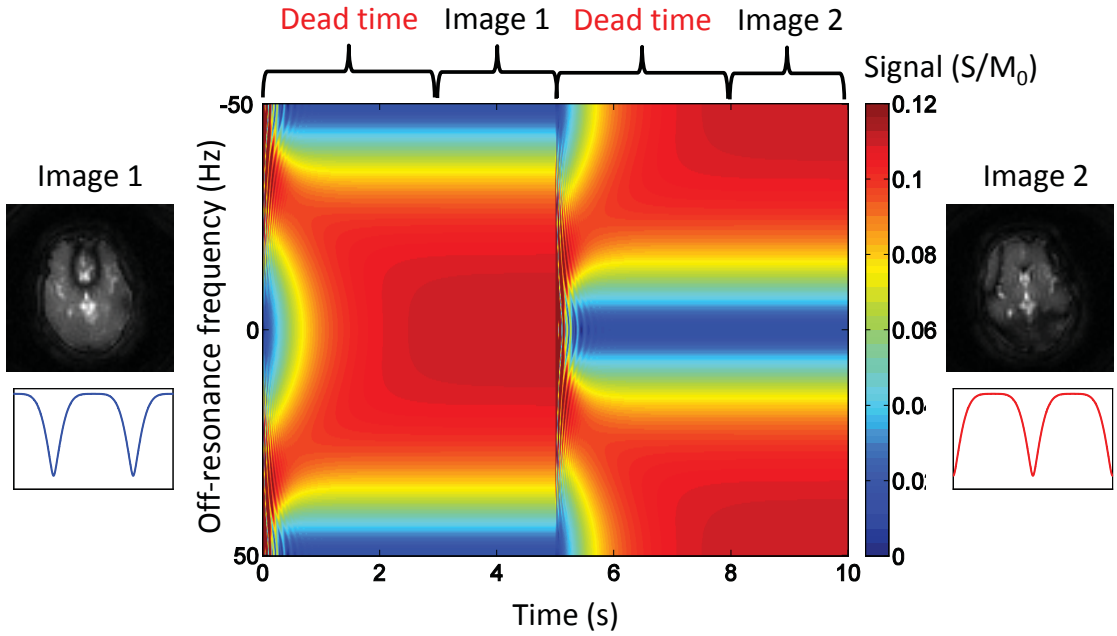

Figure 1.5: The MRI signal (amplitude indicated by colorbar) vs. time (x-axis) and off-resonance frequency (y-axis) when alternating between 180°- and 0°-RF-phase-cycled steady states (RF increment = 180° for $0 < t < 5$ s and 0° for $5 < t < 10$ s). Also shown are the complementary (180°-RF-phase-cycled (image 1) and 0°-RF-phase-cycled (image 2)) images required for banding artifact removal, as well as their corresponding signal vs. off-resonance frequency profiles (directly below). Following the acquisition of a given image, it takes about 3 s to establish the opposing steady state before the complementary image can be acquired. While pass-band SSFP images can be acquired in rapid succession from a given steady state, alternating between two steady states introduces about 6 s of dead-time per image pair. Data from numerical simulations of the Bloch equations.

timecourse was then generated by pairing images from the two timecourses collected four minutes apart. This method of repeating the functional paradigm suffices for proof-of-concept studies, however, it is unsuitable for most clinical and neuroscientific applications. It assumes that the response of the brain to the second run of the functional paradigm is identical to the first; this assumption is not valid due to factors such as habituation, practice, and learning. Thus while pass-band SSFP fMRI offers advantages over SE and GRE methods, at present it is too slow for whole-brain applications.

1.4 Project Overview and Hypothesis

The goal of this work was to develop a modified two-acquisition pass-band SSFP fMRI technique, alternating SSFP, capable of acquiring both images needed for banding artifact removal in 3 s (i.e., fast enough to track blood oxygenation changes in the brain). The primary challenges associated with alternating SSFP are reducing signal oscillations and maintaining BOLD sensitivity, discussed next.

Signal Oscillations

Alternating SSFP images must be acquired during the transient phase of balanced SSFP; time constraints prevent the establishment of the steady state. The transient phase of balanced SSFP is characterized by oscillations in the MRI signal, which cause image artifacts. These signal oscillations must be suppressed for alternating SSFP to be successful. RF catalyzation strategies [19–21] have been successfully used to reduce signal oscillations during the transition from equilibrium to steady state in pass-band SSFP. We hypothesize that RF catalyzation strategies can also be used to reduce signal oscillations during the transition between (quasi) steady states in alternating SSFP.

BOLD Sensitivity

Once a smooth signal transition between steady states has been found, it must be determined if alternating SSFP maintains BOLD sensitivity. Monte Carlo simulations have been successfully used to characterize the BOLD sensitivity of pass-band

SSFP [22, 23]; we will use similar Monte Carlo simulations to characterize the BOLD sensitivity of alternating SSFP.

The alternating SSFP acquisition parameter space is too broad to probe experimentally. We hypothesize that Monte Carlo simulations can be used to search this acquisition parameter space, with comparison to established balanced SSFP acquisitions, to find a set of acquisition parameters that maximize BOLD sensitivity.

1.4.1 Thesis Outline

This thesis begins with a chapter introducing MRI (chapter 2), including an introduction to balanced SSFP (section 2.12) and RF catalyzation (section 2.12.3). Chapter 3 provides an introduction to functional MRI, including a review of fMRI using balanced SSFP (section 3.7).

The next four chapters (chapters 4 to 7) describe original research involving the development and implementation of alternating SSFP. Chapter 4 describes Bloch simulations used to find a smooth signal transition between steady states, and Monte Carlo simulations used to characterize, and to identify acquisition parameters to maximize, alternating SSFP BOLD sensitivity. Chapter 5 describes the implementation of alternating SSFP on a 4 T human MRI system, and experiments used to confirm the theoretically-predicted alternating SSFP signal behaviour, and to compare image quality between alternating and conventional pass-band SSFP acquisitions. Chapter 6 describes the implementation of alternating SSFP on a 3 T small animal MRI system, and experiments used to demonstrate the efficacy of alternating SSFP for whole-brain fMRI with 3 s temporal resolution in rats, and to confirm theoretical predictions for the optimum acquisition parameters. Chapter 7 describes experiments used to demonstrate the ability of alternating SSFP to provide banding-artifact-free fMRI in humans at 4 T with 3 s temporal resolution.

The final chapter of this thesis (chapter 8) outlines some potential directions for future work.

1.5 Contributions to Research

The Alternating SSFP pulse sequence was developed by Steve Patterson and Chris Bowen. An existing RF catalyzation strategy [21], developed for cardiac balanced

SSFP, was adopted to reduce signal oscillations in alternating SSFP. The flip-down RF pulse, added to the alternating SSFP pulse sequence to further-reduce signal oscillations, was developed by Steve Patterson.

The Monte Carlo model was coded in MATLAB by Steve Patterson, augmenting an existing algorithm [24] to include intravascular T_2 changes as well as pass-band SSFP and alternating SSFP pulse sequences.

Implementation and testing of alternating SSFP on the 3 T small animal MRI system was performed by Steve Patterson. An existing GRE spiral pulse sequence, written by Martyn Klassen, was repurposed to create alternating SSFP. Modifications to the data acquisition (conversion of GRE to alternating SSFP) and image reconstruction code (addition of post-processing image combination to eliminate banding artifacts) were performed by Steve Patterson. The rat hypercapnia experimental setup was performed by Drew DeBay and Erin Mazerolle. Experimental design was performed by Erin Mazerolle and Steve Patterson. Animal handling was performed by Erin Mazerolle and Steve Patterson, with assistance from Drew DeBay and Kirk Feindel. Rat fMRI data acquisition was performed by Steve Patterson, with assistance from Erin Mazerolle. Rat fMRI data analysis was performed by Steve Patterson using pre-existing software packages (SPM and FSL), under the guidance of Erin Mazerolle.

Implementation and testing of alternating SSFP on the 4 T human MRI system was performed by Steve Patterson. Experimental design was performed by Steve Patterson and Chris Bowen. The visual stimulation experimental setup was performed by Kim Brewer. Modifications were made by Steve Patterson with help from Tynan Stevens. Human fMRI data acquisition was performed by Steve Patterson, with assistance from David McAllindon. Human fMRI data analysis was performed by Steve Patterson (using FSL), aided by helpful discussions with Erin Mazerolle.

A manuscript based on the Monte Carlo simulation results (chapter 4), including experimental confirmation of the theoretically-predicted alternating SSFP signal behaviour (chapter 5), has been submitted to NMR in Biomedicine. Reviews were issued on October 23, 2013, requesting major revisions citing the need to experimentally-confirm BOLD sensitivity with alternating SSFP. A revision including experimental human fMRI data (chapter 7) is in preparation.

Chapter 2

Background: Magnetic Resonance Imaging (MRI)

2.1 Overview

In MRI an object is placed in a strong magnetic field, which results in the alignment of a fraction of the object's nuclear magnetic moments (section 2.2) along the field (section 2.3), forming the magnetization vector. The magnetization vector is then tilted away from the external field by applying a second oscillating (at radio-frequency) magnetic field, perpendicular to the static field (section 2.5). The perturbed magnetization precesses about the static field (section 2.4) as it returns to equilibrium alignment with the static field via relaxation processes (section 2.7). The precessing magnetization is detected as an induced voltage in a coil oriented perpendicular to the static field (section 2.6). Spatial encoding (imaging) is achieved by augmenting the static field with spatially varying magnetic fields (gradients) to create a position-dependent precession frequency in the object (section 2.11). These topics are treated in more detail below. This chapter follows the MRI textbooks of Haacke [25] and Callaghan [26].

2.2 Spin and the Magnetic Moment of the Proton

A charged object possessing angular momentum $\vec{L}$ has a magnetic moment $\vec{\mu}$ given by:

$$\vec{\mu} = \gamma \vec{L}, \tag{2.1}$$

where γ is the gyromagnetic ratio. For a classical rotating body having identically-distributed charge and mass, γ is one-half of the charge-to-mass ratio:

$$\gamma = \frac{q}{2m}. \tag{2.2}$$

Many elementary and composite particles, including the proton[1], possess an intrinsic angular momentum called spin. This gives rise to an intrinsic magnetic moment:

$$\vec{\mu} = \gamma \vec{S}, \tag{2.3}$$

where $\vec{S}$ represents the spin angular momentum vector. The gyromagnetic ratio for the proton is:

$$\gamma = 2.675 \times 10^8 \text{ rad} \cdot \text{s}^{-1} \cdot \text{T}^{-1}, \tag{2.4}$$

which is close to three times the proton's charge to mass ratio. Frequently the reduced γ is used, 'gamma-bar', which, for the proton, is:

$$\gamma\!\!\!^{-} = \frac{\gamma}{2\pi} = 42.58 \text{ MHz/T}. \tag{2.5}$$

Spin is described by the spin quantum number, s, which can take on non-negative integer or half-integer values ($s = 0, 1/2, 1, 3/2$, etc). The proton has spin quantum number $s = 1/2$. Total spin angular momentum, as well the component measured along any direction, is quantized. Total spin angular momentum is given by:

$$\left|\vec{S}\right| = \hbar\sqrt{s(s+1)}. \tag{2.6}$$

The component measured along the (arbitrarily chosen) z-direction is given by:

$$S_z = m_s \hbar, \tag{2.7}$$

where m_s can take on values of $-s, -s+1, ..., s-1, s$. For a spin 1/2 particle such as the proton, only two values of S_z are possible, $\pm\hbar/2$, and thus two values of z-directed magnetic moment, $\mu_z = \pm\gamma\hbar/2$.

2.3 Equilibrium Magnetization

Consider N protons in a volume V in the presence of a uniform external z-directed[2] magnetic field $\vec{B_0} = B_0\hat{z}$. The protons are divided into two energy levels based on the z-component of their spin angular momentum:

$$E_\pm = -\vec{\mu} \cdot \vec{B_0} = -\mu_z B_0 = \mp\gamma\hbar B_0/2. \tag{2.8}$$

[1]the focus of this introductory chapter is the hydrogen nucleus, i.e., the proton, which is the dominant nucleus in MRI due to its relative abundance in the human body (in the form of H_2O).

[2]unless specified, we will always take the external (static) magnetic field to point in the z-direction with amplitude B_0

Spins aligned with the external magnetic field (denoted by the + symbol) are in a lower energy state (E_+) than those opposed to it (E_-). The probability of a given spin being aligned or anti-aligned is given by the Boltzmann distribution:

$$P(E) = \exp(-E/k_B T)/Z, \tag{2.9}$$

where P is the probability of the state having energy E, T is temperature in Kelvin, $k_B = 1.38 \times 10^{-23}$ J/K is Boltzmann's constant, and Z is the partition function which normalizes the probability distribution:

$$Z = \sum_E \exp(-E/k_B T). \tag{2.10}$$

At low temperature, the lower-energy (aligned) state is more probable, while at high temperature both states are equally likely.

The difference in probability between aligned and anti-aligned states is given by:

$$P(E_+) - P(E_-) = \frac{\exp(a) - \exp(-a)}{\exp(a) + \exp(-a)}, \tag{2.11}$$

where $a = \hbar\gamma B_0/(2k_B T)$. For protons at room temperature in a 4 T magnetic field, $a \approx 10^{-5}$, and eq. 2.11 can be approximated:

$$P(E_+) - P(E_-) \approx a, \tag{2.12}$$

i.e., for every million protons, 10 more are aligned with the field than anti-aligned. This spin-excess gives rise to a net magnetization, or magnetic moment per unit volume:

$$\vec{M}_0 = \frac{Na\mu_z}{V}\hat{z} = \frac{\rho_0 \hbar^2 \gamma^2 B_0}{4k_B T}\hat{z}, \tag{2.13}$$

where Na represents the spin-excess (the net spin alignment), μ_z is the magnitude of the z-component of the magnetic moment of a single proton ($\gamma\hbar/2$), and $\rho_0 = N/V$ is the proton density. Note that, while the spin-excess is extremely small, the density of hydrogen nuclei in water is extremely large (on the order of 10^{29} hydrogen nuclei/m^3). This makes MRI possible, and is the reason that the hydrogen nucleus is the dominant nucleus in MRI.

2.4 Semi-Classical Equations of Motion

A magnetic moment $\vec{\mu}$ in an external magnetic field $\vec{B}$ experiences a torque:

$$\vec{\tau} = \vec{\mu} \times \vec{B}, \tag{2.14}$$

which causes a change in angular momentum according to Newton's second law:

$$\vec{\tau} = \frac{d\vec{L}}{dt} = \frac{1}{\gamma}\frac{d\vec{\mu}}{dt}, \tag{2.15}$$

where the relationship between magnetic moment and angular momentum (eq. (2.1)) has been used. Combining eqs. (2.14) and (2.15), we obtain the equation of motion for a magnetic moment in a magnetic field:

$$\frac{d\vec{\mu}}{dt} = \gamma\vec{\mu} \times \vec{B}. \tag{2.16}$$

This equation describes a clockwise precession about the magnetic field (Fig. 2.1):

$$\begin{aligned} \mu_z(t) &= \mu_z(0) \\ \mu_{xy}(t) &= \mu_{xy}(0)\exp(-i\omega_0 t), \end{aligned} \tag{2.17}$$

at the Larmor (angular) frequency,

$$\omega_0 = \gamma B_0. \tag{2.18}$$

Here γ is the gyromagnetic ratio, the magnetic field $\vec{B}$ has been taken to point in the z-direction with amplitude B_0, and the transverse components of magnetic moment have been expressed in complex form $\mu_{xy} = \mu_x + i\mu_y$. This equation of motion can be extended to an ensemble of non-interacting spins[3], i.e., the magnetization:

$$\frac{d\vec{M}}{dt} = \gamma\vec{M} \times \vec{B}, \tag{2.19}$$

with solution:

$$\begin{aligned} M_z(t) &= M_z(0) \\ M_{xy}(t) &= M_{xy}(0)\exp(-i\omega_0 t). \end{aligned} \tag{2.20}$$

[3]modifications to this equation of motion due to interactions between the spins and their environment are addressed in section 2.7

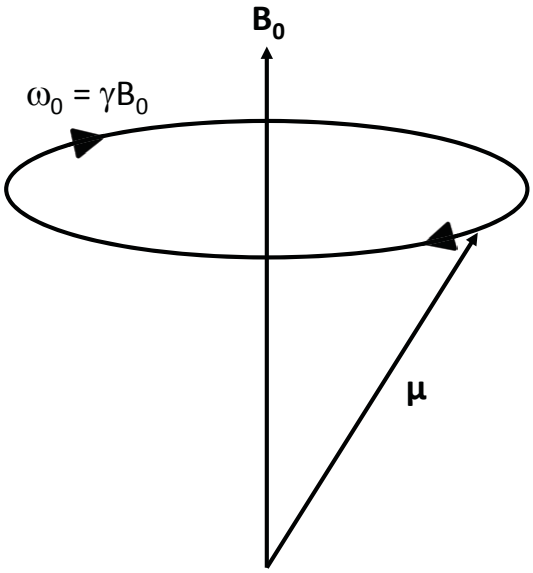

Figure 2.1: Precession of a magnetic moment $\vec{\mu}$ about an external magnetic field $\vec{B}_0$ at the Larmor angular frequency ω_0.

2.5 Excitation

The magnetization vector (eq. 2.13) that develops when a group of spins are placed in an external magnetic field points along the direction of the field, and thus does not change in time (eq. 2.19 for $\vec{M} \times \vec{B} = 0$). To produce a time-varying magnetic field that can be detected using a pickup coil by Faraday induction, the magnetization vector must first be tilted away from the static field. This is achieved by the application of an additional, oscillating magnetic field

$$\vec{B}_1(t) = B_1 \cos(\omega_0 t)\hat{x} - B_1 \sin(\omega_0 t)\hat{y}, \tag{2.21}$$

applied perpendicular to the static field $B_0\hat{z}$, at a frequency $\omega_0 = \gamma B_0$, such that the total field is:

$$\vec{B}(t) = B_1 \cos(\omega_0 t)\hat{x} - B_1 \sin(\omega_0 t)\hat{y} + B_0\hat{z}. \tag{2.22}$$

The oscillating field is in the radio-frequency (RF) range for typical static magnetic field strengths of 1.5 - 9.4 T, and is only applied for a short time, hence its name "RF pulse". The evolution of the magnetization during the application of an RF pulse is most easily treated in a rotating frame of reference.

2.5.1 The Rotating Reference Frame

Consider a rotating frame of reference, whose rotation with respect to a static frame is described by the angular velocity vector $\vec{\Omega}$ in the static frame. The tail of $\vec{\Omega}$ is the origin in the static frame - i.e., the origins of both reference frames are co-localized at all points in time. The rate of change of a vector $\vec{f}(t)$ in the rotating frame is related to that in the static frame by:

$$\left(\frac{d\vec{f}}{dt}\right)_r = \frac{d\vec{f}}{dt} - \vec{\Omega} \times \vec{f}, \tag{2.23}$$

where the subscript r refers to the rotating frame. This is simply the rate of change of $\vec{f}$ in the static frame, with a component subtracted to account for the rotation of the reference frame.

By substituting $\vec{M}$ for $\vec{f}$ in eq. (2.23) and combining with eq. (2.19), we obtain an expression for the evolution of the magnetization $\vec{M}$ in a rotating reference frame:

$$\left(\frac{d\vec{M}}{dt}\right)_r = \gamma\vec{M} \times \left(\vec{B} + \vec{\Omega}/\gamma\right). \tag{2.24}$$

The magnetization precesses about the "effective" field $\vec{B} + \vec{\Omega}/\gamma$ in the rotating reference frame.

Consider the evolution of the magnetization vector in the presence of the applied field given in eq. (2.22), in a reference frame rotating with angular velocity vector $\vec{\Omega} = -\omega_0\hat{z} = -\gamma B_0\hat{z}$. The rotating and static reference frames share a common z-axis, while the x- and y-axis are related according to:

$$\begin{aligned} \hat{x_r} &= \cos(\omega_0 t)\hat{x} - \sin(\omega_0 t)\hat{y} \\ \hat{y_r} &= \sin(\omega_0 t)\hat{x} + \cos(\omega_0 t)\hat{y}, \end{aligned} \tag{2.25}$$

where subscript r signifies the rotating frame. The $\vec{B_1}$ field (eq. (2.21)) points along the $\hat{x_r}$ axis, and the evolution of the magnetization in the rotating frame is written:

$$\left(\frac{d\vec{M}}{dt}\right)_r = \gamma\vec{M} \times B_1\hat{x_r}. \tag{2.26}$$

This represents a precession about the x-axis in the rotating reference frame at an angular frequency $\omega_1 = \gamma B_1$. The angle α through which the magnetization vector is

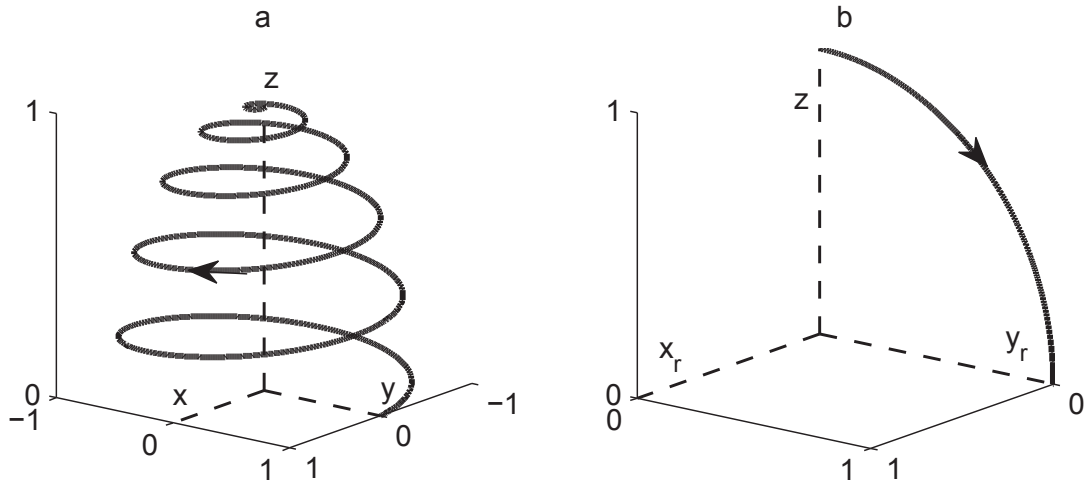

Figure 2.2: Magnetization trajectory during the application of a 90° RF pulse in the laboratory (a) and rotating (b) reference frames. The depiction of the magnetization trajectory in the laboratory frame is not to scale: in reality the magnetization completes thousands of rotations about the z-axis during its decent to the transverse plane.

rotated depends on the duration τ and strength B_1 of the RF pulse:

$$\alpha = \gamma B_1 \tau = \omega_1 \tau. \tag{2.27}$$

Figure 2.2 depicts the trajectory of the magnetization in the laboratory and rotating reference frames during the application of a 90° RF pulse. Once titled away from the static field, the precessing magnetization can be detected via Faraday induction by a coil oriented perpendicular to the static field.

2.6 Signal Detection

The voltage induced in a coil, which is the measured signal S in MRI[4], depends on the rate of change of magnetic flux through the coil:

$$S = -\frac{d}{dt} \int_{\text{coil surface}} \vec{B} \cdot d\vec{A}, \tag{2.28}$$

where $\vec{B}$ is the magnetic field at the coil surface and $d\vec{A}$ is a coil surface area element with a direction normal to the coil surface. The dependence of S on the magnetization

[4]up to a constant that depends on amplifier gain

vector $\vec{M}$ is obtained using the principle of reciprocity: the flux through the coil from the magnetization is equivalent to the flux through the magnetization, per unit current, from the coil ($\vec{B}_1/i$) [26]. The signal is then expressed[5]:

$$S = -\frac{d}{dt}\int (\vec{B}_1(\vec{r})/i) \cdot \vec{M}(\vec{r}) dV, \tag{2.29}$$

where the integral is over the magnetization-containing volume V with volume-element dV. Taking $\vec{B}_1(\vec{r})/i = (B_1/i)\hat{x}$ and $\vec{M}(\vec{r}) = M_0(\cos(\omega_0 t)\hat{x} - \sin(\omega_0 t)\hat{y})$[6] (neglecting, for the moment, spatial variations in the coil sensitivity, magnetization, and external field), the signal can be expressed:

$$S(t) = \omega_0 M_0 (B_1/i) V \sin(\omega_0 t) \tag{2.30}$$

Recalling eqs. (2.13) and (2.18):

$$\begin{aligned} |S| &\propto \omega_0 M_0 (B_1/i) V \\ &\propto \frac{\rho_0 \gamma^3 B_0^2 (B_1/i) V}{T}. \end{aligned} \tag{2.31}$$

Equation 2.31 explains two phenomena in MRI, which is often limited by low SNR. The dependence of the detected signal amplitude $|S|$ on the spin density ρ_0 accounts for the popularity of water proton MRI; the spin-density of ^{1}H in the human body is about three orders of magnitude greater than that of other NMR-visible nuclei. The dependence on B_0^2 accounts for the progression to higher and higher magnetic field strengths.

Signal phase information is obtained by heterodyning (multiplication followed by low-pass filtering) with $\sin(\Omega t)$ and $-\cos(\Omega t)$ [25], to give real and imaginary channels, respectively. These are then combined to give the complex demodulated signal, $\tilde{S}$:

$$\tilde{S}(t) = \omega_0 M_0 (B_1/i) V \exp(i(\Omega - \omega_0)t). \tag{2.32}$$

Including spatial variations in the coil sensitivity, magnetization, and external field, the general complex demodulated signal is:

$$\tilde{S}(t) = \int \rho(\vec{r}) \exp(i(\Omega - \omega(\vec{r}))t) dV, \tag{2.33}$$

[5] $\vec{B}_1(\vec{r})/i$ accounts for the spatial variation in coil sensitivity over the object

[6] such as would be the case following a 90° RF pulse for a sample at uniform frequency ω_0

where the effective spin density has been introduced:

$$\rho(\vec{r}) = \omega M_0(\vec{r})(B_1(\vec{r})/i)K. \tag{2.34}$$

Here $B_1(\vec{r})/i$ is the magnitude of $\vec{B}_1(\vec{r})/i$ in the transverse plane, and K is a (complex) constant including amplifier gain and the phase offset between the transverse components of $\vec{M}$ and $\vec{B}_1(\vec{r})/i$ at $t = 0$. Demodulated at the Larmor frequency, or, equivalently, viewed in the rotating frame, the signal is expressed:

$$\tilde{S}(t) = \int \rho(\vec{r}) \exp(-i\Delta\omega(\vec{r})t)dV, \tag{2.35}$$

where $\Delta\omega = \omega - \omega_0$ is the offset from the Larmor frequency. Note that, since the MRI signal depends on the magnitude of the transverse magnetization, the term "signal" is often used to refer to the magnitude of the transverse magnetization.

2.7 Relaxation

2.7.1 Spin-lattice relaxation

The application of an RF pulse disturbs the thermal equilibrium (which gives rise to the equilibrium magnetization $\vec{M} = M_0\hat{z}$) between the nuclear spins and their surroundings, collectively referred to as the lattice. The spins return to equilibrium by exchanging energy with the lattice in a process known as spin-lattice relaxation. Spin-lattice relaxation is described by the phenomenological differential equation:

$$\frac{dM_z}{dt} = \frac{M_0 - M_z}{T_1}, \tag{2.36}$$

where M_z is the z-component of the magnetization vector (the component in the direction of the external magnetic field $B_0\hat{z}$), M_0 is the length of the equilibrium magnetization vector ($\vec{M} = M_0\hat{z}$), and T_1 is a characteristic time-constant. This equation has solution:

$$M_z(t) = M_0 + (M_z(0) - M_0)\exp(-t/T_1). \tag{2.37}$$

Most biological tissues have T_1 time-constants between 250 ms and 5 s. Figure 2.3a shows the regrowth of magnetization toward equilibrium following the application of a 90° RF pulse.

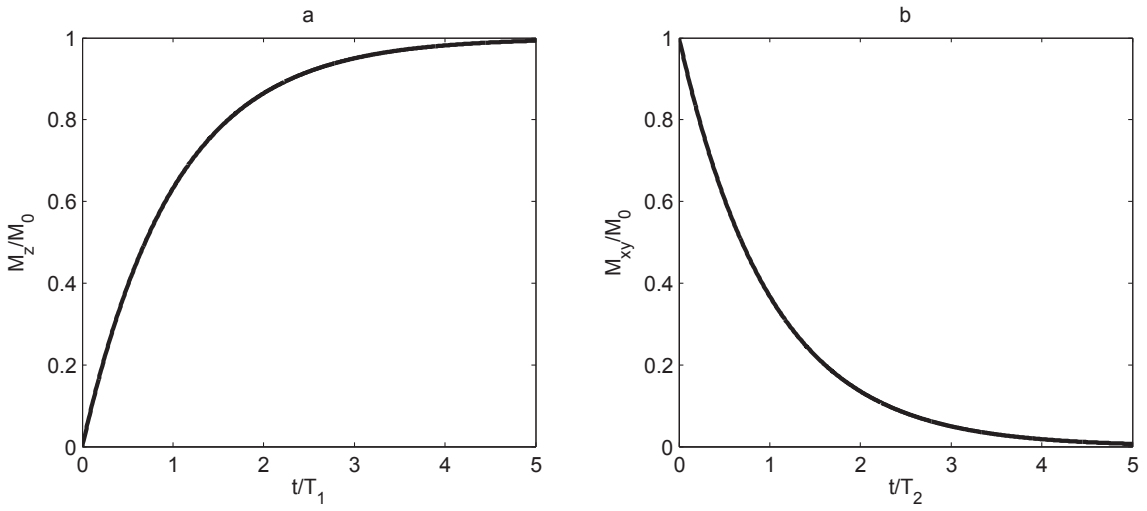

Figure 2.3: Regrowth of longitudinal magnetization (a) and decay of transverse magnetization (b) following a 90° RF pulse.

The theory of relaxation is complicated and analytic expressions for T_1 typically require several simplifying assumptions to be made. Bloembergen, Purcell, and Pound [27] developed a theory (commonly referred to as BPP theory) for relaxation by considering nuclear magnetic dipole-dipole interactions as a time-dependent perturbation to the Zeeman Hamiltonian (which describes the energy for a single spin in an external magnetic field).

Time-dependent perturbations in the magnetic field experienced by a nucleus can cause stimulated absorption or emission of energy quanta $\hbar\omega_0$, inverting the orientation of the nuclear magnetic moment. This is most likely when the perturbations are at the Larmor frequency ω_0. The equilibrium magnetization $\vec{M}_0$ is the result of a balance between stimulated absorption and emission. When an RF pulse creates an excess in the number of spin states anti-aligned with the main field, stimulated emission dominates, returning the system to equilibrium.

T_1 relaxation is dominated by molecular motions at ω_0 and $2\omega_0$. The ω_0 dependence accounts for the Larmor-frequency oscillation induced at nucleus i by the z-component of the magnetic moment of nucleus j, when nucleus j is moving relative to i with frequency ω_0 [27]. The $2\omega_0$ dependence is understood by decomposing the oscillating magnetic field $\cos(\omega_0 t)$ induced at nucleus i by precessing nucleus j. Decomposing this into rotating and counter-rotating components $\cos(\omega_0 t) =$

$(1/2)(\exp(-i\omega_0 t) + \exp(i\omega_0 t))$, motion of nucleus j relative to i with frequency $2\omega_0$ allows the previously ineffectual counter-rotating component at $-\omega_0$ to induce a transition at i [27].

2.7.2 Spin-spin relaxation

The return of the longitudinal magnetization to equilibrium alignment with the main field implies a decay in the transverse magnetization. Spin-lattice interactions play a role in the decay of transverse magnetization, however, additional processes referred to as spin-spin interactions also contribute (and often dominate) transverse magnetization decay. Spin-spin relaxation is described by the phenomenological differential equation:

$$\frac{dM_{xy}}{dt} = \frac{-M_{xy}}{T_2}, \tag{2.38}$$

with time constant T_2, where $M_{xy} = \sqrt{M_x^2 + M_y^2}$ is the length of the magnetization vector perpendicular to the external field. This equation has solution

$$M_{xy}(t) = M_{xy}(0)\exp(-t/T_2). \tag{2.39}$$

The T_2 relaxation times for most biological tissues range from 50 ms to 2 s. Figure 2.3b shows the decay of transverse magnetization following the application of a 90° RF pulse.

Qualitatively, spin-spin relaxation results from the dephasing of the nuclear magnetic moments that compose the magnetization vector. Each nuclear magnetic moment experiences a slightly different magnetic field due to the position and orientation of its neighbouring magnetic moments. As a result of this, the nuclear magnetic moments that compose the magnetization precess at slightly different frequencies, resulting in a loss of phase coherence and therefore a decrease in the length of the magnetization vector with time.

T_2 relaxation is dominated by molecular motion at low frequency. Molecular motion at high frequency results in a time-averaged field of zero at a given nucleus, and is less effective at dephasing the nuclear magnetic moments. Thus the T_2 relaxation times of liquids, such as pure water (about 2 s), tend to be much longer than that of solids, such as ice (about 10 μs) [27].

2.7.3 Relaxation due to macroscopic magnetic field inhomogeneities

In addition to the dephasing that results from microscopic magnetic field inhomogeneities (T_2), dephasing also results from macroscopic magnetic field inhomogeneities, such as those caused by a spatially-varying B_0 field. B_0 inhomogeneity can result from imperfect magnet design or from susceptibility-induced magnetic field gradients that arise when an object with spatially-varying magnetic susceptibility (such as the human brain) is placed in a homogeneous magnetic field. Magnetic field inhomogeneity causes additional dephasing, described by the relaxation time T_2'. Under such circumstances the T_2^* relaxation time is used to describe the decay of transverse magnetization

$$1/T_2^* = 1/T_2 + 1/T_2', \tag{2.40}$$

which includes irreversible spin-spin dephasing (T_2) and reversible (see section 2.9.2 below) macroscopic magnetic field inhomogeneity dephasing T_2'. In human MRI, T_2^* is often dominated by T_2'.

The assumption of an exponential decay for the transverse magnetization in the presence of macroscopic magnetic field inhomogeneity is not valid under many circumstances, and should be used with caution. Even for the relatively simple case of a cubic voxel in the presence of a linearly-varying magnetic field, the signal decays according to a sinc function rather than an exponential. In general, the signal evolution is obtained by integration over the volume of interest (eq. (2.35)):

$$S(t) = \int \rho(\vec{r}) \exp(-i\Delta\omega(\vec{r})t) dV. \tag{2.41}$$

If $S(t) \approx S_0 \exp(-t/T_2')$, an exponential signal decay can be assumed.

2.8 The Bloch Equations

Combining the equations describing precession (eq. (2.19)) and relaxation (eqs. (2.36) and (2.38)) gives the Bloch equations - the (macroscopic) equations of motion for the magnetization:

$$\frac{d\vec{M}}{dt} = \gamma\vec{M} \times \vec{B}_{ext} + \frac{M_0 - M_z}{T_1}\hat{z} - \frac{\vec{M}_{xy}}{T_2}, \tag{2.42}$$

where $\vec{B}_{ext}$ represents the external magnetic field. Note that the Bloch equation assumes $\vec{B}_{ext} = B_0\hat{z} + \vec{B}$, with $|\vec{B}| << B_0$, such that the equilibrium magnetization

vector points in the z-direction with amplitude M_0. This is the case during the application of an RF pulse, as $B_1 << B_0$.

2.8.1 Piecewise solution of the Bloch equations

Basic MRI pulse sequences involve alternate periods of RF excitation (the application of an RF pulse to perturb the magnetization), and free precession, during which the MRI signal is measured (and no RF pulse is applied). The Bloch equations can be used to determine the behaviour of the MRI signal due to an arbitrary sequence of RF pulse and free precession periods.

In many MRI pulse sequences, the duration of the RF pulse τ_{rf} is much shorter than the T_1 and T_2 relaxation times, and the frequency ω_1 of the pulse is much larger than the off-resonance frequency $\Delta\omega = \omega - \omega_0$[7] When this is the case, relaxation and off-resonance precession can be neglected during the application of the RF pulse. This permits a piecewise solution of the Bloch equations to be used, where a pulse sequence is divided into RF pulse and free precession pieces.

During the application of an RF pulse applied along the $\hat{x}$-axis in the rotating reference frame, with relaxation and off-resonance precession neglected, the Bloch equations (eq. (2.42)) reduce to eq. (2.26). As previously illustrated (Fig. 2.2), in this case the Bloch equations describe the precession of the magnetization vector about the $\hat{x}$-axis in the rotating reference frame:

$$\begin{aligned} M_x(t') &= M_x(t_0) \\ M_y(t') &= \cos(\omega_1 t') M_y(t_0) + \sin(\omega_1 t') M_z(t_0) \\ M_z(t') &= -\sin(\omega_1 t') M_y(t_0) + \cos(\omega_1 t') M_z(t_0), \end{aligned} \tag{2.43}$$

where $t' = t - t_0$, $0 \leq t' \leq \tau_{rf}$, and it has been assumed that the RF pulse is applied from time $t = t_0$ to $t = t_0 + \tau_{rf}$.

Between RF pulses, the magnetization undergoes relaxation and off-resonance precession, where $\Delta\omega = \omega - \omega_0$ is the off-resonance frequency. In the rotating reference frame, this is described by the Bloch equations (eq. (2.42)) with $\vec{B}_{ext} = (\Delta\omega/\gamma)\hat{z}$. As $\vec{B}_{ext}$ is along the z-axis, the z-component of $\gamma\vec{M} \times \vec{B}_{ext}$ is zero, and the z-component

[7]RF pulse durations are typically on the order of 1 ms, whereas T_1 and T_2 relaxation times for most human tissues are on the order of 50-4000 ms; ω_1 is typically on the order of 1 kHz, whereas $\Delta\omega$ is typically less than 100 Hz throughout the majority of the brain.

of eq. (2.42) reduces to eq. (2.36), solved previously (eq. (2.37)). The transverse component of the Bloch equations is:

$$\frac{dM_{xy}}{dt} = -i\Delta\omega M_{xy} - M_{xy}/T_2, \tag{2.44}$$

where complex notation $M_{xy} = M_x + iM_y$ has been used. This equation has solution $M_{xy}(t) = M_{xy}(0)\exp(-t/T_2)\exp(-i\Delta\omega t)$, which is a combination of relaxation (eq. (2.39)) and precession (eq. (2.20)). Combining longitudinal (M_z) and transverse (M_{xy}) components, the behaviour of the magnetization during free precession is:

$$\begin{aligned} M_{xy}(t') &= M_{xy}(t_0)\exp(-t'/T_2)\exp(-i\Delta\omega t') \\ M_z(t') &= M_z(t_0)\exp(-t'/T_1) + M_0(1-\exp(-t'/T_1)), \end{aligned} \tag{2.45}$$

where $t' = t - t_0$, $0 \le t' \le \tau_{fp}$, and it has been assumed that free precession occurs from time $t = t_0$ to $t = t_0 + \tau_{fp}$.

For a general pulse sequence consisting of alternate periods of RF excitation[8] and free precession, these solutions to the Bloch equations (eqs. (2.43) and (2.45)) can be used piecewise to obtain the magnetization behaviour, with the initial magnetization vector for period $(n+1)$ set equal to the final magnetization vector from period n.

2.9 Basic Pulse Sequences

2.9.1 Free Induction Decay

The simplest pulse sequence is the free induction decay (FID) - measurement of the MRI signal following the application of a single RF pulse. The signal, in the rotating frame, is given by:

$$S(t) = \int \rho(\vec{r})\exp(-t/T_2)\exp(-i\Delta\omega(\vec{r})t)dV, \tag{2.46}$$

where $\Delta\omega = \omega - \omega_0$ is the off-resonance frequency at position $\vec{r}$, dV is a sample volume element, $\rho(\vec{r})$ is the effective spin density (eq. (2.34)), and it has been assumed that T_2 is independent of position.

Figure 2.4 shows the FID signal and frequency spectrum (Fourier transform of the signal) for a sample containing two pools of spins, at different resonant frequencies, in a homogeneous magnetic field. Such a signal could originate from a fat-water mixture,

[8] assuming, as above, that relaxation and free precession can be ignored during the application of the RF pulse

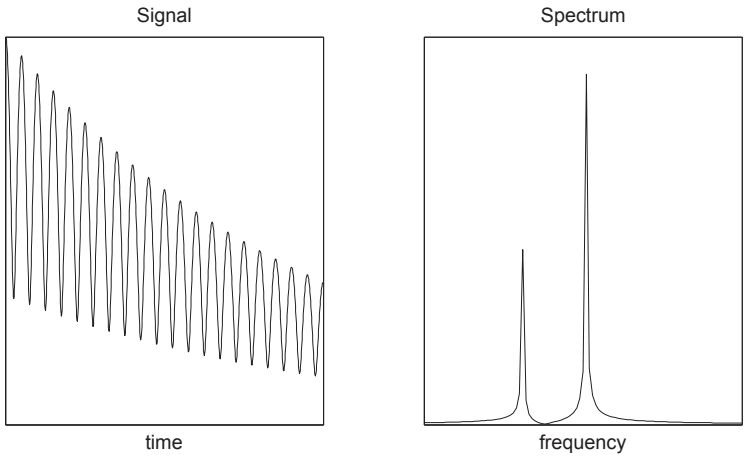

Figure 2.4: Signal vs. time (left) and Spectrum (Fourier transform of the signal) vs. frequency for a sample containing two spin pools at different resonant frequencies.

for example. Protons in fat and water molecules precess at different frequencies because the magnetic moments of neighboring electrons perturb the magnetic field at the nucleus, and the electron structure surrounding fat and water protons differ. NMR spectroscopy takes advantage of this to determine the chemical composition of unknown substances.

One use of the FID pulse sequence in MRI is for magnetic field shimming. Inhomogeneities in the main magnetic field result in a rapid decay of the FID signal through phase cancellation in the $\int \exp(-i\Delta\omega(\vec{r})t)dV$ integral. After placing an object in the magnetic field, small spatially-varying magnetic fields (shim gradients) are added to the main field to maximize the lifetime of the FID, thereby improving magnetic field homogeneity across the object.

2.9.2 The Spin-Echo

It was mentioned in section 2.7.3 that macroscopic magnetic field inhomogeneity dephasing (T_2') could be reversed. This can be achieved using a spin-echo sequence.

A basic spin-echo sequence consists of a 90° RF pulse applied about the x-axis[9] followed by a 180° "re-focusing" RF pulse applied about the y-axis at time $T_E/2$ later. The initial 90° RF pulse tips spin isochromats[10] to the y-axis, where they will

[9] all RF pulse rotations are with respect to the rotating reference frame
[10] A group of spins sharing a common resonance frequency

begin to dephase relative to each other because of differences in their local z-directed magnetic fields. Consider the phase gained by a general isochromat relative to the y-axis:

$$\phi(\vec{r},t) = -\gamma\Delta B(\vec{r})t \quad \text{for } 0 < t < T_E/2, \tag{2.47}$$

where ΔB is the offset from the externally applied magnetic field. At time $t = T_E/2$, the 180° pulse reflects the phase about the y-axis:

$$\begin{aligned}\phi(\vec{r},T_E/2^+) &= -\phi(\vec{r},T_E/2^-) \\ &= \gamma\Delta B(\vec{r})T_E/2,\end{aligned} \tag{2.48}$$

where - (+) represents the time immediately before (after) the RF pulse. After the 180° pulse, the spins will continue to gain phase as they did prior to the 180° pulse if $\Delta B(\vec{r})$ is time-invariant:

$$\begin{aligned}\phi(\vec{r},t) &= \gamma\Delta B(\vec{r})T_E/2 - \gamma\Delta B(\vec{r})(t - T_E/2) \quad \text{for } t > T_E/2 \\ &= -\gamma\Delta B(\vec{r})(t - T_E).\end{aligned} \tag{2.49}$$

At the echo time, T_E, the phase gained due to a general static magnetic field inhomogeneity is zero. The only source of signal decay is that resulting from irreversible T_2 decay:

$$S(t) \propto M_0 \exp(-T_E/T_2). \tag{2.50}$$

Figure 2.5 shows the spin isochromat behavior during a basic spin-echo sequence.

The ability of a spin-echo sequence to refocus dephasing caused by magnetic field inhomogeneities that vary in both space and time $\Delta B(\vec{r},t)$ depends on the correlation time τ_c of the magnetic field fluctuations (the time-span over which there is appreciable autocorrelation) relative to the echo time, T_E.

The microscopic magnetic field fluctuations leading to T_2 decay ($\tau_c < 10^{-9}$ s) are not refocused by spin-echo sequences at typical echo times ($\approx$ 10-100 ms) as $\tau_c << T_E$. Conversely, static magnetic field inhomogeneities have an effectively infinite correlation time and are completely refocused as $\tau_c >> T_E$. For magnetic field fluctuations having correlation times on the order of the echo time, partial refocusing occurs. In these cases, the apparent T_2 relaxation time depends on the echo time (the apparent T_2 increases as echo time decreases, and vice versa).[11]

[11] this is the case for the intravascular T_2-like effect in functional MRI (see eqs. (3.3) and (3.4)).

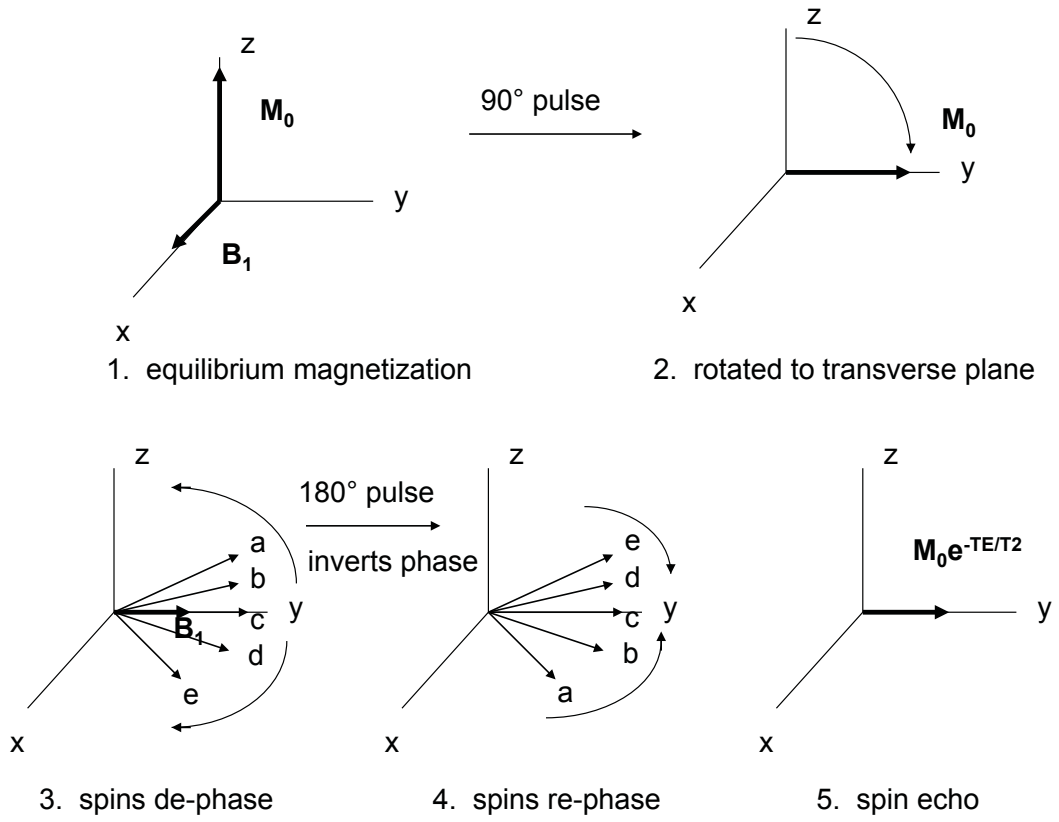

Figure 2.5: Isochromat behavior during a basic spin-echo sequence. RF pulses are represented by the vector $\vec{B}_1$. Each isochormat is at a constant off-resonance frequency (for example, isochromat "a" precesses counterclockwise by $\approx 45°$ between the 90° and 180° pulse (elapsed time $T_E/2$), and between the 180° pulse and the echo time (elapsed time $T_E/2$)).

2.10 Selective Excitation

So far, RF pulses have been considered which excite magnetization across the entire object. It is also possible to only excite magnetization over a thin region of the object, referred to as slice selection. Slice selection is achieved by applying a magnetic field gradient $\vec{G}$

$$\vec{G} = \nabla B_z(\vec{r}) \tag{2.51}$$

to create a spread of larmor frequencies across the object. Here we will consider a z-directed magnetic field gradient, $\vec{G} = G\hat{z}$, producing a z-dependent larmor frequency:

$$\omega(z) = \gamma B_0 + \gamma G z. \tag{2.52}$$

An RF pulse is then applied in the presence of this gradient, where the frequency spectrum of the RF pulse is chosen to match the frequency spectrum, imposed by the gradient, over the desired slice to be excited (Fig. 2.6). Selective excitation as described here relies on some simplifying assumptions, which are discussed in the next section.

2.10.1 Selective Excitation: Theory

Consider the application of a time-varying RF pulse $B_1(t)$, applied along the x-axis in the rotating reference frame ($\vec{\Omega} = -\gamma B_0 \hat{z}$), in the presence of a magnetic field gradient $\vec{G} = G\hat{z}$. The effective field in the rotating frame ($(\vec{B} + \vec{\Omega}/\gamma)$, eq. (2.24)) is $(B_1(t)\hat{x} + Gz\hat{z})$. Neglecting relaxation (valid if the duration of the RF pulse is much less than the T_1 and T_2 relaxation times), the rate of change of the magnetization in the rotating reference frame is given (eq. (2.42) without relaxation terms, i.e., eq. (2.24)):

$$\frac{d\vec{M}}{dt} = \gamma \vec{M} \times (B_1(t)\hat{x} + Gz\hat{z}), \tag{2.53}$$

which, when separated into components, becomes:

$$\begin{aligned} \frac{dM_x}{dt} &= \gamma G z M_y \\ \frac{dM_y}{dt} &= \gamma \left(B_1(t) M_z - G z M_x\right) \\ \frac{dM_z}{dt} &= -\gamma B_1(t) M_y. \end{aligned} \tag{2.54}$$

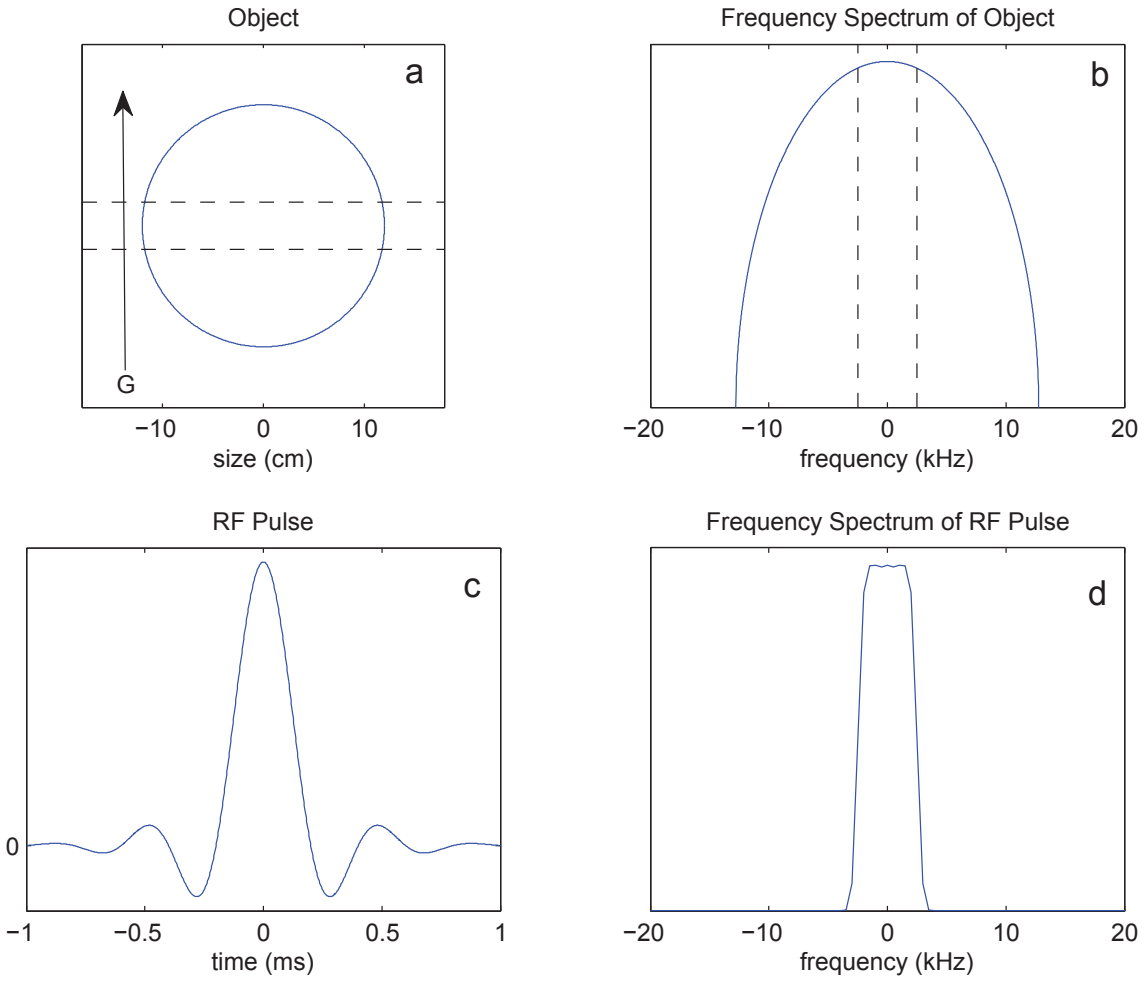

Figure 2.6: Illustration of slice selection. A magnetic field gradient (a) is applied to create a spread of larmor frequencies across the object (b). An RF pulse (c) is then applied with a frequency spectrum (d) corresponding to that of the desired slice to be excited.

If we assume a small tip angle α such that $\sin\alpha \approx \alpha$ and $\cos\alpha \approx 1$, then $M_z \approx M_0$, $dM_z/dt \approx 0$, and eq. (2.54) can be approximated:

$$\begin{aligned} \frac{dM_x}{dt} &= \gamma G z M_y \\ \frac{dM_y}{dt} &= \gamma \left(B_1(t) M_0 - G z M_x\right) \\ \frac{dM_z}{dt} &= 0, \end{aligned} \tag{2.55}$$

which can be expressed in complex ($M_{xy} = M_x + iM_y$) form:

$$\frac{dM_{xy}}{dt} = -i\gamma G z M_{xy} + i\gamma M_0 B_1(t). \tag{2.56}$$

For an RF pulse $B_1(t)$ of duration τ_{rf}, applied from $-\tau_{rf}/2$ to $\tau_{rf}/2$ with $B_1(t) = 0$ outside of this interval, and the initial condition $M_{xy}(-\tau_{rf}/2) = 0$, eq. (2.56) has solution:

$$M_{xy}(z, \tau_{rf}/2) = i\gamma M_0 \exp(-i\gamma G z \tau_{rf}/2) \int_{-\tau_{rf}/2}^{\tau_{rf}/2} dt B_1(t) \exp(i\gamma G z t). \tag{2.57}$$

We can extend the limits of eq. (2.57) to $\pm\infty$, since $B_1(t)$ is only non-zero for $t \in [-\tau_{rf}/2, \tau_{rf}/2]$. Equation 2.57 then becomes an inverse Fourier transform:

$$M_{xy}(z, \tau_{rf}/2) = i\gamma M_0 \exp(-i\gamma G z \tau_{rf}/2) b_1(\gamma G z), \tag{2.58}$$

where $b_1(f)$ represents the inverse Fourier transform of $B_1(t)$. Two important relationships can be deduced from eq. (2.58): 1) the magnitude of the excited magnetization at position z is proportional to the magnitude of the B_1 spectrum at frequency $\gamma G z$, and 2) for an RF pulse that is symmetric about $t = 0$ (resulting in a real Fourier transform), the excited magnetization has spatially-varying phase in the z-direction $\exp(-i\gamma G z \tau_{rf}/2)$ at the end of the RF pulse. This spatially-varying phase is undesirable, as it diminishes the slice signal through vector cancellation. Luckily this phase dispersion can be easily removed. The phase gain that results from applying a gradient $G\hat{z}$ for duration τ is:

$$\phi(z) = -\gamma \Delta B \tau = -\gamma G z \tau. \tag{2.59}$$

Thus the unwanted phase dispersion can be removed by applying the slice-select gradient, with opposite polarity, for one-half of the duration of the RF pulse (fig. 2.7).

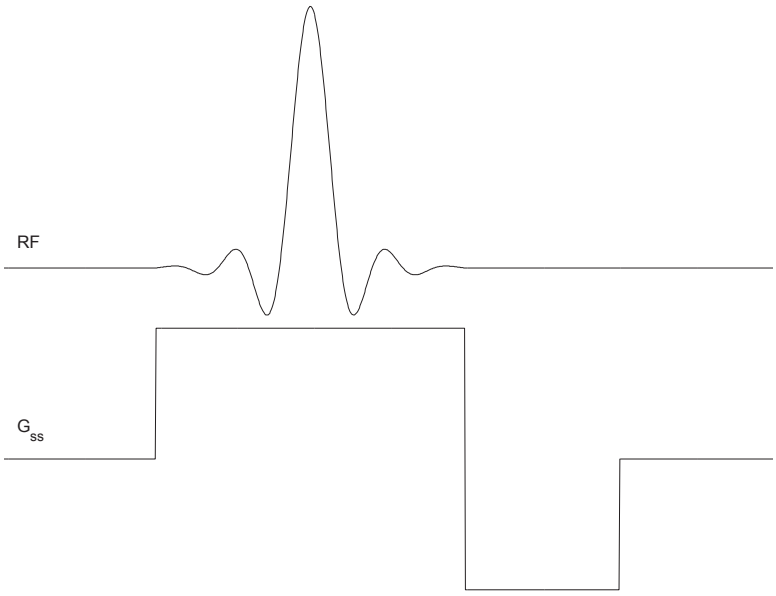

Figure 2.7: Slice Selection with Refocusing. A symmetric, small-tip-angle, slice-selective RF pulse results in a phase dispersion across the selected slice. This can be removed with a slice-select refocusing gradient having the same magnitude, opposite polarity, and one-half of the duration of the slice select gradient.

Despite assuming a small tip angle, the Fourier transform relationship between the RF pulse and the excited magnetization (eq. (2.58)) holds quite well for tip angles up to 90°. For the design of high-flip-angle RF pulses, the reader is referred to the the Shinnar-Le Roux (SLR) algorithm [28].

2.11 Imaging

NMR imaging (MRI) is achieved by adding a spatially-varying magnetic field gradient $\vec{G}$:

$$\vec{G} = \nabla B_z(\vec{r}), \tag{2.60}$$

to the main field, creating a position-dependent precession frequency:

$$\omega(\vec{r}) = \gamma B_0 + \gamma \vec{G} \cdot \vec{r}. \tag{2.61}$$

The signal in the presence of a gradient is expressed (eq. (2.35)):

$$S(t) = \int \rho(\vec{r}) \exp(-i\gamma \vec{G} \cdot \vec{r}t) dV, \tag{2.62}$$

which has the form of a Fourier transform. This relationship is clarified by defining a reciprocal **k**-space vector having units of m^{-1}:

$$S(\vec{k}) = \int \rho(\vec{r}) \exp(-i2\pi\vec{k}\cdot\vec{r})dV, \tag{2.63}$$

with

$$\begin{aligned} \vec{k} &= \frac{\gamma\vec{G}t}{2\pi} \\ &= \gamma\vec{G}t. \end{aligned} \tag{2.64}$$

The effective spin-density is obtained from the signal via the inverse Fourier transform:

$$\rho(\vec{r}) = \int S(\vec{k}) \exp(i2\pi\vec{k}\cdot\vec{r})dk_x dk_y dk_z. \tag{2.65}$$

In practice the signal is uniformly[12] sampled at discrete locations in **k**-space and the image is generated via the inverse discrete Fourier transform (IDFT). The IDFT produces shifted, overlapping copies (aliases) of the image whose spacing $1/(\Delta k)$ is determined by the inverse of the sampling interval in conjugate space Δk. The periodicity of the DFT determines how finely the 3D **k**-space matrix must be sampled to avoid aliasing:

$$\frac{1}{\Delta k_i} = N_i \Delta x_i = \mathrm{FOV}_i \geq X_i, \tag{2.66}$$

where Δk_i is the sampling interval in the i^{th} dimension, N_i is the number of sampled points, Δx_i is the sampling interval in conjugate space (the image resolution), $N\Delta x_i = \mathrm{FOV}_i$ is the field of view (the distance between shifted image copies), and X_i is the size of the object. Equation 2.66 also determines the extent $K_i = N_i \Delta k_i$ that must be covered in **k**-space to achieve a desired image resolution: $K_i = 1/(\Delta x_i)$. Figure 2.8 depicts the sampling relationship between image-space and **k**-space. Figure 2.9 shows a 2D representation of a human brain in **k**-space and image-space.

Imaging amounts to moving through **k**-space, sampling the signal at each matrix point, and applying an IDFT. Magnetic field gradients are used to move through **k**-space, with direction and speed determined by $\vec{G}$, and γG, respectively (eq. (2.64)). The amount of **k**-space that can be sampled following a single RF excitation depends on the capabilities of the gradient hardware, the T_2 (spin echo) or (T_2^*) (gradient echo) relaxation time, and the strength of the magnetic field gradients from unwanted

[12] or interpolated onto a uniform grid

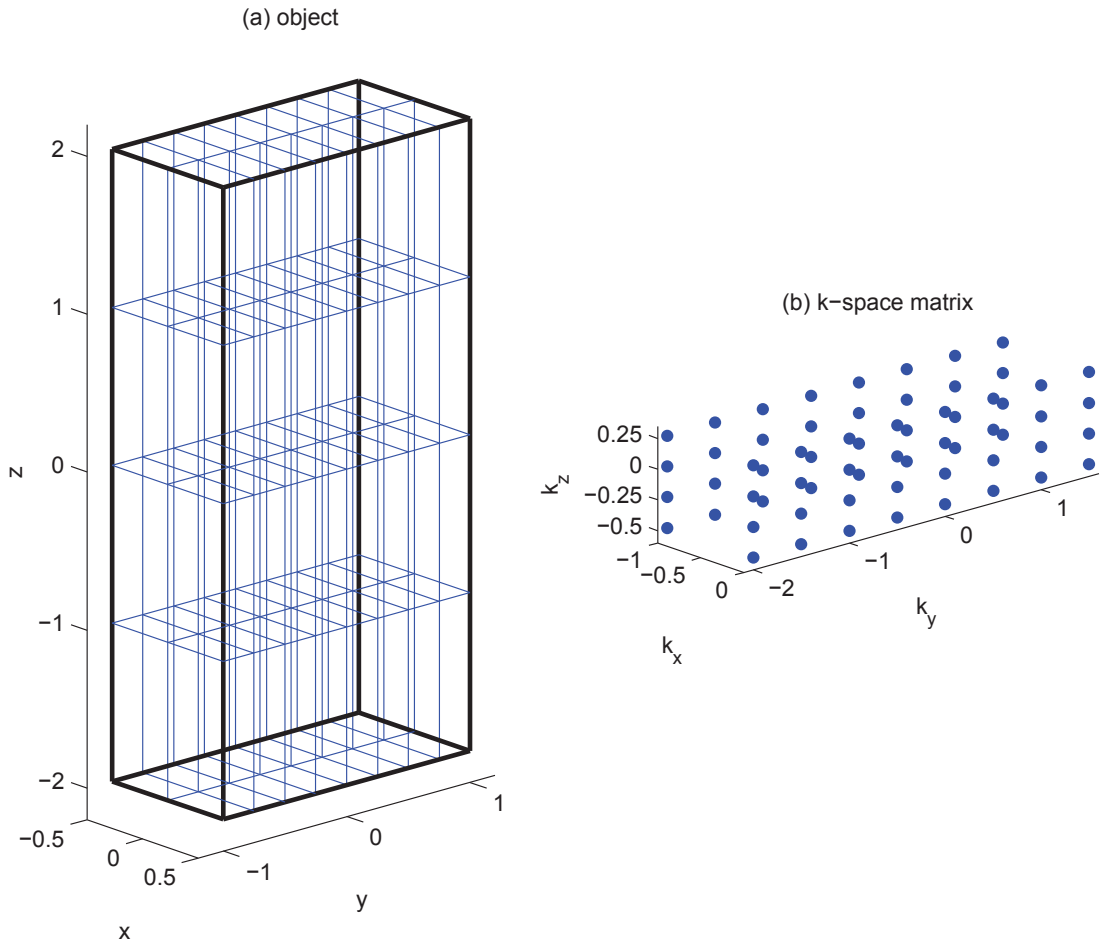

Figure 2.8: The **k**-space matrix (b) that must be sampled to image the rectangular object (a, outlined in black) at the depicted resolution (blue rectangular voxels in object). As the object is largest in the z-dimension, the k_z dimension is most densely sampled. As the desired resolution is highest in the y-dimension, the k_y dimension is largest.

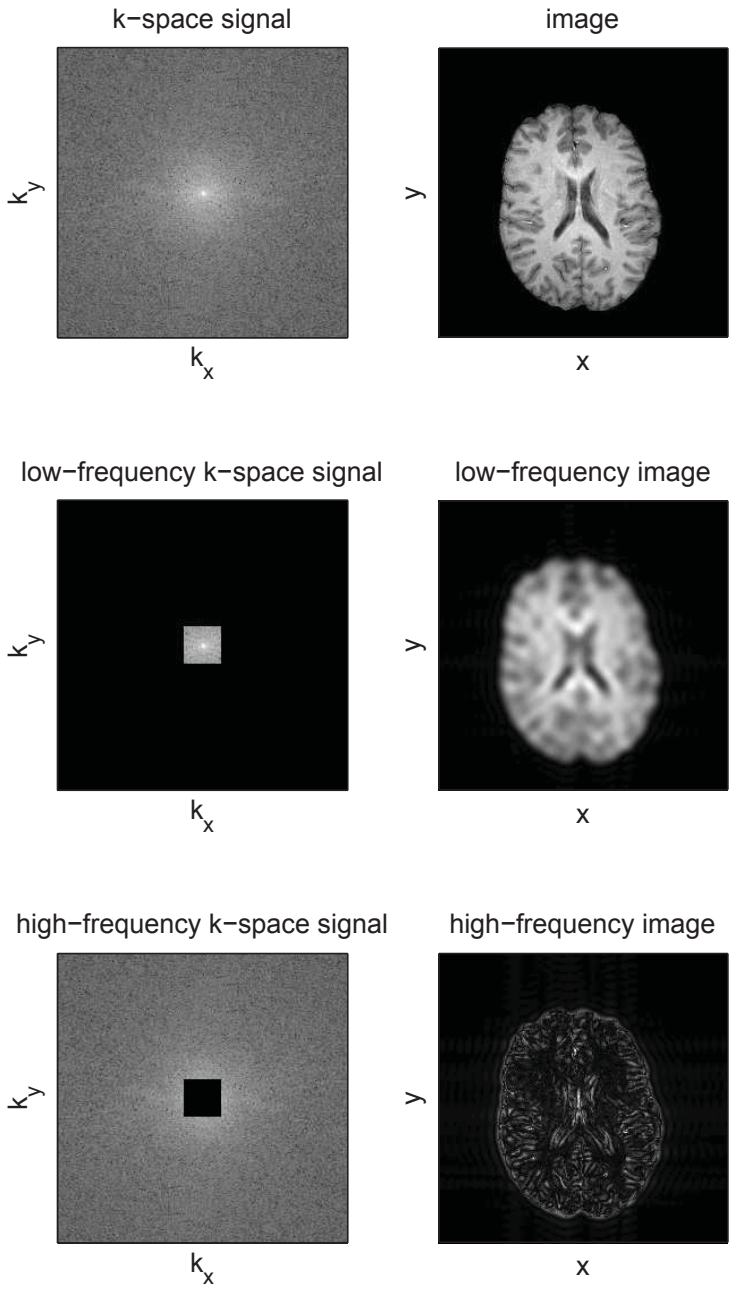

Figure 2.9: The **k**-space signal and corresponding image (Fourier-transformed signal) are shown for: the entire **k**-space (top row), the low-spatial-frequency (centre) of **k**-space (middle row), and the high-spatial-frequency (periphery) of **k**-space (bottom row). Most of the image intensity and tissue contrast in the human brain is at low spatial frequency. High spatial frequencies denote boundaries. Note that the **k**-space signal has been plotted on a logarithmic intensity scale.

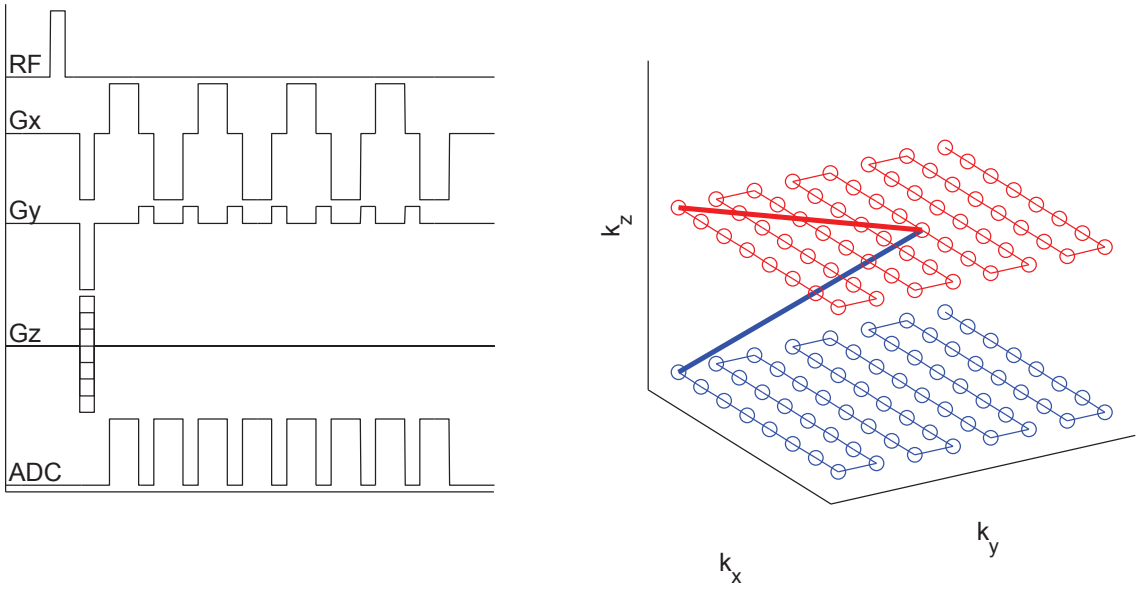

Figure 2.10: 3D GRE stack-of-EPI pulse sequence (left) and resulting **k**-space trajectory (right). Depicted in the pulse sequence are the status of the RF transmitter (RF), x, y, and z gradients (G_x, G_y, and G_z, respectively), and the analog-to-digital converter (ADC) (receiver), all of which are off to begin. An entire plane in **k**-space is acquired every RF excitation. The entire pulse sequence is repeated for each k_z-value (G_z is depicted in steps to represent this).
Only two planes are depicted in the **k**-space trajectory (right) for clarity. Each trajectory begins at the **k**-space centre, proceeds to the bottom-left-corner of the appropriate **k**-space plane, and then traverses the plane. Data are acquired at each point required for IDFT image formation, depicted as open circles.

sources, which create unwanted phase variations across the object in proportion to the acquisition duration, resulting in image distortion. Rapid imaging sequences, such as single-shot GRE-EPI[13], can acquire an entire **k**-space plane per RF excitation. Imaging sequences are classified as 2D or 3D depending if slice selection (2D) or gradient-encoding (3D) is used to resolve the z-dimension. A 3D GRE-EPI pulse sequence is depicted in Fig. 2.10. In NMR imaging, the echo time T_E is defined as the elapsed time between the RF excitation pulse and the collection of the **k**-space centre (at which point the phase variation across the object due to the imaging gradients is zero), as this dominates image contrast (e.g., Fig. 2.9).

[13]Gradient echo is a general term used to refer to any pulse sequence consisting of **k**-space encoding following a single RF excitation pulse. The term "gradient echo" refers to the fact that often in GRE sequences the signal is first dephased and subsequently rephased, forming an "echo", by the imaging gradients.

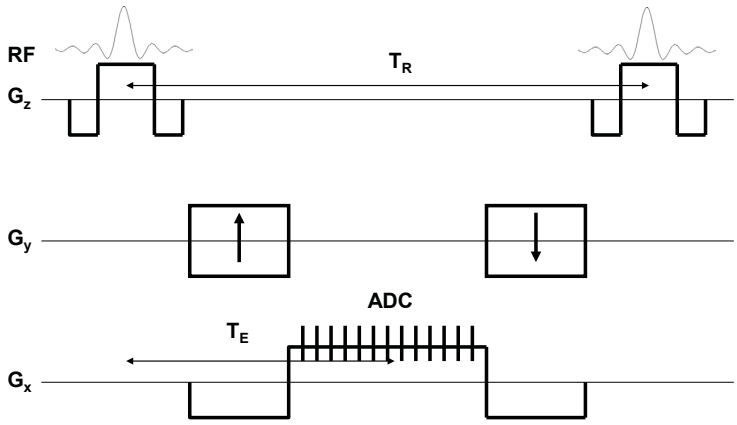

Figure 2.11: 2D (slice-selective) balanced SSFP pulse sequence. All gradients are balanced to have zero area over a T_R cycle.

In applications requiring high resolution (which increases the size of the **k**-space matrix that must be sampled) or reduced distortion (where the readout duration must be reduced), segmented acquisitions can be used, where the acquisition of a **k**-space plane is divided over multiple RF excitations.

2.12 Balanced Steady State Free Precession

Balanced SSFP is similar to a short-T_R gradient echo sequence such as Spoiled Gradient Echo (SPGR), except that instead of spoiling the transverse magnetization at the end of each T_R, all imaging gradients are balanced to have zero integral area over a T_R cycle (fig. 2.11). Thus the only source of phase evolution between RF pulses in b-SSFP is that from free precession.

Gradient refocusing results in the preservation of transverse magnetization from one T_R cycle to the next, making b-SSFP the most SNR-efficient of all known pulse sequences [18] (Fig. 2.12). The preservation of transverse magnetization also results in a complicated signal dependence on off-resonance frequency not seen in gradient echo or spin echo sequences (Fig. 2.13). Even with careful shimming the magnetic field varies across the brain. As a result, balanced SSFP images often contain "banding artifacts" - regions of low signal corresponding to specific values of off-resonance frequency (fig. 1.3a-b on page 7).

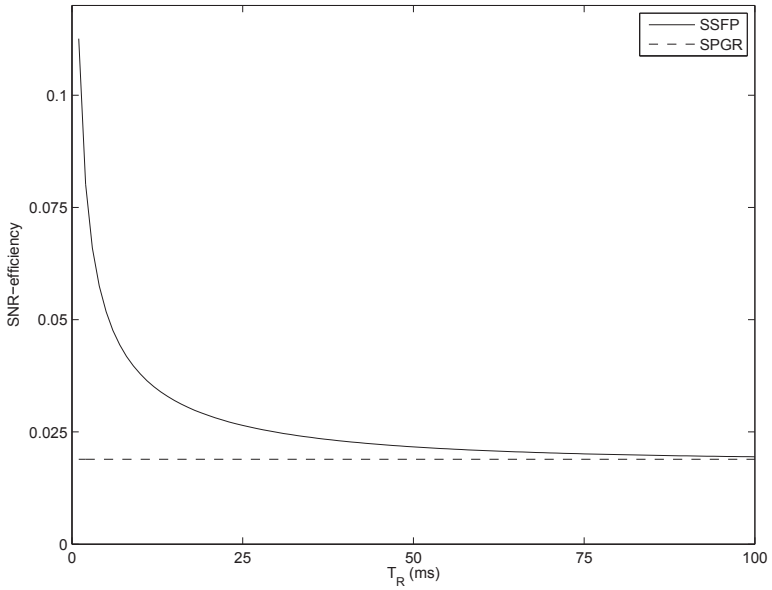

Figure 2.12: SNR-efficiency ($(S/M_0)/\sqrt{T_R}$) vs. T_R for SSFP and SPGR at $T_E = 0$. SNR-efficiency is shown for the signal-optimizing flip angle for each T_R/pulse sequence. Plot parameters: $T_1 = 1400$ ms, $T_2 = 70$ ms (relaxation times typical of human grey matter tissue at 4 T [29])

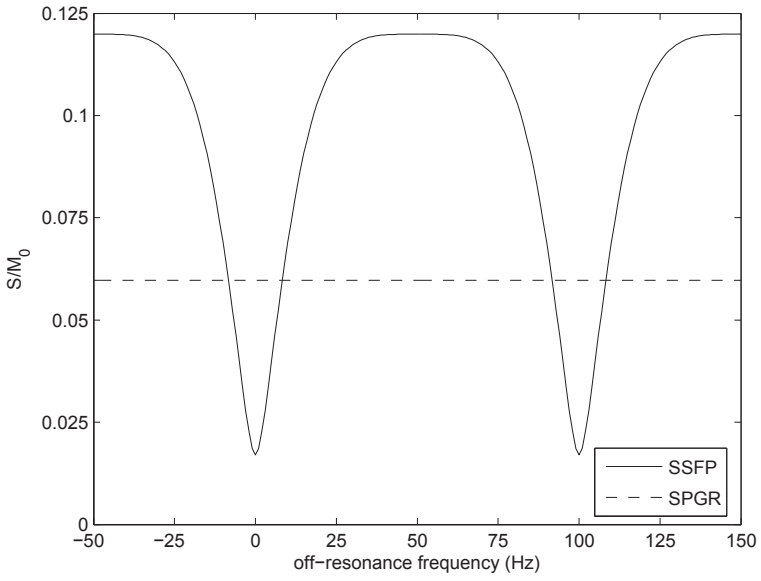

Figure 2.13: Signal vs. off-resonance frequency for SSFP and SPGR at $T_E = 0$. Off-resonance frequency refers to the global voxel frequency offset (the off-resonance frequency is assumed to be uniform across a voxel). Signal is shown for the signal-optimizing flip angle for each pulse sequence. Plot parameters: $T_R = 10$ ms, $T_1 = 1400$ ms, $T_2 = 70$ ms.

2.12.1 Derivation of the b-SSFP Signal Equations

The balanced SSFP pulse sequence consists of a train of identical RF pulses with flip angle α applied periodically with period T_R. After a sufficient number of RF pulses[14], a steady state is reached in which the magnetization is periodic in time, with period T_R.

Below, the balanced SSFP signal equations are derived using the Bloch Equations (section 2.8) in matrix form [20], with the magnetization represented by the 3×1 column vector:

$$\vec{M} = \begin{bmatrix} M_x \\ M_y \\ M_z \end{bmatrix} \tag{2.67}$$

In general, a pulse sequence can be divided into periods of RF excitation and precession/relaxation. If the duration of the RF pulse is much smaller than the T_1 and T_2 relaxation times, relaxation can be ignored during the application of the RF pulse[15]. Here RF pulses are treated as instantaneous clockwise rotations about the x-axis with flip angle α:

$$R_x(\alpha) = \begin{bmatrix} 1 & 0 & 0 \\ 0 & \cos\alpha & \sin\alpha \\ 0 & -\sin\alpha & \cos\alpha \end{bmatrix}. \tag{2.68}$$

Between RF pulses the magnetization undergoes free precession and relaxation for time-duration τ. Precession is characterized by rotation about the z-axis by angle $\theta = \Delta\omega\tau$, where $\Delta\omega$ is the off-resonance frequency:

$$R_z(\tau) = \begin{bmatrix} \cos(\Delta\omega\tau) & \sin(\Delta\omega\tau) & 0 \\ -\sin(\Delta\omega\tau) & \cos(\Delta\omega\tau) & 0 \\ 0 & 0 & 1 \end{bmatrix} \tag{2.69}$$

Relaxation is characterized by magnetization decay:

$$D(\tau) = \begin{bmatrix} \exp(-\tau/T_2) & 0 & 0 \\ 0 & \exp(-\tau/T_2) & 0 \\ 0 & 0 & \exp(-\tau/T_1) \end{bmatrix}, \tag{2.70}$$

[14] see section 2.12.3 for a discussion of the approach to steady state

[15] for human imaging at 4 T, typical RF pulse durations are 1-4 ms, while typical grey matter relaxation times are $T_1 \approx 1400$ ms and $T_2 \approx 70$ ms

and magnetization regrowth in the z-direction:

$$\vec{B}(\tau) = (1 - \exp(-\tau/T_1)) \begin{bmatrix} 0 \\ 0 \\ M_0 \end{bmatrix}. \tag{2.71}$$

Using these matrices, the magnetization immediately before the nth RF pulse is related to that immediately before the (n+1)th RF pulse according to:

$$\begin{aligned} \vec{M}_{n+1} &= D(T_R)R_z(T_R)R_x(\alpha)\vec{M}_n + \vec{B}(T_R) \\ &= A\vec{M}_n + \vec{B} \end{aligned} \tag{2.72}$$

Where A is the 3×3 matrix $A = D(T_R)R_z(T_R)R_x(\alpha)$.

The steady state magnetization is obtained by solving eq. (2.72) for $\vec{M}_{n+1} = \vec{M}_n = \vec{M}_{ss}$:

$$\vec{M}_{ss} = (I - A)^{-1}\vec{B}, \tag{2.73}$$

where I represents the 3×3 identity matrix. The solution for the steady state magnetization immediately before an RF pulse (denoted by the minus sign $^-$) is [30]:

$$\begin{aligned} M_x^- &= M_0(1 - E_1)E_2 \sin\alpha \sin\theta / D \\ M_y^- &= M_0(1 - E_1)(E_2 \sin\alpha \cos\theta - E_2^2 \sin\alpha)/D \\ M_z^- &= M_0(1 - E_1)(1 - E_2\cos\theta - E_2\cos\alpha(\cos\theta - E_2))/D, \end{aligned} \tag{2.74}$$

with

$$\begin{aligned} D &= (1 - E_1\cos\alpha)(1 - E_2\cos\theta) - (E_1 - \cos\alpha)(E_2 - \cos\theta)E_2 \\ E_1 &= \exp(-T_R/T_1) \\ E_2 &= \exp(-T_R/T_2). \end{aligned} \tag{2.75}$$

Similarly, the steady state solution for the magnetization immediately after an RF pulse (denoted by the plus sign $^+$) is [30]:

$$\begin{aligned} M_x^+ &= M_0(1 - E_1)E_2 \sin\alpha \sin\theta / D \\ M_y^+ &= M_0(1 - E_1)(1 - E_2\cos\theta)\sin\alpha / D \\ M_z^+ &= M_0(1 - E_1)(E_2(E_2 - \cos\theta) + (1 - E_2\cos\theta)\cos\alpha)/D. \end{aligned} \tag{2.76}$$

The solution for a general echo time T_E ($0 \leq T_E \leq T_R$) is obtained by applying the appropriate precession and relaxation matrices to the magnetization vector given in eq. (2.76) (referred to as $\vec{M}_{ss}^{+}$):

$$\vec{M}_{ss}(T_E) = D(T_E)R_z(T_E)\vec{M}_{ss}^{+} + \vec{B}(T_E). \tag{2.77}$$

We will represent the balanced SSFP signal in complex form:

$$\begin{aligned} S &= M_x + iM_y \\ &= r\exp(i\phi) \end{aligned} \tag{2.78}$$

The balanced SSFP signal magnitude (r) and phase (ϕ) are both periodic in off-resonance angle[16] (Fig. 2.14). The magnitude-period is 360°, while the phase-period is 360° for $T_E = 0$ and $(T_R/T_E)\times 360°$ for $0 < T_E \leq T_R$.[17]

Note that the balanced SSFP signal magnitude, but not the signal phase, varies with flip angle α. The balanced SSFP signal vs. off-resonance profile is typically divided into "pass-band" and "transition-band" regions. The pass-band refers to the region of uniform signal phase vs. off-resonance angle that occurs for $90° < \theta < 270°$ (Fig. 2.14). Signal is maximized in the pass-band for high flip angles (maximum pass-band signal occurs at $\alpha = 25°$ for the chosen values of T_1 and T_2 in this example). The transition-band refers to the region of large signal phase variation with off-resonance angle that occurs in the vicinity of $\theta = 0°$. Signal is maximized in the transition-band for low flip angles ($\alpha = 2°$ in this example).

2.12.2 Phase Cycling

The steady state signal (eq. (2.76)) depends on the relative phase evolution between the RF pulse axis and the transverse magnetization vector during a T_R cycle. For constant-phase RF pulses (each along the x-axis in the derivation of the steady state signal above), this is entirely determined by free precession, $\theta = \Delta\omega T_R$. Of course, the relative phase evolution can also be changed by changing the phase (direction)

[16] The balanced SSFP signal depends on the relative phase between the RF pulse and the transverse magnetization. The phase angle between the RF pulse and the transverse magnetization is the same for spins precessing by θ and $\theta + 2\pi$ during the time between RF excitations, T_R.

[17] the signal phase is not 2π-periodic for $0 < T_E < T_R$; magnetization vectors at off-resonance angles of θ and $\theta + 2\pi$ (precession per T_R time-period) are indistinguishable at integer multiples of T_R, but not for time-points in between.

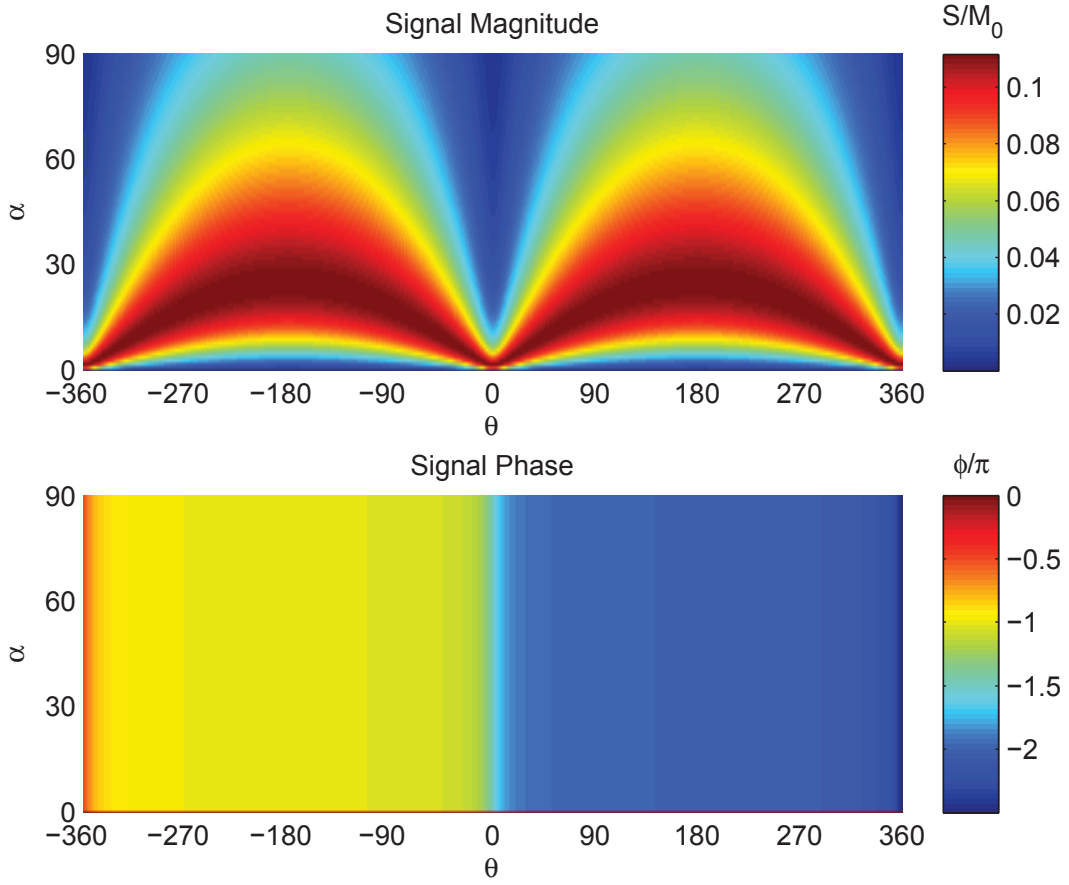

Figure 2.14: balanced SSFP signal magnitude (S/M_0, top, value indicated by color bar) and phase (ϕ, bottom, value indicated by color bar) vs. flip angle α and free precession angle θ, both in degrees. Signal phase is expressed in radians/π. Plot parameters: $T_R = 10$ ms, $T_E = 5$ ms, $T_1 = 1400$ ms, $T_2 = 70$ ms.

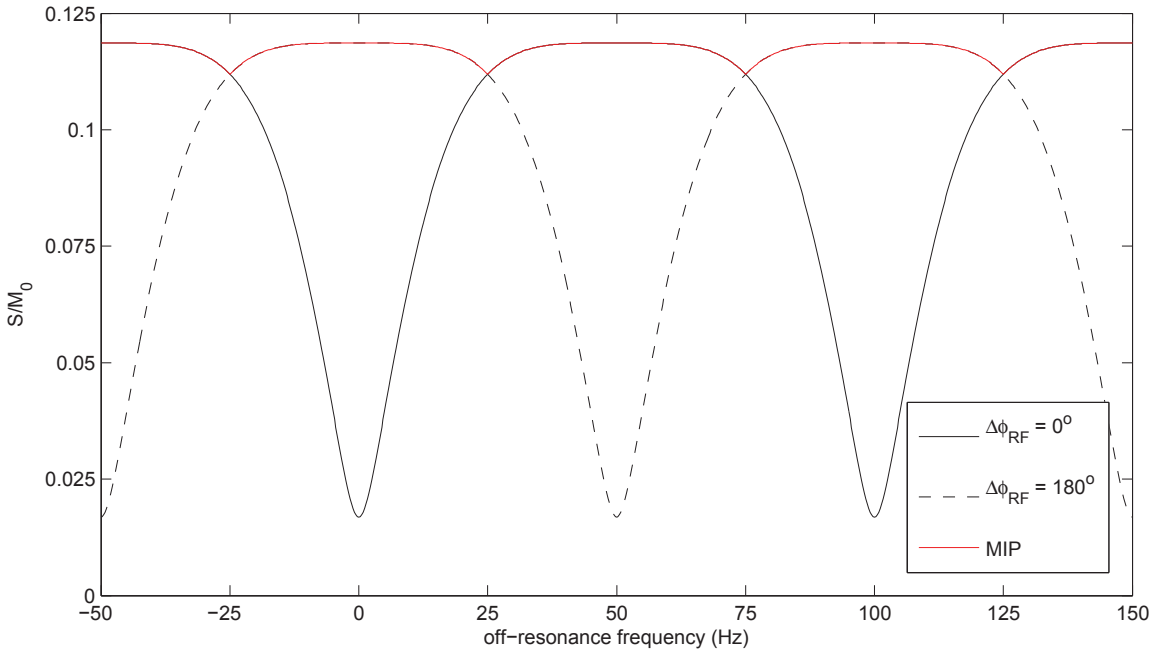

Figure 2.15: Balanced SSFP images obtained from 0°- and 180°-RF-phase-cycled steady states can be combined, via maximum intensity projection (MIP), to produce a single image without banding artifacts.

of the RF pulse axis in the transverse plane, a process known as "phase cycling". In such cases, the relative phase evolution becomes:

$$\theta = \Delta\omega T_R - \Delta\phi_{RF}, \tag{2.79}$$

where $\Delta\phi_{RF}$ is the RF increment - the phase difference between subsequent RF pulses[18].

Two balanced SSFP images obtained from $\Delta\phi_{RF} = 0°$ and $\Delta\phi_{RF} = 180°$ steady states, respectively, can be combined, via maximum intensity projection (where the combined image is created pixel-wise from the component images by choosing the larger of the two pixel intensity values) to produce a single, banding-artifact-free image (Fig. 2.15 and Fig. 1.3c on page 7). Tuning the RF-phase-cycling increment is also referred to as setting the centre frequency.

[18]where a positive increment in RF phase has been defined as a clockwise rotation of the RF axis about the z-axis (in the same direction as Larmor precession).

2.12.3 The Approach to Steady State

Starting from equilibrium, the balanced SSFP signal goes through a transient phase, characterized by signal oscillations, before achieving steady state (fig. 2.16a-b). The duration of the transient phase depends on the flip angle, T_1 and T_2 relaxation times, as well as on the off-resonance frequency [31]. Due to relaxation processes, the signal acquired in MRI is decaying in time, which degrades image resolution. Signal oscillations are more problematic, however, because pixels in the image can be considerably displaced from their location in the object (fig. 2.17). This results in shifted, overlapping copies of the image, referred to as "ghosts".

Signal oscillations during the transient phase are primarily caused by differences in direction, rather than magnitude, between the instantaneous and steady state magnetization vectors [20]. "RF catalyzation strategy" is a general term used to refer to any sequence of preparatory RF pulses applied prior to balanced SSFP readout, designed to align the magnetization vector to the steady state direction, thereby reducing transient signal oscillations. The simplest catalyzation strategy consists of a single RF pulse with flip angle $\alpha/2$, applied at time $T_R/2$ prior to the first pulse in the balanced SSFP sequence (with flip angle α) [19] (fig. 2.18). This aligns the on-resonance ($\Delta\omega = 0$) magnetization vector with the steady state direction, eliminating signal oscillations (fig. 2.16c, $\Delta\omega = 0$). Catalyzing all frequencies is difficult, however, as the steady state magnetization direction varies with off-resonance frequency. While the $\alpha/2$ catalyzation works perfectly in the pass-band centre, signal oscillations remain off-resonance (e.g., Fig. 2.16c, $-.25/T_R < \Delta\omega < -.5/T_R$). Improved off-resonance performance can be obtained using a linear-ramp catalyzation [21] (Fig. 2.18 and Fig. 2.16d). More sophisticated catalyzation strategies also exist [20, 32], including those involving magnetization scaling as well as directing [20].

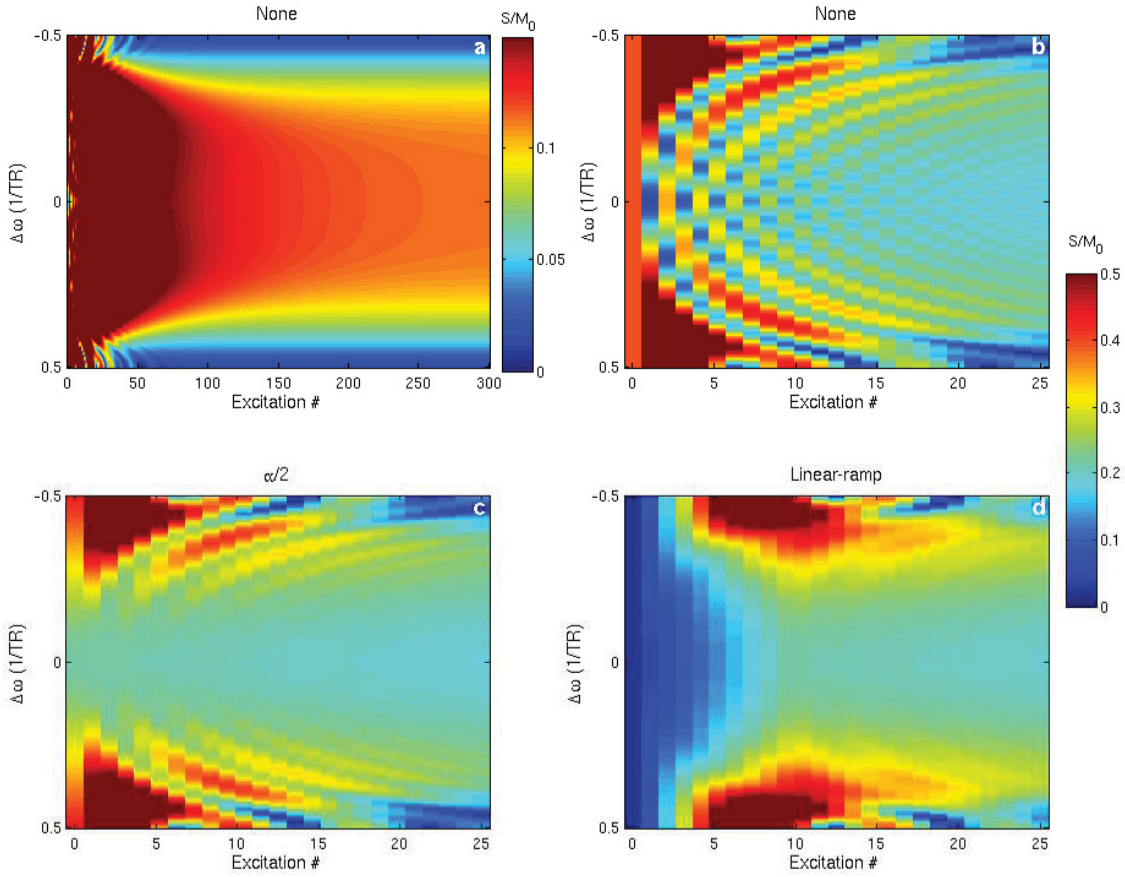

Figure 2.16: Balanced SSFP (180°-RF-phase-cycled) signal magnitude (S/M_0, amplitude indicated by colorbar) vs. excitation number (x-axis, equivalently RF pulse #) and off-resonance frequency $\Delta\omega$ (y-axis, in units of $1/T_R$), beginning from equilibrium ($\vec{M} = M_0\hat{z}$). The approach to steady state, over the course of 300 RF pulses, is shown using no RF catalyzation (a). Also shown is the signal behaviour over the course of the first 25 RF pulses for: (b) no RF catalzation (zoomed view of (a)), (c) $\alpha/2$ RF catalyation, and (d) linear-ramp RF catalyzation (10-pulse ramp). Plot parameters: $T_R = 10$ ms, $T_E = T_R/2$, $\alpha = 25°$, $T_1 = 1400$ ms, $T_2 = 70$ ms. Note the color scale of (a) differs from that of b-d.

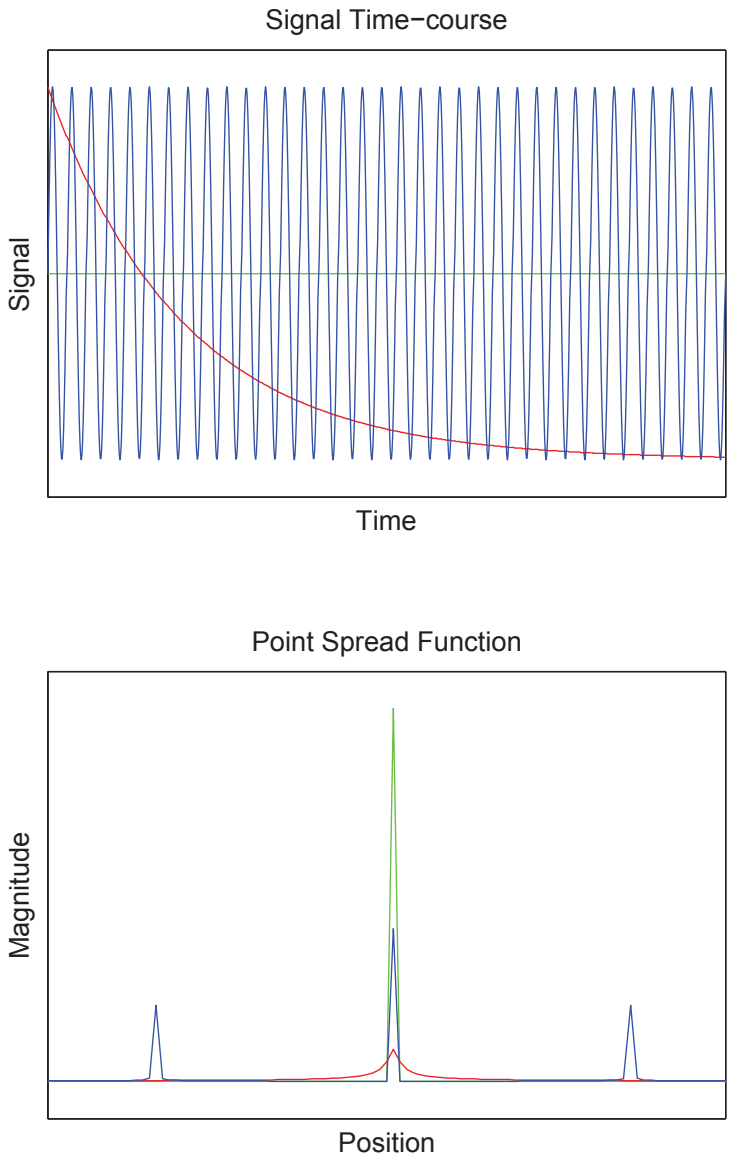

Figure 2.17: Top: constant (green), decaying (red), and oscillating (blue) signal timecourses. Bottom: magnitude of the Fourier transform of the corresponding signal-timecourse plotted above. This represents the point spread function - the (1D) image that would result if the object that produced the corresponding signal timecourse were a (1D) delta function.

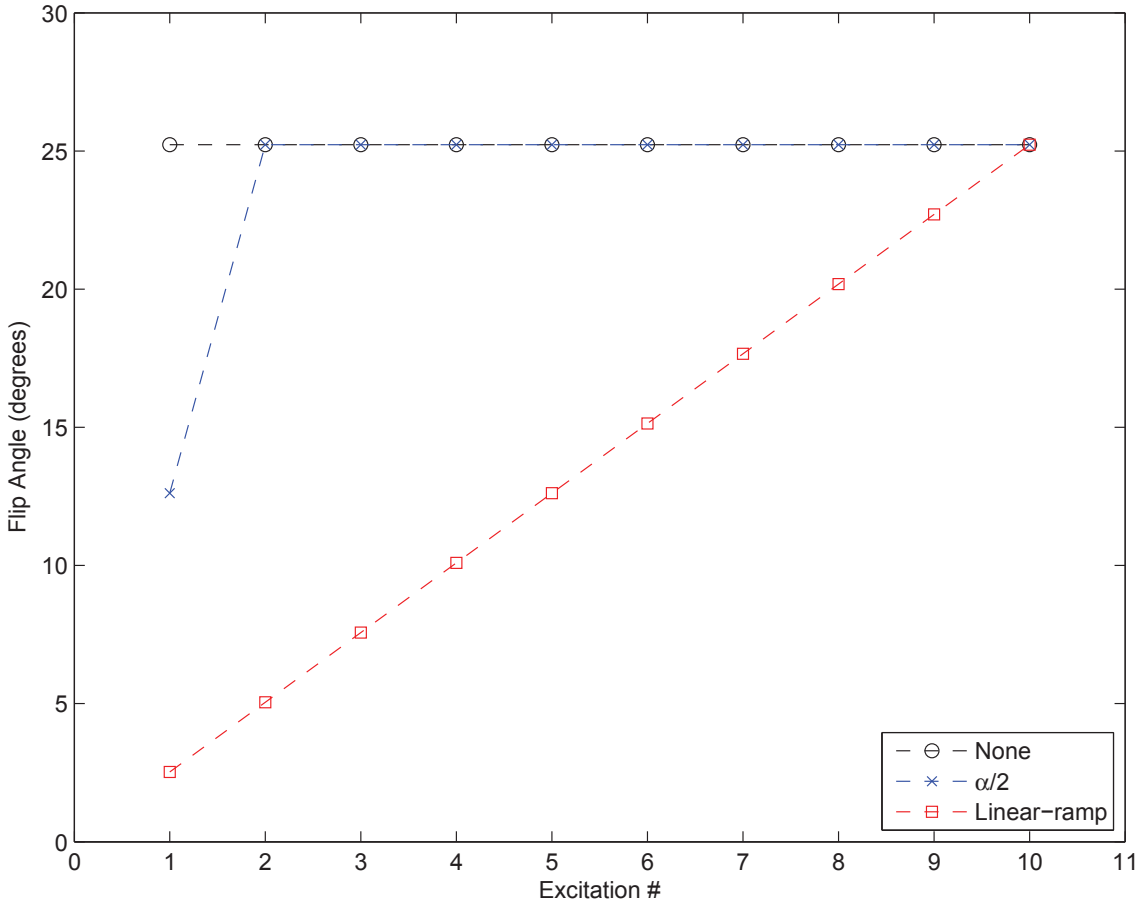

Figure 2.18: Flip angle of the first ten RF pulses for balanced SSFP using: no catalyzation (black circles), $\alpha/2$ catalyzation (blue x's) and linear-ramp RF catalyzation (red squares).

Chapter 3

Background: functional Magnetic Resonance Imaging (fMRI)

3.1 The BOLD Effect

This section follows the BOLD review article by Norris [15]. Fundamentally, BOLD fMRI measures changes in the local concentration of deoxyhemoglobin. Neural activity results in a local increase in blood oxygenation. The hemoglobin molecules inside of the red blood cells contain iron atoms (Fe^{2+}), which bind to oxygen (O_2) molecules, carrying them from the lungs to the cells of the body. These iron atoms contain unpaired electrons, resulting in a net magnetic moment. Oxygen molecules also contain unpaired electrons; when oxygen molecules bind to iron atoms, their respective unpaired electrons pair, resulting in no net magnetic moment. As a result, oxygenated blood, like brain tissue, is diamagnetic (weak negative magnetic susceptibility), whereas deoxygenated hemoglobin is paramagnetic (stronger, positive magnetic susceptibility). The increase in blood oxygenation that accompanies neural activity increases the homogeneity of the local magnetic field by reducing the local concentration of paramagnetic deoxyhemoglobin. This results in an increase in image intensity in T_2- (e.g., spin echo) or T_2^*-weighted (e.g., gradient echo) images, because of reduced dephasing.

Physiologically, the local concentration of deoxyhemoglobin in brain tissue depends on three parameters: 1) cerebral blood flow (CBF), 2) cerebral blood volume (CBV), and 3) the cerebral metabolic rate of oxygen ($CMRO_2$). Neural activity results in an increase in CBF, CBV, and $CMRO_2$. The increase in CBV results in an increase in the local concentration of deoxyhemoglobin (i.e., for a given tissue volume and blood oxygenation, an increase in tissue blood volume results in an increase in tissue deoxyhemoglobin concentration). Likewise, the increase in $CMRO_2$ results in an increase in the local concentration of deoxyhemoglobin, by extracting more oxygen

from the blood. Conversely, the increase in CBF results in a decrease in the local concentration of deoxyhemoglobin (i.e., by increasing the rate of delivery of oxygenated blood to the tissue, flushing out deoxyhemoglobin). Of these competing effects, the change in CBF dominates[1], such that an increase in neural activity is accompanied by a decrease in the local concentration of deoxyhemoglobin.

While an increase in neural activity resulting in an increase in blood oxygenation may seem paradoxical, this is resolved if one supposes that passive diffusion is the mechanism of oxygen delivery from the capillary bed to the cells [34]. Assuming a negligible partial pressure of oxygen at the cells, an increase in blood oxygenation at the capillary bed is the only way to increase the concentration gradient and therefore increase the rate of oxygen delivery to the cells, supporting increased energy demand.

3.2 BOLD Contrast Mechanisms

The distortions in the magnetic field created by paramagnetic deoxyhemoglobin extend beyond the blood vessels, resulting in both extra- and intravascular BOLD signal changes. These can be further subdivided into T_2 or T_2' effects, leading to four BOLD contrast mechanisms: 1) extravascular static dephasing (T_2'), 2) extravascular dynamic dephasing (T_2), 3) the intravascular T_2-like effect (T_2), and 4) the intravascular frequency offset effect (T_2').

In the resting state the blood oxygenation saturation fraction Y ($Y = 1$ for fully oxygenated blood and 0 for fully deoxygenated blood) is approximately 1 in the arteries and 0.6 at the end of the capillary beds and in the veins [35]. BOLD activation results in an increase in blood oxygenation ΔY of approximately 0.1 at the end of the capillary beds that experience increased blood flow. In the following discussion of BOLD contrast mechanisms, we consider "active" and "resting" states having blood oxygenation saturation fractions of $Y + \Delta Y$ and Y, respectively. Changes in blood volume between active and resting states are ignored, as are time-variations in blood oxygenation during the active state[2].

[1] typical CBF increases are on the order of 50-70 % while typical CBV and $CMRO_2$ increases are less than 20 % [33]

[2] this is a good approximation if the timescale of the image acquisition is much smaller than the timescale of the HRF, and for block designs (periods of continuous stimulation alternated with periods of rest, during which the hemodynamic response reaches a steady state).

Theoretical models of the BOLD signal change treat the blood vessels as cylinders having a length that is much greater than their diameter [35]. In the extravascular space, far from the granular RBCs, the cylinders can be considered to have a uniform magnetic susceptibility offset from the tissue in which they are embedded. This magnetic susceptibility offset is given by:

$$\Delta\chi_{\text{vessel}} = Hct(1-Y)\Delta\chi_{RBC} \tag{3.1}$$

where Hct, the hematocrit, is the volume fraction of red blood cells (RBC) in blood (approximately 0.4), Y is the blood oxygen saturation fraction, and $\Delta\chi_{RBC}$ is the magnetic susceptibility offset of a fully deoxygenated RBC from tissue (2.26×10^{-6} in SI units). The magnetic field offset, in the direction of the external magnetic field $\vec{B}_0$, produced outside of a cylinder having a magnetic susceptibility offset $\Delta\chi$ from its surroundings is given by:

$$\Delta B(r,\phi) = B_0(\Delta\chi/2)(R/r)^2 \sin^2\theta \cos 2\phi \tag{3.2}$$

where r and ϕ give position in polar coordinates in the plane perpendicular to the cylinder axis (see Fig. 3.1 for coordinate system definition, and note $r > R$), B_0 is the magnitude of the external magnetic field, R is the cylinder radius, and θ is the angle the cylinder axis makes with the external magnetic field $\vec{B}_0$. Figure 3.2 shows a plot of the magnetic field distortions surrounding a cylinder.

Note the spatial scale of the magnetic field distortions produced by a vessel are proportional to the vessel radius (R) (Eq. 3.2). This implies: 1) the spatial extent of the magnetic field distortions surrounding a large vessel is much greater than that surrounding a small vessel, and 2) the magnetic field distortions surrounding a small vessel vary more rapidly in space than those surrounding a large vessel.

Water protons surrounding a vessel have a distribution of larmor frequencies which causes a loss of phase coherence in time. The width of this distribution is proportional to the deoxygenation of the vessel via Eqs. 3.1 and 3.2. Thus the rate of phase coherence loss depends on the blood oxygenation.

BOLD contrast in the extravascular space can be divided into two contrast mechanisms:

1) Extravascular static dephasing: In the extravascular space surrounding large vessels ($R > 25$ μm), water protons are effectively static, on the T_E-timescale ($10 -$

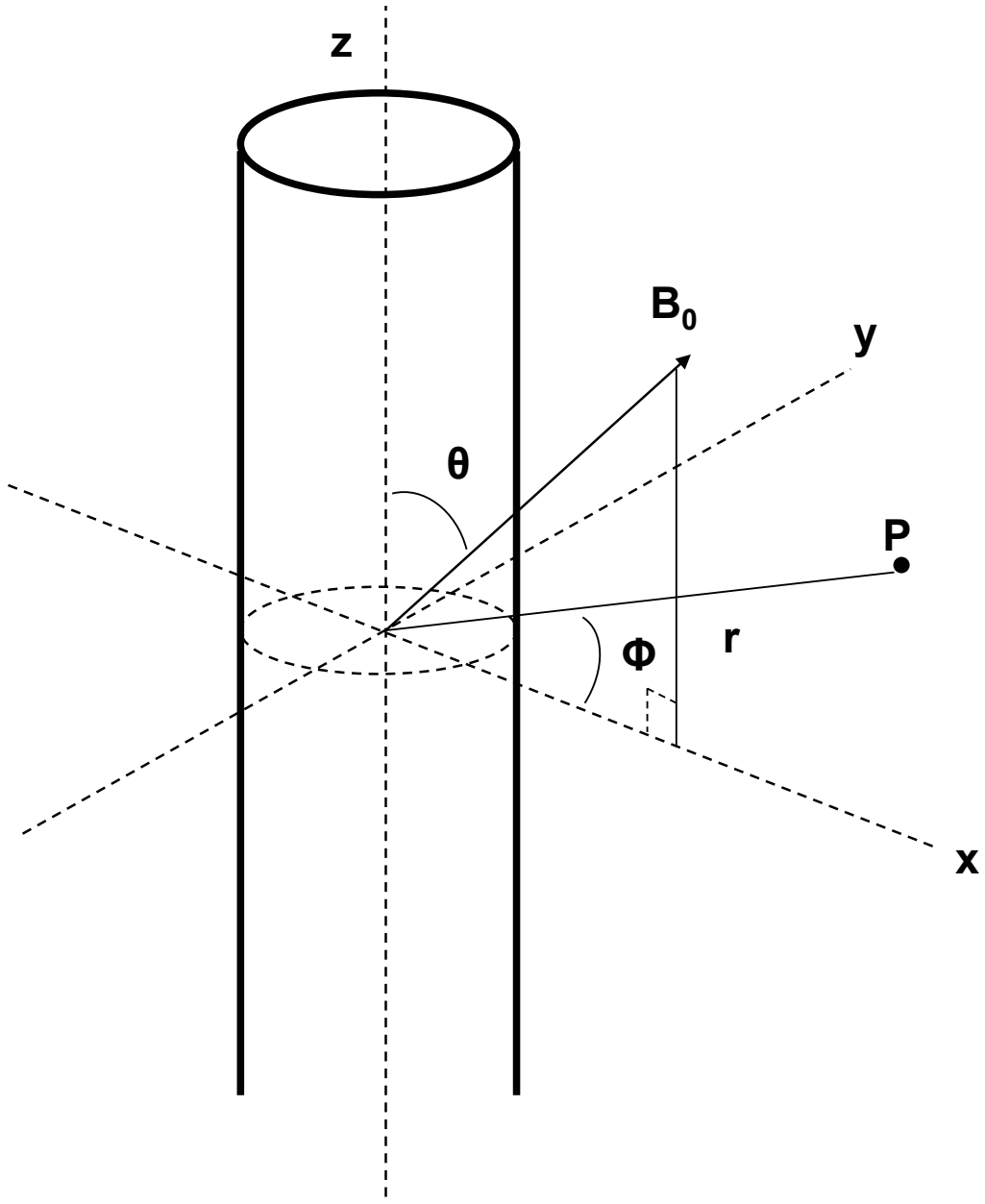

Figure 3.1: Local coordinate system used to compute the magnetic field offset at point P from a cylindrical field perturber. The x-axis is defined by the projection of $\vec{B}_0$ into the plane perpendicular to the cylinder axis containing P. r and ϕ give the position of P, in the plane perpendicular to the cylinder, in polar coordinates.

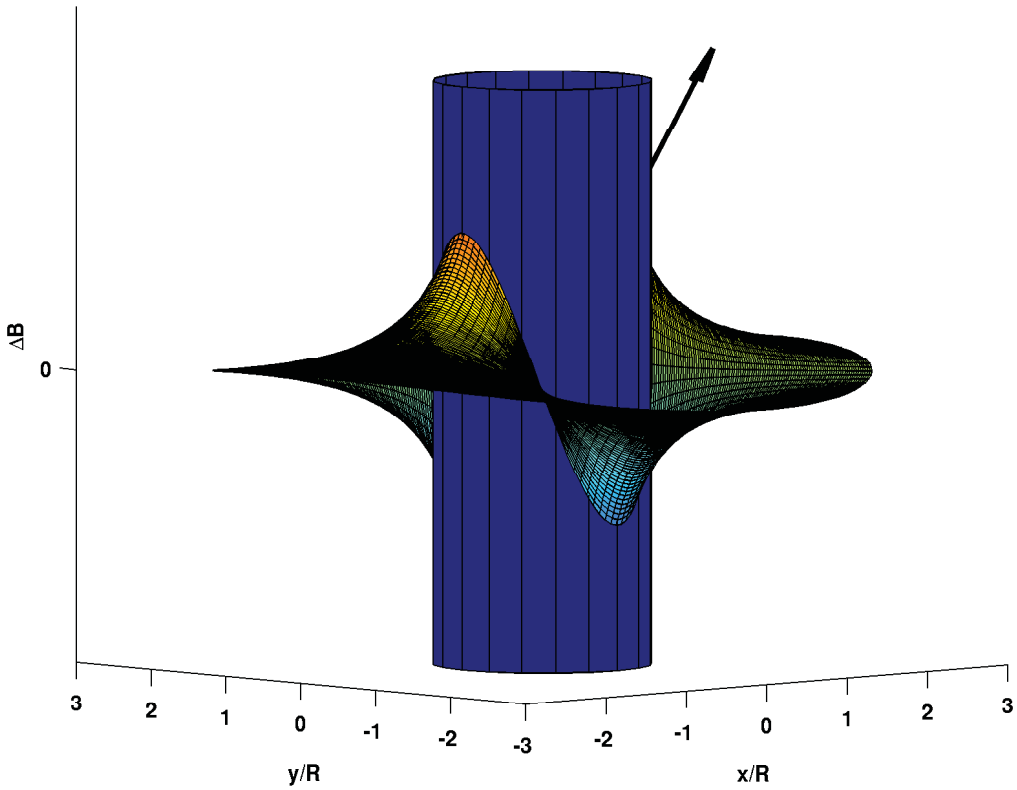

Figure 3.2: The magnitude of the magnetic field offset surrounding a cylinder represented as distortions in the plane perpendicular to the cylinder. Note the direction of these distortions is along the $\vec{B}_0$ axis, indicated by the black arrow.

100 ms), relative to the spatial scale of the magnetic field variations. The rate of signal loss caused by this static (time-independent) magnetic field variation can be characterized by a T_2' relaxation time (see section 2.7.3). BOLD activation reduces the strength of the perturbing magnetic field, increasing the T_2' relaxation time.

2) Extravascular dynamic dephasing: In the extravascular space surrounding small vessels ($R \leq 25$ μm), water protons diffuse a significant distance on the T_E-timescale relative to the spatial scale of the magnetic field variations. Each spin experiences a range of magnetic field offsets as it changes locations. This results in irrecoverable signal loss that can be characterized by a T_2 relaxation time (see sections 2.7.2 and 2.9.2). BOLD activation reduces the strength of the time-dependent magnetic field offsets experienced by each spin, increasing the T_2 relaxation time.

BOLD contrast in the intravascular space can also be divided into two contrast mechanisms:

1) Intravascular T_2-like effect: Water protons in the intravascular space diffuse rapidly around the RBCs and undergo chemical exchange across their highly permeable membranes. Again the spins experience a range of magnetic field offsets as they diffuse and exchange, resulting in irrecoverable signal loss that can be characterized by a T_2 relaxation time. BOLD activation reduces the strength of the magnetic field perturbations, increasing the T_2 relaxation time. The dependence of intravascular T_2 on blood oxygenation can be described by an analytic expression [36]:

$$R_2 = R_{2,0} + K(1 - Y)^2 \tag{3.3}$$

where $T_2 = 1/R_2$, $R_{2,0} = 3.9\ s^{-1}$ is a constant, Y is the blood oxygenation saturation fraction, and K is a constant that depends on field strength, pulse sequence, and echo time. For spin-echo sequences, K is given by [36]:

$$K = K_0 B_0^2 \left(1 - \frac{2\tau_{ex}}{\tau_{180}} \tanh \frac{\tau_{180}}{2\tau_{ex}}\right) \tag{3.4}$$

where $K_0 = 30.7\ s^{-1}$, B_0 is the strength of the external magnetic field in Tesla, $\tau_{ex} \approx 5\ ms$ is the mean resident time of water molecules in the RBC interior, and τ_{180} is the time-separation of the 180^0 pulses in a CPMG sequence, or T_E in a singe-echo spin-echo sequence.

2) Intravascular frequency-offset effect: The intravascular T_2-like effect is governed by the interaction between spins and neighboring RBCs. The interaction between

spins and distant RBCs in the blood vessel can be treated in a similar fashion to the extravascular case: far from the granular RBCs, the cylinder can be considered to have a uniform magnetic susceptibility. This results in a coherent frequency shift for all spins in the vessel that depends on the angle (θ) the blood vessel makes with the external magnetic field. Again modeling blood vessels as cylinders, the magnetic field offset, in the direction of the external magnetic field $\vec{B}_0$, produced inside of a cylinder having a magnetic susceptibility offset $\Delta\chi$ from its surroundings is given by:

$$\Delta B = B_0(\Delta\chi/2)(\cos^2\theta - 1/3) \tag{3.5}$$

See Fig. 3.1 for coordinate system definition. In the human brain, grey matter tissue contains vessels at various orientations. The distribution of vessel orientations results in a distribution of larmor frequencies for the intravascular spins. The intravascular frequency shift is time-independent and can therefore be characterized by a T_2' relaxation time. BOLD activation reduces the strength of the intravascular frequency shift, increasing the T_2' relaxation time.

3.3 The Temporal Resolution of BOLD

The duration of a single action potential is on the order of one millisecond, while the coherent firing of large groups of neurons occurs on the order of one hundred milliseconds (sensory processes) to one second (cognitive processes). Conversely, the hemodynamic changes that accompany neural activity occur on a considerably longer timescale - seconds to minutes. Figure 3.3 shows the timecourse of the BOLD response to an impulse stimulus at $t = 0$ - the hemodynamic response function (HRF). The positive BOLD response results from an increase in CBF which peaks approximately 5 s post-stimulus. This is followed by a post-stimulus undershoot that is believed to originate from a delayed return of the CBV to baseline, although some studies have suggested it to result from a prolonged elevation of $CMRO_2$. Note that a brief increase in neural activity (less than one second) results in a much longer hemodynamic response (up to one minute).

Defining a temporal resolution for BOLD is challenging. One way is to define the temporal resolution of BOLD as the shortest on-off period that can be detected in a block design paradigm. Or, what is the minimum time interval between two stimuli

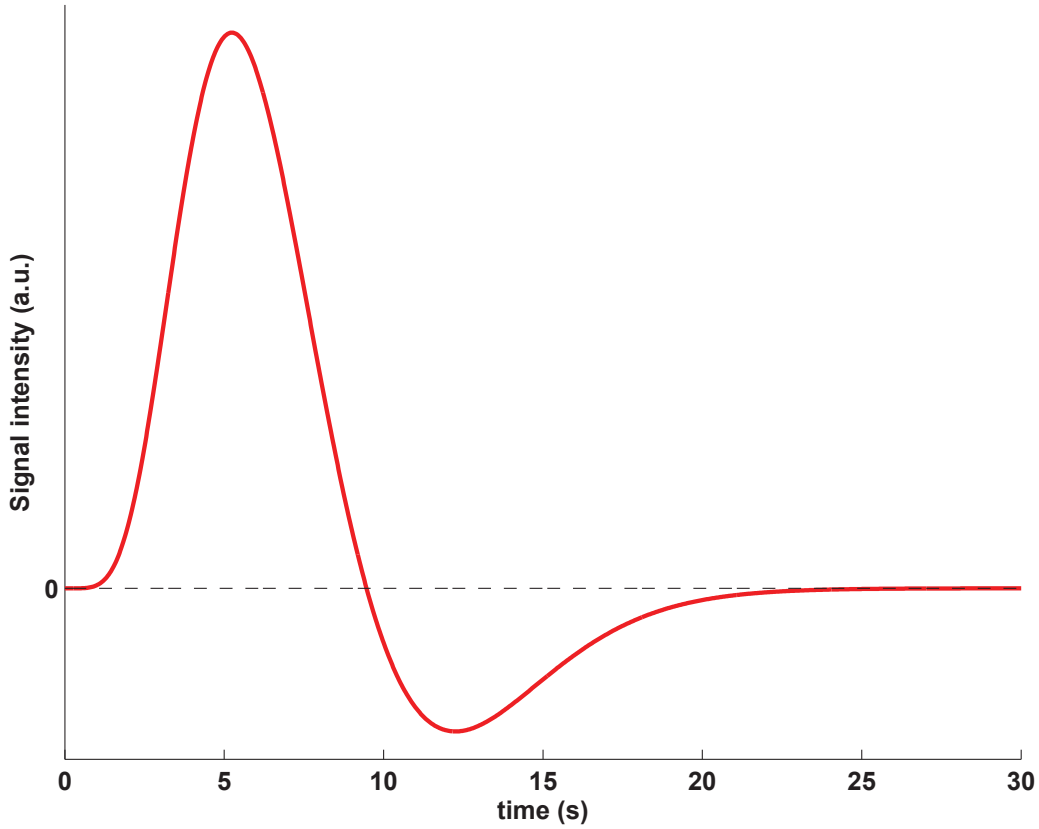

Figure 3.3: The canonical hemodynamic response function

required to for the stimuli to be resolved? When the on-off period becomes too short, the BOLD response becomes constant in time, preventing active and resting states from being distinguished. Using a finger-tapping task in the motor cortex, Friston et. al. found this time to be 8 s [37]. Later Bandettini et. al. found an on-off period of 4 s could be resolved with sufficient averaging across trials to increase SNR [38].

Another way is to define the temporal resolution of BOLD as the ability to pinpoint the onset of neural activity in a region of the brain. Studies have investigated the variation in the onset time of the HRF following an impulse stimulus. It was found that the HRF latency (from the impulse stimulus) for a single voxel varied between trials with a standard deviation of 1/2 s [39]. Assuming the onset of neural activity did not vary between trials, this places a limit on the ability to temporally resolve neural activity with fMRI. A further confound is the latency of the HRF across space. Studies using a finger tapping task in the motor cortex found the latency in the HRF to vary by 4 s between the active voxels in the motor cortex [35]. Some [40–42], but not all [43] studies have found HRF latency to correlate with vascular structure, with the shortest latencies occurring in gray matter and the largest occurring in large draining veins. As the variation in HRF latency within a brain region is typically larger than that between brain regions, it is challenging to use fMRI to map the spatial-temporal cascade of networked brain activation.

3.4 The Spatial Resolution of BOLD

Neural activity occurs over a range of spatial scales in the brain, from the firing of a single neuron (having a cell body on the order of 10 micron) to distributed neural networks spanning nearly the entire brain. Many factors influence the spatial resolution of neural activity that can be achieved using BOLD fMRI, including the spatial specificity of the HRF (i.e., the volume of increased blood oxygenation relative to the volume of increased neural activity), the pulse sequence used (e.g., GRE vs. SE), and the strength of the main magnetic field.

One fundamental limit to the spatial resolution achievable with BOLD fMRI is the spatial specificity of the HRF. The visual cortex of many mammals, including humans, is divided into groups of neurons that respond primarily to input from one eye named ocular dominance columns. As the name suggests, these groups of neurons are

organized into columns running perpendicular to the cortical surface, and are less than one millimeter across in humans. An optical spectroscopy study involving sensory stimulation of cortical columns in cats found an initial increase in deoxyhemoglobin that was localized to the cortical columns, followed by an increase in blood flow approximately 3 s later that spread over an area of 3-5 mm [44]. This lead the authors to describe the CBF response as "Watering the whole garden for the sake of one thirsty flower". Other optical spectroscopy studies have generally confirmed these results [45]. If the CBF response is uniform (not higher at the foci of neural activity and lower in distal regions), this suggests 3-5 mm as a fundamental limit to the resolution of neural activity attainable with fMRI.

Studies have also taken advantage of the retinotopic organization of the human visual cortex to assess the spatial resolution of the BOLD effect. The spatial frequency of the activation pattern induced in the primary visual cortex is proportional to the spatial frequency of the stimulus applied to the visual field. Applying visual stimuli at higher and higher spatial frequency will induce patterns of neural activity at higher and higher spatial frequency in the visual cortex. However, because the HRF blurs the region of increased neural activity, visual stimuli applied beyond a threshold spatial frequency will produce a homogenous activation pattern, as the HRF blurs neighboring regions of active cortex together. In this fashion Engel et. al. [46] found the spatial resolution of BOLD fMRI to be 3.5 ± 1.5 mm at 1.5 T. The results of similar studies measuring the point spread function of BOLD fMRI in the visual cortex at several magnetic field strengths are given in table 3.1. The data in this table has been taken from *Principles of Magnetic Resonance Assessment of Brain Function* by Norris [15]. An estimate for the PSF of spin-echo fMRI at 1.5 T has not been given, likely due to inadequate sensitivity at this field strength [15]. The two PSF estimates for GRE BOLD at 7 T correspond to voxels that did not (lower estimate) and did (higher estimate) contain large vessels[3].

In spite of these findings, the positive BOLD response has been used to map ocular dominance columns in the human visual cortex at 4 T [47]. This study found single-eye stimulation to elicit a positive BOLD response in both left-eye and right-eye

[3]the presence of large vessels was inferred from the magnitude of the BOLD response; a threshold was chosen to divide active voxels into those containing large vessels (supra threshold) and those not containing large vessels (subthreshold)

	1.5 T	3 T	7 T	9.4 T
Gradient echo	3.5 ± 1.5	3.9 ± 0.7	3.5; 2	1.6
Spin echo	no data available	3.4 ± 0.8	< 2	1

Table 3.1: Width measurements (mm) of the BOLD fMRI Point Spread Function. Adapted from *Principles of Magnetic Resonance Assessment of Brain Function* by Norris [15].

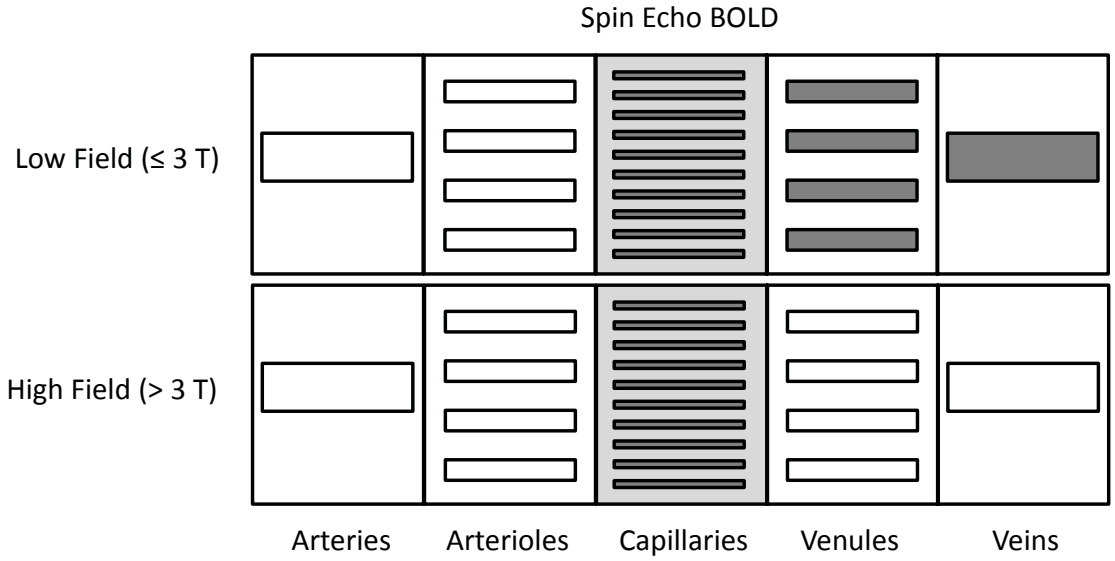

Figure 3.4: The tissue and vascular compartments that contribute to the SE BOLD signal at low and high field are shaded in grey. Light and dark shades of grey are only used to distinguish between compartments and do not indicate relative weighting between compartments. Adapted from *Functional MRI: an introduction to methods* [33].

ocular dominance columns, but the BOLD response was stronger in the columns corresponding to the eye being stimulated. This study also found the spatial specificity of the positive BOLD response to diminish as stimulus duration was increased.

The spatial resolution of BOLD also depends on the choice of pulse sequence. The tissue and vascular compartments that contribute to BOLD contrast for SE and GRE pulse sequences are shown in Figs. 3.4 and 3.5, respectively. These figures are adapted versions of those found in *Functional MRI: an introduction to methods* [33]. Blood flow carries changes in blood oxygenation from the foci of neural activity (i.e., the capillary bed) downstream into venules and finally to large draining veins. This reduces the specificity of changes in blood oxygenation to the foci of neural activity. However, this effect is also mitigated by the dilution of blood oxygenation changes in

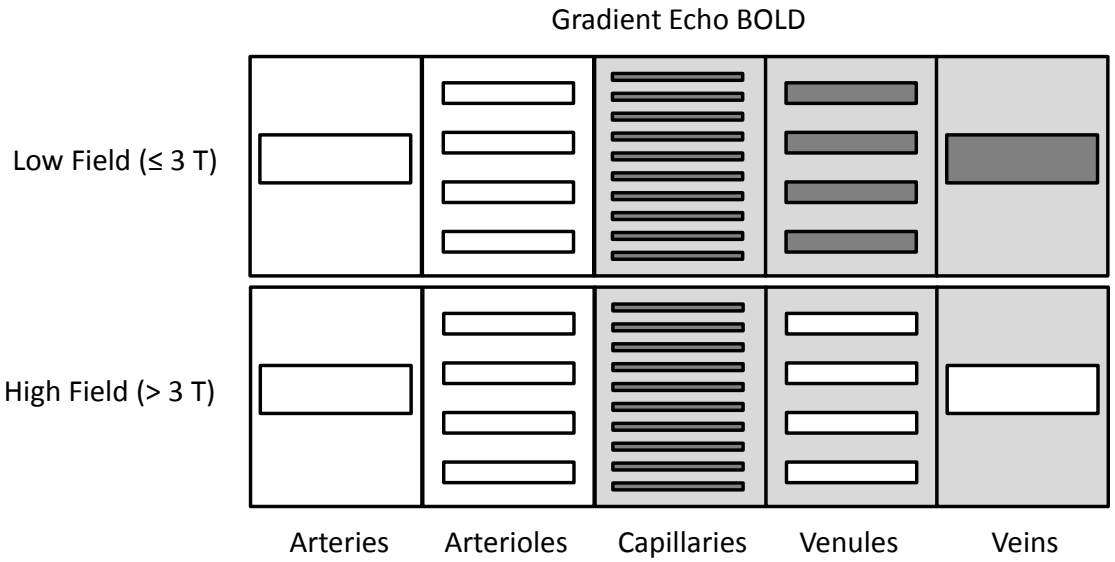

Figure 3.5: The tissue and vascular compartments that contribute to the GRE BOLD signal at low and high field are shaded in grey. Light and dark shades of grey are only used to distinguish between compartments and do not indicate relative weighting between compartments. Adapted from *Functional MRI: an introduction to methods* [33].

large veins due to inflow from inactive regions. The contrast mechanisms described above (see 3.2) vary in terms of their coupling to the foci of neural activity. Extravascular dynamic dephasing is specific to capillary-sized vessels and therefore tightly coupled to the foci of neural activity. Intravascular effects occur in vessels of all sizes, while extravascular static dephasing is strongest surrounding large vessels, furthest from the site of neural activity. The relative contribution to total BOLD contrast from each contrast mechanism depends on the pulse sequence used. GRE sequences derive contrast from all all four BOLD contrast mechanisms described above. SE sequences refocus T_2' effects and are only sensitive to extravascular dynamic dephasing and the intravascular T_2-like effect. Of note, SE sequences refocus extravascular static dephasing effects surrounding large vessels, which is the least spatially specific of the four BOLD contrast mechanisms. This suggests that SE BOLD fMRI maps will be better localized to the site of neural activity than GRE. However, at 1.5 T, the intravascular T_2-like effect is the dominant contrast mechanism for both GRE and SE pulse sequences [48]. This explains the similar BOLD PSFs obtained for SE and GRE fMRI shown in table 3.1.

Magnetic field strength also influences the spatial resolution achievable with BOLD fMRI. As field strength is increased, the intravascular T_2 relaxation time becomes increasingly shorter than the T_2 relaxation time of grey matter. At high ($> 3\ T$) field, extravascular dynamic dephasing becomes the dominant contrast mechanism for SE sequences, while extravascular static dephasing becomes the dominant contrast mechanism for GRE sequences [36]. As a result, SE BOLD becomes increasingly specific to the foci of neural activity at high field.

Experimental results also indicate a reduction in the spatial PSF for GRE fMRI at high field (Table 3.1). This may be due to the enhanced relative sensitivity to microvasculature for GRE fMRI at high field predicted by Monte Carlo simulations [24, 49]. Diffusion effects reduce BOLD contrast in GRE fMRI. As magnetic field strength is increased, the radius of the blood vessel for which diffusion effects become negligible decreases. However, note that the relative sensitivity of microvasculature to macrovasculature cannot exceed one for GRE fMRI; in the static dephasing limit (no diffusion), GRE BOLD contrast is independent of vessel size for fixed blood volume [50].

3.5 The Optimum T_E for GRE and SE fMRI

Experimental studies have found that the BOLD effect can be well-described by a change in the R_2^* (ΔR_2^*) or R_2 (ΔR_2) relaxation rates for GRE and SE sequences, respectively. BOLD contrast ΔS can then be represented as the difference in signal levels (S) between active and resting states. Note that ΔR_2, $\Delta R_2^* < 0$ (i.e., the relaxation rate decreases upon activation).

$$\begin{aligned} \Delta S &= S_{\text{active}} - S_{\text{resting}} \\ &= \exp\left(-(R_2 + \Delta R_2)T_E\right) - \exp\left(-R_2 T_E\right) \end{aligned} \tag{3.6}$$

Fractional BOLD signal change is given by:

$$\begin{aligned} \frac{\Delta S}{S_{\text{resting}}} &= \exp\left(-\Delta R_2 T_E\right) - 1 \\ &\approx -\Delta R_2 T_E, \text{ for } |\Delta R_2 T_E| << 1. \end{aligned} \tag{3.7}$$

While the fractional BOLD signal change increases linearly with T_E, the baseline signal decreases exponentially. Thus there is an optimum T_E for BOLD:

$$\begin{aligned} T_E &= \frac{\ln(\frac{R_2+\Delta R_2}{R_2})}{\Delta R_2} \\ &\approx \frac{1}{R_2}, \text{ for } |\Delta R_2| << R_2 \\ &= T_2. \end{aligned} \tag{3.8}$$

At the optimum T_E, BOLD contrast is directly proportional to the normalized R_2 change:

$$\Delta S \propto \frac{\Delta R_2}{R2}. \tag{3.9}$$

For GRE, replace R_2 with R_2^* and T_2 with T_2^* in eqs. (3.6) to (3.9). Equation 3.9 governs the choice between GRE and SE pulse sequences for fMRI. If $\Delta R_2/R2 > \Delta R_2^*/R_2^*$, spin-echo will be more sensitive, whereas if $\Delta R_2/R2 < \Delta R_2^*/R_2^*$, gradient echo will be more sensitive.

3.6 Overview of fMRI Analysis

This section outlines the steps involved in an elementary model-based[4], univariate[5] fMRI analysis following Chapter 11, "Overview of fMRI analysis" in "Functional MRI: an introduction to methods" [33].

In a typical fMRI experiment, the subject performs a task or attends a stimulation, interspersed with periods of rest, for a total duration of about five minutes. Images are acquired every 2-3 s during this time, matching the timescale of variations in blood oxygenation, which normally restricts the images to low spatial resolution (on the order of $5\times5\times5$ mm^3). These rapid, low spatial resolution images are referred to as functional images. The goal is then to determine which brain areas were involved in the performance of the task or activated by the stimulation. The simplest stimulation paradigm is the block design - periods of stimulation (often 20-30 s) alternated with equally-long periods of rest, applied in a square wave pattern.

Following data collection, the following pre-processing and statistical analyses are usually performed to determine active brain regions:

[4] i.e., the data is compared with a model of the expected response

[5] i.e., the timeseries of each image voxel is analyzed independently

1. Motion correction: the timecourse of functional images are re-aligned. This helps reduce false activations, particularly at the boundaries between high and low signal regions.

2. Spatial smoothing: each individual image volume is convolved with a gaussian function, typically having a full-width-at-half-maximum (FWHM) of 1.5 times the nominal image voxel size. This increases SNR at the expense of spatial resolution.

3. High-pass filtering: each voxel timeseries is high-pass filtered at a cutoff frequency slightly lower than the stimulation frequency. This removes drifts in baseline signal intensity than can arise, for example, from heating of the gradient coil, reducing the quality of the magnetic field shim over time.

4. General Linear Modeling (GLM): after pre-processing steps 1-3, the timeseries for each voxel is least-squares fit to a model of the expected response. The model is obtained by convolving the stimulus function (for a block design, a square wave) with the hemodynamic response function (see Fig. 3.3 and section 3.3). This represents the expected BOLD response of the brain to the stimulus. Voxels are then classified as active or inactive depending on the goodness of fit.

To reduce the number of false positives, a correction for multiple comparisons (based on the number of voxels in the functional image) is used in assigning the statistical threshold defining activation. Cluster thresholding is a common way to do this, in which the number of contiguous active voxels is taken into account when determining statistical significance, as truly active voxels are expected to occur in spatially contiguous clusters rather than in isolation. Often a single, high-resolution anatomic image is collected during the fMRI session, and activation maps are overlaid on this image to better-visualize the anatomic origin of the observed activation.

3.7 Balanced SSFP fMRI

Balanced SSFP fMRI techniques are typically classified as transition-band or pass-band approaches, depending on which portion of the balanced SSFP signal vs. off-resonance profile is used to generate functional contrast. The first balanced SSFP

fMRI technique was proposed by Scheffler [51], which we will refer to as magnitude-sensitive transition-band SSFP fMRI. This technique involves adjusting the centre-frequency such that activation-induced frequency shifts span the steep portion of the b-SSFP signal magnitude profile (Fig. 3.6a). Activation-induced frequency shifts then create large changes in signal magnitude.

An improved transition-band SSFP fMRI technique was proposed by Miller [52], which we will refer to as phase-sensitive transition-band SSFP fMRI[6]. In this technique the steep portion of the b-SSFP signal phase, rather than the magnitude, profile is exploited (Fig. 3.6b). A low flip angle is used to maximize the signal magnitude in this region. Because the phase of the b-SSFP signal changes by close to π over a narrow frequency range, the potential contrast using this method is twice that possible from the magnitude approach[7].

A third b-SSFP fMRI technique, pass-band SSFP, was proposed by Bowen [17]. In pass-band SSFP the centre frequency and flip angle are chosen to minimize the frequency sensitivity of the signal magnitude and phase over the region of interest (Fig. 3.6c). Pass-band SSFP is primarily sensitive to activation-induced changes in T_2 rather than frequency shifts.

Advantages

The major advantage for balanced SSFP over SE and GRE fMRI techniques is the ability to achieve BOLD contrast at extremely short T_E [7,17]. This allows for highly segmented **k**-space acquisitions to be used in balanced SSFP fMRI, permitting high-resolution, distortion-free imaging, without a penalization in efficiency [18]. GRE and SE fMRI acquisitions becomes increasingly inefficient with increased segmentation because a delay on the order of T_2^* (or T_2) must be inserted at the beginning of each segment for sufficient BOLD contrast to develop prior to data encoding. Instead, GRE and SE fMRI acquisitions use long, single-shot readouts for efficiency. Long readouts allow more time for both T_2^* (or T_2) decay, reducing image resolution, and phase accrual due to unwanted sources of magnetic field variation, increasing image distortion.

[6] also known as blood oxygenation sensitive steady-state (BOSS) fMRI

[7] i.e., for signal level S, $\Delta S_{\max} \approx S - 0 = S$ for the magnitude-sensitive approach and $\Delta S_{\max} \approx S - (-S) = 2S$ for the phase-sensitive approach.

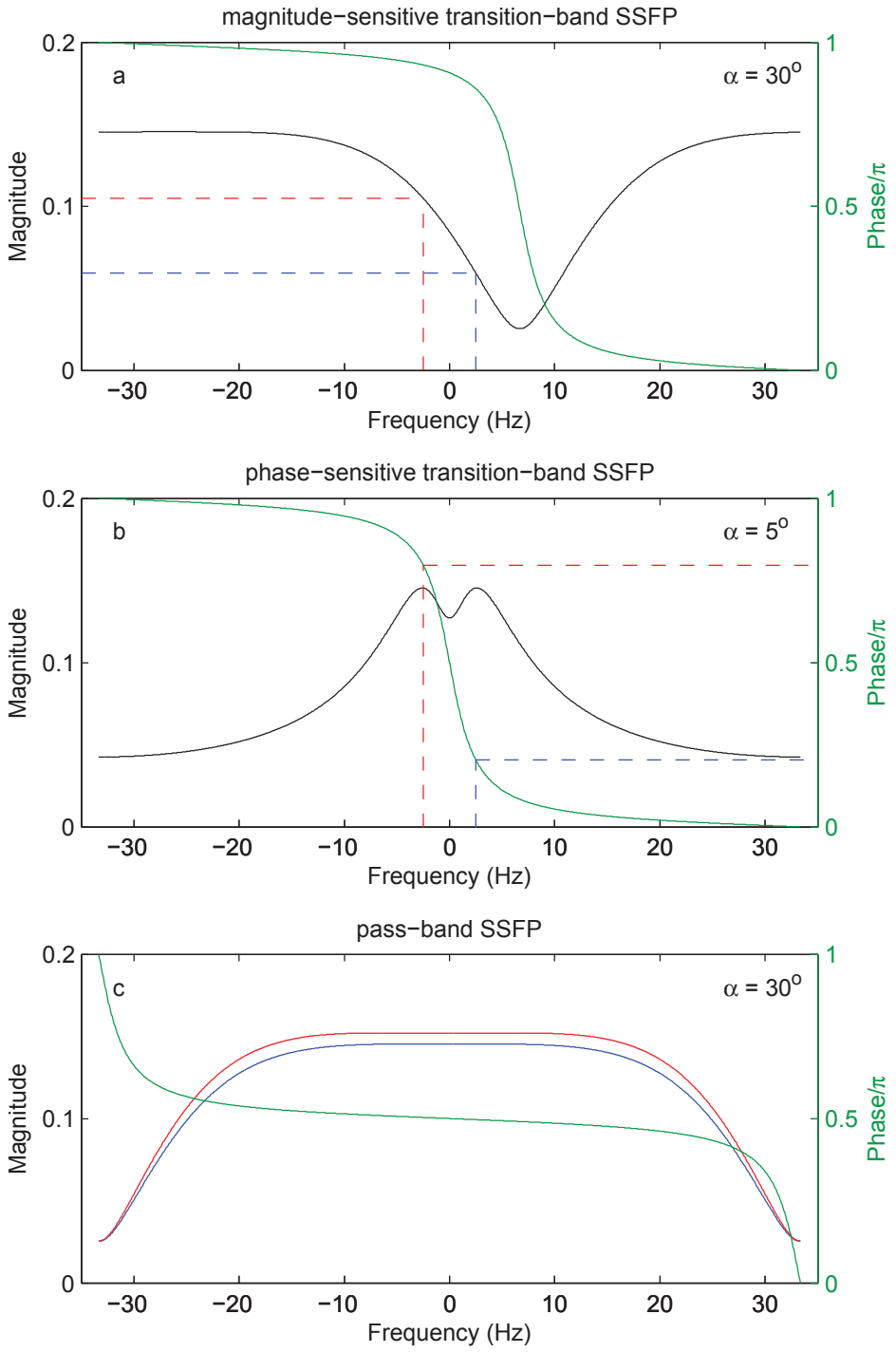

Figure 3.6: Balanced SSFP fMRI techniques. In (a) and (b) activation is depicted as a 5 Hz frequency shift between resting (blue dashed line) and active (red dashed line) states. In (c) activation is depicted as a decrease in R_2 of 1 s^{-1} between resting (blue line) and active (red line) states.

Drawbacks

The major drawback of balanced SSFP fMRI is limited spectral coverage, which results in the need for multiple acquisitions to achieve whole brain coverage. This is compounded by the fact that the multiple acquisitions are derived from different steady states, which take longer to establish than the time required to acquire an image, once in them.

In a study demonstrating whole-brain fMRI using phase-sensitive transition-band SSFP, acquisition at 11 centre frequencies was required to ensure functional sensitivity in each brain region [53]. Pass-band SSFP has reduced BOLD sensitivity compared to transition-band SSFP (both magnitude- and phase-sensitive), but covers a much broader spectral range; whole-brain coverage has been demonstrated by combining acquisitions at two centre frequencies (referred to as the two-acquisition method) [4].

Small-tip fast recovery (STFR) is a recently proposed (2012) pulse sequence that produces image contrast similar to balanced SSFP, but has the potential to eliminate banding artifacts in a single scan [54,55]. STFR uses short excitation pulse repetition times (around 10 ms), similar to balanced SSFP, with the addition of a tailored tip-up pulse having a spatially-varying phase to align spins with the longitudinal axis after each data readout segment, regardless of off-resonance frequency. However, STFR is limited by reduced spatial (rather than spectral) coverage (i.e., incapable of whole-brain fMRI), as tip-up pulses having a spatially-varying phase over a large region of space are incompatible with short pulse repetition rates.

Alternating SSFP

As mentioned above and in chapter 1, balanced SSFP is capable of whole-brain fMRI by combining acquisitions at multiple centre frequencies (RF phase cycling increments) to eliminate banding artifacts. However, it takes several seconds to establish steady state at a new centre frequency (see Fig. 1.5 on page 9), resulting in a prohibitively long banding-artifact-free image acquisition time (i.e., on the order of 10 s, whereas images must be acquired roughly every 3 s to track blood oxygenation changes in the brain (see Fig. 3.3 for a plot of the hemodynamic response function)).

The goal of this work was to develop an accelerated balanced SSFP fMRI technique, alternating SSFP, to achieve rapid, banding-artifact-free balanced SSFP fMRI.

We hypothesize that RF catalyzation strategies will allow imaging during the transient phase of balanced SSFP, reducing the dead-time between the acquisition of images from different steady states. We chose to focus acceleration attempts on pass-band SSFP rather than transition-band SSFP. While pass-band SSFP is less sensitive to BOLD signal changes than transition-band techniques, pass-band SSFP covers a broader spectral range than transition-band SSFP, requiring acquisition at fewer centre frequencies to achieve whole-brain coverage.

Chapter 4

Theoretical Modeling

4.1 Introduction

As outlined in the introductory chapter, two-acquisition pass-band SSFP fMRI is capable of whole-brain, banding-artifact-free fMRI, but not at the 3 s (roughly) temporal resolution necessary for most applications in neuroscientific and clinical settings[1]. The goal of this project was to develop an accelerated two-acquisition pass-band SSFP fMRI technique, alternating SSFP. The alternating SSFP acquisition parameter space is too broad to probe experimentally, so theory and simulation were used to identify appropriate acquisition parameters, with comparison to established balanced SSFP acquisitions. This chapter describes the development of alternating SSFP using theoretical modeling.

The primary challenges associated with alternating SSFP are reducing signal oscillations and maintaining BOLD sensitivity during the transition between (quasi) steady states. Bloch simulations were used to identify a smooth signal transition between steady states by comparing acquisitions employing flip-back [56] and novel flip-down RF pulses, gradient spoiling, and RF catalyzation strategies [19, 21]. After identifying a suitable alternating SSFP implementation using Bloch simulations, Monte Carlo simulations were used to optimize the remaining free parameters (flip angle, image combination strategy, **k**-space ordering) for BOLD sensitivity, with quantitative comparison to conventional pass-band SSFP[2].

[1] two-acquisition pass-band SSFP fMRI has a temporal resolution on the order of 10 s (or several minutes, in the case of a repeat run of the functional paradigm).

[2] comparisons were not made with transition-band SSFP; although more sensitive to BOLD changes than pass-band SSFP, transition-band SSFP requires about 10 acquisitions to achieve whole-brain coverage (whereas pass-band SSFP requires 2) and was therefore not considered a practical technique for whole-brain fMRI.

4.2 Methods

4.2.1 Monte Carlo Simulations

Overview

Monte Carlo simulations at 4 T of spin isochromat diffusion throughout a blood vessel network were performed following Boxerman [24]. An overview of the simulation procedure is given below.

Tissue voxels were modeled as cubes (side-length $L = 100 + 80R$ μm) containing randomly oriented cylinders, representing blood vessels (radius R, infinite length, occupying voxel volume fraction f), embedded in a homogeneous medium with grey matter relaxation properties. Two tissue models were considered in this work: a microvasculature model ($f = 2$ %$, R = 3$ μm) and a simplified grey matter model ($f = 2$ %$, R = 3$ μm combined with $f = 3$ %$, R = 100$ μm). Monte Carlo simulations using these blood volume and vessel radii values have shown good agreement with experiment (e.g., [23]). Vessels were assigned a magnetic susceptibility offset, relative to their surroundings, of $Hct\Delta\chi(1 - Y)$, where $Hct = 0.4$ is the Hematocrit, $\Delta\chi = 2.26 \times 10^{-6}$ (SI units) is the susceptibility offset across a fully deoxygenated red blood cell, and Y is the blood oxygen saturation fraction. This magnetic susceptibility offset produced a spatially varying magnetic field throughout the voxel according to eq. (3.2). BOLD activation was simulated by changing Y from 0.67 (resting) to 0.75 (active). Y values were obtained from a previous study that found good agreement between SSFP simulations and experiment [22].

A 100 μm side-length diffusion cube was centered in the tissue voxel having side-length $L = 100+80R$ μm. Simulations began with the placement of a spin isochromat at a random location within the diffusion cube. The spin isochromat commenced a random walk in three dimensions (Gaussian distributed step size, zero mean, standard deviation $\sigma = \sqrt{2D\Delta t}$ in each dimension), with a time step, $\Delta t = 100$ μs, and diffusion coefficient, $D = 1$ μm^2/ms, the approximate value in grey matter [24]. Blood vessels were modeled as impermeable, which is a closer approximation to physiological permeability than freely permeable vessels [24,57]. Spins were confined to the diffusion cube centred in the larger tissue voxel to prevent the near-approach of spins to the vascular tissue voxel perimeter, and apparent blood volume reduction. Diffusion

steps violating these boundary conditions were retaken until boundary conditions were satisfied. Simulations using a smaller (60 μm) diffusion cube were verified to agree with simulations using the 100 μm diffusion cube to ensure results were not biased by finite-size effects (results not shown).

Each time step, the spin isochromat underwent precession from the net magnetic field, calculated by summing the contribution from each vessel in the tissue voxel [24], and T_1 and T_2 relaxation, the latter of which varied between the intra and extravascular space (see section 4.2.1, Relaxation Rates, below). RF pulses, implemented as 3×3 rotation matrices instantaneously in time [22], were applied to the spin isochromat with flip angle, phase, and timing specific to the pulse sequence being simulated (see section 4.2.3, Pulse Sequences, below).

The normalized signal, S/M_0, was calculated as the magnitude of the vector sum of the transverse magnetization from 1,000 isochromat trials, divided by the number of trials, with M_0 set to 1. Vessel positions were redistributed for each trial. Sets of 1,000 isochromat trials were simulated and averaged until the percent change in the measured value of interest from including additional sets was less than one percent for several additional sets in a row. This required 10-50 sets, depending on the effect size. Simulations were conducted for both active and resting states, and fMRI contrast was calculated as the difference in the normalized signal between the active and resting simulations ($\Delta S/M_0$). In this work, BOLD contrast ($\Delta S/M_0$) is preferred to the more often reported percent signal change ($\Delta S/S$). For a constant baseline signal, BOLD contrast and percent signal change are proportional. However, in balanced SSFP the baseline signal varies strongly with off-resonance frequency. In this case, BOLD contrast, rather than percent signal change, better corresponds to experimental BOLD sensitivity.

Relaxation Rates

The rapid nature of the diffusion and exchange processes that govern the intravascular transverse relaxation rate permit an analytical characterization (eq. 3 in [36] at

$B_0 = 4\ T, \tau_{ex} = 4.4\ ms$ [58])[3]:

$$R_2 = R_{2,0} + A(1-Y)^2\left(1 - \frac{2\tau_{ex}}{\tau}\tanh\frac{\tau}{2\tau_{ex}}\right), \tag{4.1}$$

where $R_{2,0} = 3.9\ \mathrm{s}^{-1}$, $A = 490.4\ \mathrm{s}^{-1}$, Y is the blood oxygenation saturation fraction, τ_{ex} is the mean resident time of water molecules in red blood cells, and τ is the spacing between refocusing RF pulses. In computing intravascular R_2, τ was taken to be T_R in pass-band SSFP [58]. Extra-vascular T_2 was fixed at 70 ms [59], with diffusion-attenuation added explicitly via Monte Carlo modeling. T_1 was calculated to be 1383 ms at 4 T from a phenomenological equation for grey matter [60], and differences between intra- and extra-vascular T_1, which are small [61], were ignored.

4.2.2 RF catalyzation

RF catalyzation strategies (see section 2.12.3) consist of a sequence of preparatory RF pulses applied prior to balanced SSFP readout that are designed to expedite imaging. These typically fall into two categories: those that rapidly achieve the steady state magnetization [20], and those that reduce signal oscillations during the transition into steady state [19, 21, 32]. Of these, the latter are simpler and more robust in the presence of B_1 inhomogeneity. In this work, $\alpha/2$ [19] and linear-ramp [21] RF catalyzation strategies were investigated for reducing signal oscillations in alternating SSFP. Each consisted of 10 RF pulses with the same pulse spacing and RF phase cycling as the subsequent balanced SSFP RF train readout. Linear ramp RF catalyzation consisted of linearly increasing the RF flip angle from $\alpha/10$ to α over the first 10 pulses. $\alpha/2$ RF catalyzation consisted of a half-tip RF pulse followed by 9 α pulses (to match catalyzation time with linear ramp).

4.2.3 Pulse Sequences

Alternating SSFP

Alternating SSFP simulations consisted of a timecourse of balanced-SSFP ($T_R/T_E/\alpha$ = 10 ms/5 ms/30-60°) image volumes acquired with, alternately, 180° or 0° RF phase-cycling increments.

[3] the following equation is simply eqs. 3.3 and 3.4 combined.

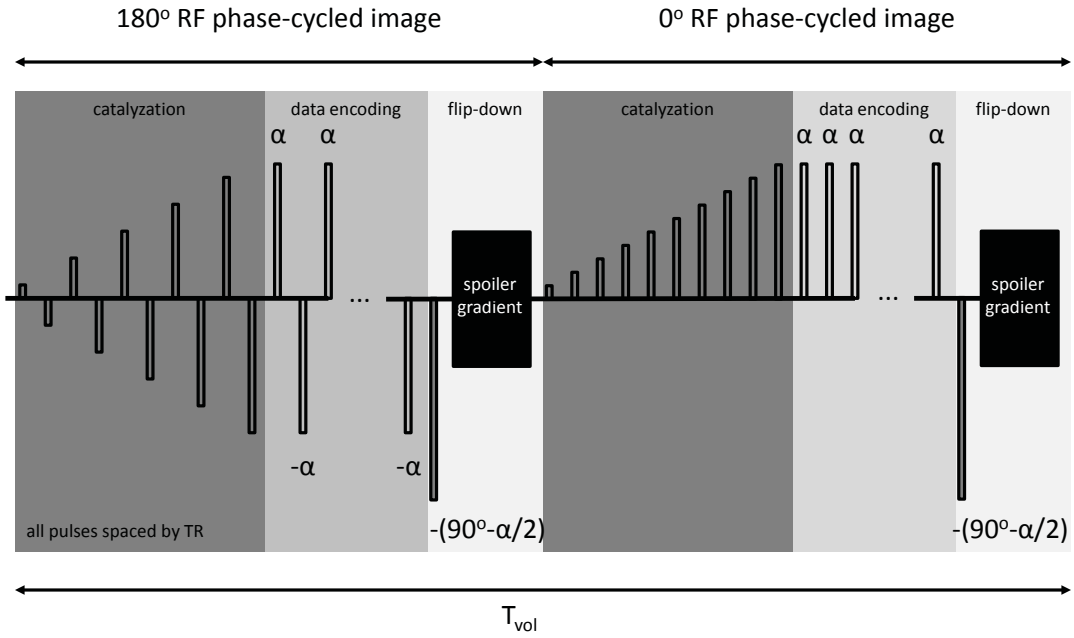

Figure 4.1: Schematic of the alternating SSFP pulse sequence used in all Monte Carlo simulations. Alternating SSFP acquisitions consisted of consecutive 180° and 0° RF phase-cycled balanced SSFP image volumes. Each image volume began with a 10-pulse linear ramp RF catalyzation and ended with a flip-down pulse (to tilt the 3D magnetization vector into the transverse plane) and gradient spoiling. The volume time, T_{vol}, was defined as the time to collect both images, including catalyzation.

Bloch simulations [25] were used to identify a smooth signal transition between steady states by comparing acquisitions employing: 1) RF catalyzation immediately after changes in RF phase cycling increment (as described above), 2) gradient spoiling immediately before changes in RF phase cycling increment, and 3) an $\alpha/2$ flip-back RF pulse or a novel (90°-$\alpha/2$) flip-down RF pulse applied immediately before gradient spoiling. Extravascular relaxation rates were used for Bloch simulations.

Figure 4.1 shows the alternating SSFP pulse sequence deemed optimal by Bloch simulations (see Results), which was used for all Monte Carlo simulations. Each image-volume acquisition was preceded by linear ramp RF catalyzation and terminated with a (90°-$\alpha/2$) flip-down pulse, to tilt pass-band magnetization into the transverse plane, and gradient spoiling. The purpose of the flip-down pulse was to reduce the amplitude of pass-band magnetization prior to switching the RF phase

cycling, after which pass-band regions transition into stop-band regions. The flip-down pulse was phase cycled by an additional 180° (i.e., it had the same phase as the preceding RF pulse in 180° RF phase-cycled acquisitions, and was 180° out of phase with the preceding RF pulse in 0° RF phase cycled acquisitions). Gradient spoiling was simulated by setting the transverse magnetization to zero. Bloch simulations using transverse magnetization nulling to achieve spoiling agreed very closely with those using realistic gradient phase twist, with parameters matching our experimental conditions (20 mT/m gradients for 2 ms, see Chapter 5), and so nulling was used thereafter.

Monte Carlo simulations of alternating SSFP were conducted for volume times (T_{vol}) of 1-5 s, defined as the time to complete both RF phase-cycled acquisitions, including catalyzation. An image-to-image steady state signal level was established before commencing data recording. To reduce Monte Carlo simulation time, the magnetization was initialized to the alternating SSFP steady state obtained from Bloch simulations of multiple image volume repetitions using the off-resonance frequency at the initial position of the diffusion path. This initial magnetization was then evolved in the Monte Carlo model for T_{vol} or 2 s, whichever was greater (the signal was observed to reach a diffusion-perturbed steady state in well-under 1 s), before commencing data recording. The off-resonance signal profiles from the complementary RF phase-cycled acquisitions were combined, using Maximum Intensity Projection (MIP) [62] or Sum of Squares (SOS) [63] combination strategies, to produce a single, banding-artifact-suppressed off-resonance profile each T_{vol}.

Pass-band SSFP

The signal and BOLD contrast from alternating SSFP simulations was compared with that from matched $T_R/T_E/\alpha$ pass-band SSFP simulations. For pass-band SSFP simulations, the magnetization was initialized into steady state [64] using the balanced-SSFP equations [30] (at the appropriate α, T_R, T_1, T_2, and RF phase-cycling increment), and evolved in the Monte Carlo model for 2 s prior to commencing data recording.

4.3 Results

4.3.1 Bloch Simulations

Bloch simulations were used to identify a suitable implementation of alternating SSFP. The ideal alternating SSFP signal trajectory is an instantaneous transition between 180°- and 0°-RF phase cycled balanced SSFP signal levels (Fig. 4.2a). Spins at $\Delta\omega = 0$ and $\Delta\omega = \pm 0.5/T_R$ alternate between the pass-band centre and the stop-band centre each image. Spins at $\Delta\omega = \pm 0.25/T_R$ are midway between the pass-band centre and the stop-band centre and experience the same trajectory each image. Given enough time the alternating SSFP signal would converge to that of balanced SSFP (i.e., Fig. 4.2b-d would match Fig. 4.2a at $t = T_{vol}/2$ and at $t = T_{vol}$ for large T_{vol}).

Simply switching the RF phase cycling increment between images results in pronounced signal oscillations (Fig. 4.2b). Signal oscillations are problematic because they produce a point spread function with side-lobes that results in shifted, overlapping copies of the image (phase-encode artifacts, or ghosts, such as the familiar $N/2$ ghost in EPI). Adding a flip-back RF pulse and gradient spoiling before changing the RF increment, and linear ramp RF catalyzation after, greatly reduces signal oscillations across most off-resonance frequencies (Fig. 4.2c). However, the flip-back pulse produces large stop-band signal amplitude following RF increment changes (e.g., Fig. 4.2c, 1.5 s $< t <$ 2.0 s, -.25/T_R $< \Delta\omega <$ 0.25/T_R), and large-amplitude signal oscillations persist in the stop-band centre (e.g., Fig. 4.2c, 1.5 s $< t <$ 2.0 s, $\Delta\omega = 0$). Exchanging the flip-back for a flip-down RF pulse (Fig. 4.2d) results in a smoother signal transition between steady states with a uniform signal level across the pass-band off-resonance frequency range (0 s $< t <$ 1.5 s, -.25/T_R $< \Delta\omega <$ .25/T_R). Smooth variations in signal intensity are preferred to signal oscillations; the former produce a broadened point spread function that degrades image resolution, but without side-lobes, avoiding ghosts. The minimal signal oscillation in alternating SSFP suggests that imaging without significant phase-encoding artifacts is possible. This implementation (Fig. 4.2d) was used in all subsequent experiments and Monte Carlo simulations, which produced a signal response similar to that from Bloch simulations (e.g., Fig. 4.3).

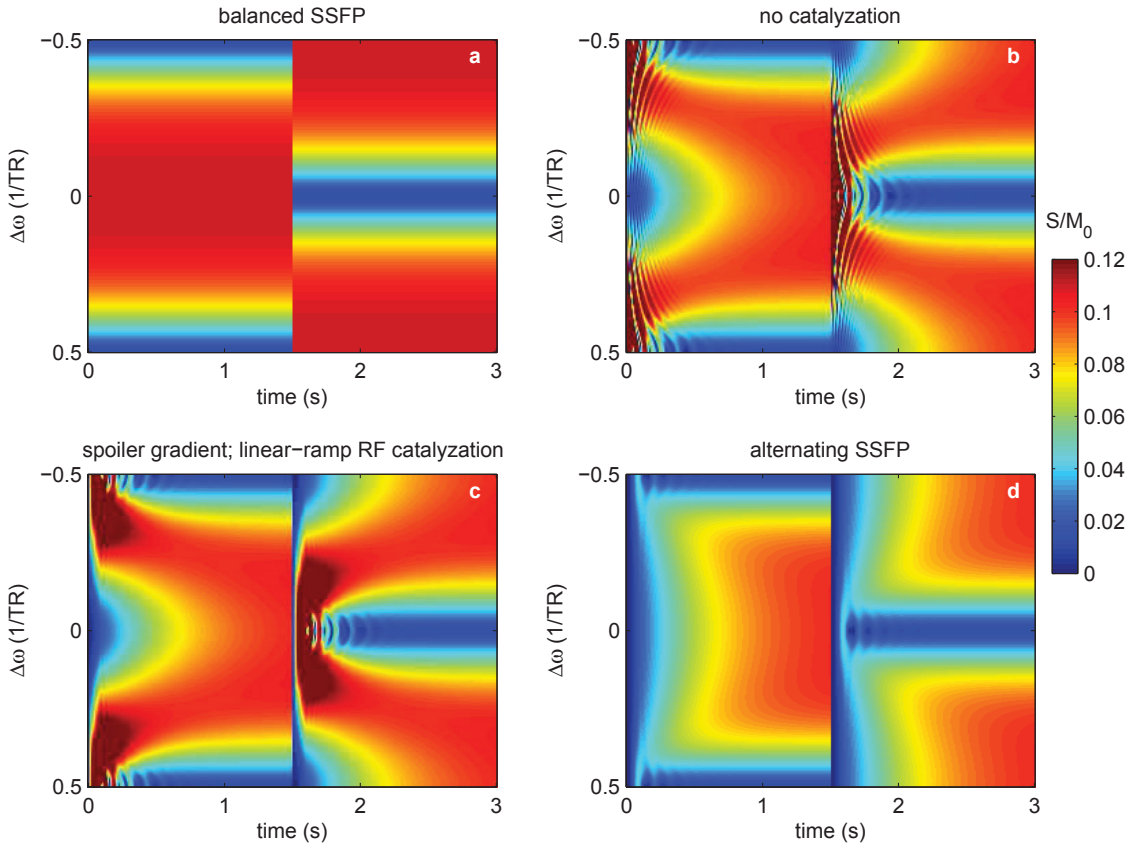

Figure 4.2: Bloch-simulated signal (S/M_0) (amplitude indicated by color bar) vs. time and off-resonance frequency ($\Delta\omega$) for alternating SSFP ($\alpha/T_R/T_E/T_{vol}$ = 30°/10 ms/5 ms/3 s). The RF phase cycling increment was changed from 180° to 0° at the midpoint (t = 1.5 s) of each image volume (RF increment = 180° for $t < 1.5$ s and 0° for $t > 1.5$ s). Signal is shown for: (a) the ideal alternating SSFP signal trajectory, fabricated by concatenating 180°- and 0°-RF phase cycled balanced SSFP Bloch simulation data, (b) the actual trajectory caused by changing the RF phase cycling increment only, (c) method (b) with an $\alpha/2$ flip-back RF pulse and gradient spoiling added prior to changing the RF phase cycling increment, and a 10-pulse linear ramp RF catalyzation train added after changing the RF phase cycling increment, and (d) method (c) with the $\alpha/2$ flip-back pulse replaced with a 90°-$\alpha/2$ flip-down RF pulse. The signal response in (d) using $\alpha/2$ RF catalyzation was very similar, and is not shown.

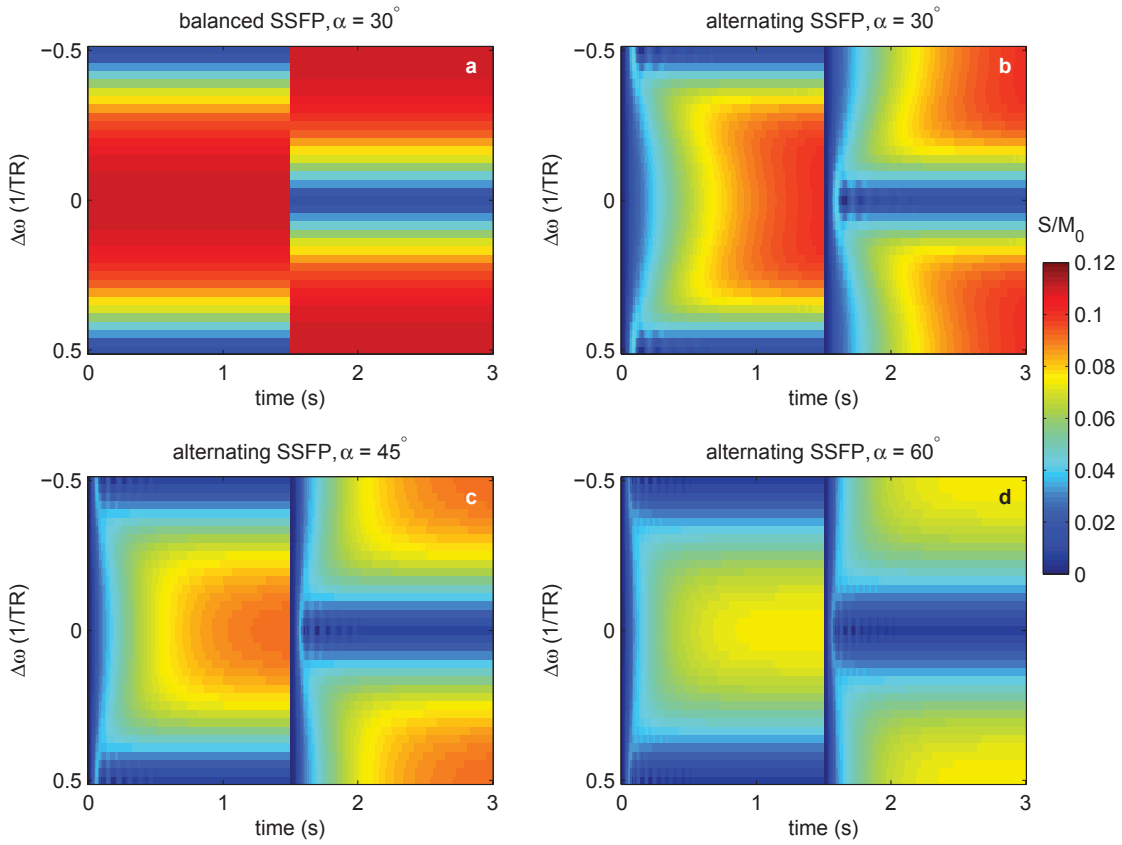

Figure 4.3: Monte-Carlo-simulated resting signal (S/M_0) (amplitude indicated by color bar) vs. time and off-resonance frequency ($\Delta\omega$) for alternating SSFP ($T_R/T_E/T_{vol}$ = 10 ms/5 ms/3 s). Simulations used the microvascular model (f = 2 %, R = 3 μm). The RF phase cycling increment was changed from 180° to 0° at the midpoint (t = 1.5 s) of each image volume (RF increment = 180° for $t < 1.5$ s and 0° for $t > 1.5$ s). Signal is shown for: (a) the ideal alternating SSFP signal trajectory, fabricated by concatenating 180°- and 0°-RF phase cycled balanced SSFP ($\alpha = 30°$) Monte Carlo simulation data, and actual alternating SSFP simulations (b-d) at flip angles of 30, 45, and 60°, respectively.

4.3.2 Monte Carlo Simulations

Figure 4.4 shows BOLD activation induced changes ($\Delta S/M_0$) in the resting signal time-courses of Fig. 4.3. Alternating SSFP BOLD contrast is entirely suppressed after RF catalyzation and increases with time. Since BOLD contrast is primarily encoded at the **k**-space centre, reverse-centric **k**-space ordering should be used to maximize alternating SSFP BOLD sensitivity. Comparison with Fig. 4.3 reveals that alternating SSFP BOLD contrast recovery lags signal recovery. For example, centre-of-pass-band alternating SSFP BOLD contrast reaches 70 % of the corresponding balanced SSFP value (Fig. 4.4a vs. Fig. 4.4b at $t = 1.5$ s, $\Delta\omega = 0$) whereas alternating SSFP signal reaches 90 % of the corresponding balanced SSFP value (Fig. 4.3a vs. Fig. 4.3b at $t = 1.5$ s, $\Delta\omega = 0$).

The rate of alternating SSFP BOLD contrast recovery increases with increased flip angle. For example, the percentage of centre-of-pass-band balanced SSFP BOLD contrast achieved at the midpoint (750 ms) of each alternating SSFP acquisition is 35 %, 70 %, and 85 % for $\alpha = 30°$, 45°, and 60°, respectively. BOLD contrast levels matching that of conventional pass-band SSFP (Fig. 4.4a, $t = 1.5$ s, $\Delta\omega = 0$) are attained with high-flip-angle ($\alpha = 45$-$60°$) alternating SSFP (Fig. 4.4c-d) by the end of the 1.5 s RF train. Higher flip angles also reduce the variation in alternating SSFP BOLD contrast across the pass-band off-resonance frequency range ($-.25/T_R < \Delta\omega < 0.25/T_R$, $0 < t < 1.5$ s). Maximal, uniform BOLD contrast across the pass-band off-resonance frequency range is paramount for producing fMRI maps that are robust to imperfect shim conditions. Acquisitions at different T_{vol} have very similar profile shapes at matched post-catalyzation time-points and are not shown.

MIP and SOS acquisition combination strategies were investigated for removing banding artifacts in alternating SSFP (Fig. 4.5). SOS acquisition combination results in greater signal and BOLD contrast than MIP at most off-resonance frequencies. However, SOS also results in greater BOLD contrast variation with off-resonance frequency. Figure 4.5 suggests that alternating SSFP ($\alpha = 45$-$60°$, MIP) can provide BOLD contrast levels comparable to that of on-resonant pass-band SSFP ($\alpha = 30°$) across all off-resonance frequencies.

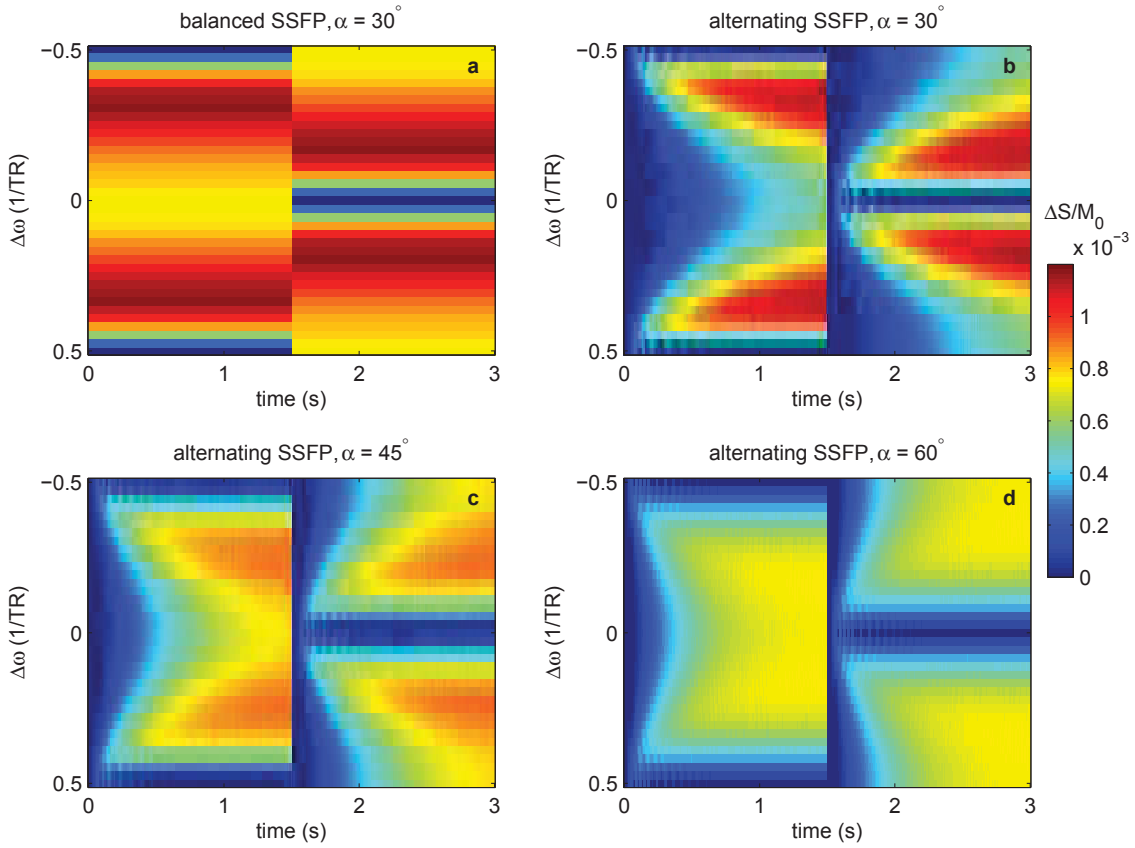

Figure 4.4: Monte-Carlo-simulated BOLD contrast ($\Delta S/M_0$) (amplitude indicated by color bar) vs. time and off-resonance frequency ($\Delta\omega$) for alternating SSFP ($T_R/T_E/T_{vol}$ = 10 ms/5 ms/3 s). Simulations used the microvascular model (f = 2 %, R = 3 μm). The RF phase cycling increment was changed from 180° to 0° at the midpoint (t = 1.5 s) of each image volume (RF increment = 180° for $t < 1.5$ s and 0° for $t > 1.5$ s). Contrast is shown for: (a) the ideal alternating SSFP BOLD contrast trajectory, fabricated by concatenating 180°- and 0°-RF phase cycled balanced SSFP (α = 30°) Monte Carlo simulation data, and actual alternating SSFP simulations (b-d) at flip angles of 30, 45, and 60°, respectively.

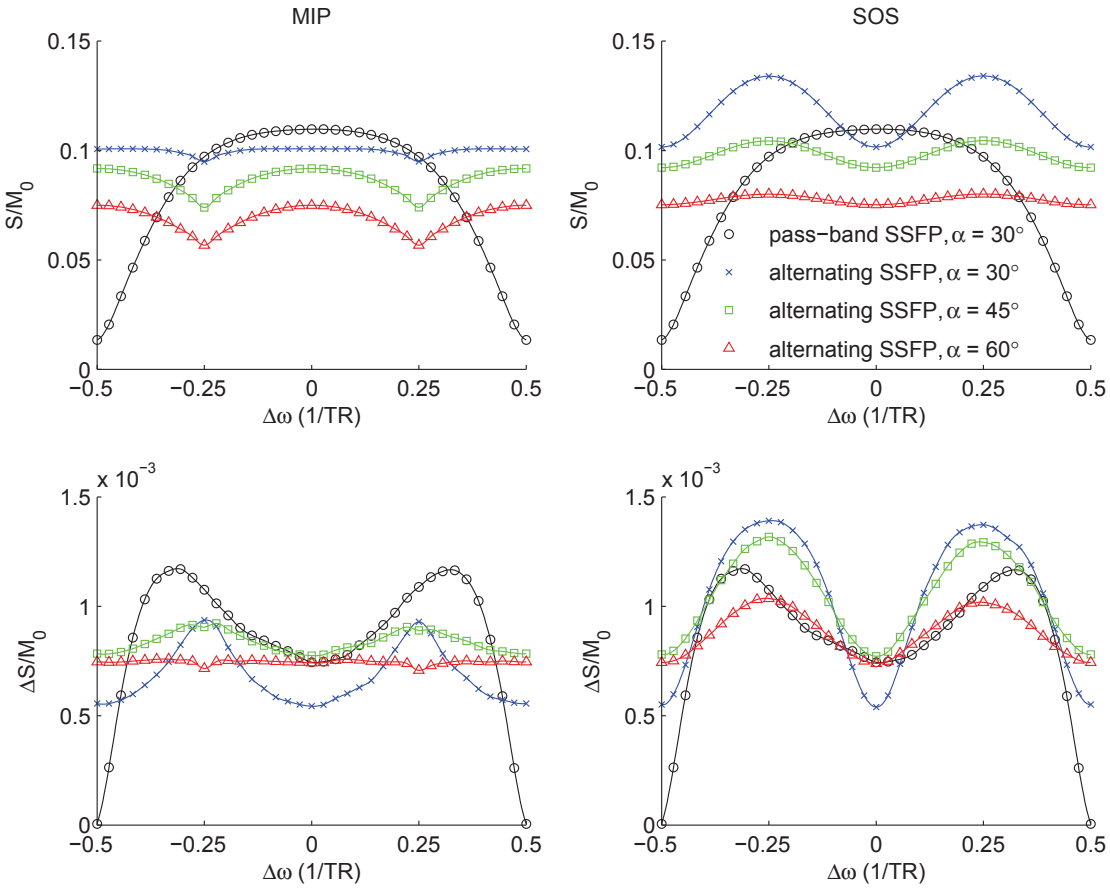

Figure 4.5: Monte-Carlo-simulated resting signal (top row) and corresponding BOLD contrast (bottom row) vs. off-resonance frequency in the microvascular model for alternating SSFP ($T_R/T_E/T_{vol}$ = 10 ms/5 ms/3 s). Data are plotted for MIP (left column) and SOS (right column) acquisition combination strategies. Each plot includes alternating SSFP data at three flip angles (30, 45, and 60°), and, for reference, pass-band SSFP (matched T_E and T_R, $\alpha = 30°$). Alternating SSFP profiles were generated by combining the profiles of the 180° and 0° RF phase-cycled acquisitions at their proposed **k**-space centers (the last T_R cycle of the 180° ($T_{vol}/2$) and 0° (T_{vol}) RF phase-cycled data acquisition trains, respectively).

4.4 Discussion

In this work, Monte Carlo simulations were used to optimize alternating SSFP for two-acquisition pass-band SSFP fMRI from a single paradigm run.

4.4.1 Signal vs. BOLD Contrast Behavior

On-resonance[4], the alternating SSFP signal can be expressed as:

$$S = S_{stst}(1 - \exp(-t/T_1^*)), \tag{4.2}$$

where S_{stst} is the steady state signal level, t is time (RF phase cycling increment changed at $t = 0$), and T_1^* is a characteristic time-constant describing the transient phase of balanced SSFP [31, 65]

$$(1/T_1^*) = (1/T_1)\cos^2(\alpha/2) + (1/T_2)\sin^2(\alpha/2). \tag{4.3}$$

For tissues with $T_2 < T_1$, T_1^* decreases with increased flip angle, resulting in accelerated signal recovery. Assuming that on-resonant BOLD contrast in alternating SSFP can be characterized by a change in the R_2 ($R_2 = 1/T_2$) relaxation rate, ΔR_2, alternating SSFP BOLD contrast may be approximated as (see Appendix A.1):

$$\Delta S \approx \Delta S_{stst}(1 - \exp(-t/T_1^*)) - At\exp(-t/T_1^*), \tag{4.4}$$

where ΔS_{stst} is the steady state contrast level, and

$$A = S_{stst}|\Delta R_2|\sin^2(\alpha/2). \tag{4.5}$$

The second term ($A \geq 0$) in Eq. 4.4 accounts for the lag in BOLD contrast growth following catalyzation, relative to signal growth, observed in alternating SSFP (Fig. 4.3 vs. Fig. 4.4).

4.4.2 Recommended Implementation

Our results suggest that alternating SSFP has the potential for two-acquisition pass-band SSFP fMRI from a single paradigm run with little scan-time overhead from catalyzation. Recommended acquisitions involve alternating between 180°- and 0°-RF

[4] i.e., the portion of the alternating SSFP signal profile chosen by MIP image combination

phase-cycled pass-band SSFP 3D image volumes, each prepared with linear ramp RF catalyzation (10 pulses) and terminated with a (90°-α/2) flip-down pulse and gradient spoiling to minimize the signal fluctuations caused by changing the RF phase-cycling increment. Consecutive images are then combined in post-processing to generate single, artifact-suppressed images. MIP or SOS image combination strategies are recommended, with MIP for applications requiring uniform BOLD sensitivity across off-resonance frequencies, and SOS to maximize total BOLD sensitivity where uniformity is less important (Fig. 4.5).

BOLD contrast is suppressed in alternating SSFP following RF catalyzation and increases during the data acquisition train (Fig. 4.4). Therefore, the centre of **k**-space should be encoded late in the data acquisition train to maximize BOLD sensitivity. Additionally, high flip angles (45-60°) should be used as they accelerate BOLD contrast development and reduce BOLD contrast off-resonance sensitivity (figs. 4.4 and 4.5). BOLD contrast levels matching conventional ($\alpha = 30°$) pass-band SSFP are attained by 1.4 s of imaging post-catalyzation in alternating SSFP using a 45° flip angle. Therefore, alternating SSFP acquisitions having a 3 s combined image volume time (0.1 s RF catalyzation + 1.4 s data acquisition per image) should provide minimal loss of BOLD contrast relative to pass-band SSFP acquisitions. At $T_R = 10$ ms, this allows 140 T_R cycles to encode each image using a rapid 3D **k**-space encoding scheme such as segmented EPI or spiral. T_E can be chosen to maximize gradient-encoding efficiency, as balanced SSFP BOLD contrast is relatively independent of T_E at short T_R [23]. To illustrate, a whole-brain (256×256×128 mm^3 FOV) protocol with 4 mm isotropic resolution (32 z-phase encodes) would require the coverage of a 64x64 matrix with 4 in-plane EPI or spiral segments. This should be feasible at short-T_R (10-15 ms) using homodyne acquisitions and/or parallel imaging with in-plane acceleration factors of 2-4. Alternatively, coverage could be reduced to achieve high spatial resolution in regions of strong magnetic susceptibility-induced field gradients. Maximum BOLD sensitivity is achieved using 3D stack-of-EPI or stack-of-spiral imaging trajectories with z-phase encoding as the outer loop in reverse-centric order to encode the **k**-space center last. Additionally, adjacent z-phase encode steps should be paired in time to minimize eddy-current-induced phase-encode ghosts [66].

4.4.3 Drawbacks

Alternating SSFP results in reduced BOLD contrast compared to pass-band SSFP. This is because the pass-band region of a given image is the stop-band region of the previous image, and the signal is not allowed sufficient time to fully recover. As a result, alternating SSFP BOLD contrast is expected to be 0-30 % lower than that of pass-band SSFP, depending on RF flip angle, for above-recommended acquisitions.

Alternating SSFP results in reduced temporal resolution compared to pass-band SSFP. The RF catalyzation required to prevent phase-encode-ghosting, and the need to acquire two images to produce one artifact-free image, limit the temporal resolution of alternating SSFP to slightly less than half that of pass-band SSFP. Nevertheless, pass-band SSFP and conventional GRE fMRI techniques are unsuitable for imaging in macroscopic susceptibility-induced field gradient (SFG) regions.

SAR limitations may prevent the use of the optimum flip angle for alternating SSFP, depending on field strength. However, the T_R of alternating SSFP is relatively long compared to that typically used for traditional pass-band SSFP applications like cardiac CINE, which should permit the use of higher-than-typical flip angles.

4.4.4 Model Limitations

Our Monte Carlo model used simplified tissue models consisting of unary or binary vessel radii distributions, similar to those employed by others [23,24]. Simplified tissue models may misestimate the contrast from the extravascular compartment (contrast from the intravascular compartment depends only on blood volume). More detailed tissue models should be employed to precisely reproduce experimentally observed percent signal change values, as in [22]. Nevertheless, the value we obtained for the relative contribution to total balanced SSFP BOLD contrast from the extravascular compartment (30 %) is very similar to that derived from more detailed tissue models (33 % from fig. 6, $\alpha = 45°$, $f_b = 2.7$ % in [22]). We therefore anticipate that using more complicated tissue models would not change our conclusions.

The intravascular T_2 relaxation times used in our SSFP simulations were calculated from a Luz-Meiboom exchange model fit to data from in-vitro blood samples measured with a CPMG sequence [67]. In-vitro blood data measured with pass-band SSFP has also been fit to a Luz-Meiboom exchange model at two magnetic field

strengths (1.5 T and 3 T) and two T_R values (4 ms and 8 ms) [58], although a fit has not been done at 4 T. The pass-band SSFP and CPMG relationships result in the same BOLD percent signal change from the intravascular compartment at $B_0 = 3$ T, $T_R = 8$ ms, within fit parameter error. Given this agreement, we chose the CPMG relationship because it has been verified to robustly scale across a broad range of echo times (6-48 ms), magnetic field strengths (1.5-9.4 T), and blood oxygenation levels [36].

4.4.5 Conclusion

We propose RF-catalyzed alternating SSFP for two-acquisition pass-band SSFP fMRI from a single paradigm run. Our Monte Carlo simulations suggest that the RF phase-cycling increment can be alternated between image volumes in the two-acquisition method, with minimal signal oscillations, if each image acquisition is preceded by 10 linear-ramp RF catalyzation pulses, and terminated with a 90°-$\alpha/2$ flip-down pulse and gradient spoiling. For typical functional image volume times (3-5 s image pairs), we found this approach to result in 100 % of conventional pass-band SSFP BOLD contrast at the proposed **k**-space centre if high (45-60°) flip angles were used. MIP image combination of these image pairs resulted in uniform (under 20 % variation compared to over 130 % variation for single-acquisition pass-band SSFP) BOLD contrast across the entire off-resonance frequency spectrum. Alternating SSFP may allow functional MRI in SFG regions not possible with GRE acquisitions, due to signal dropout; SE acquisitions, due to low BOLD sensitivity; and conventional two-acquisition pass-band SSFP, due to inherent difficulties in interpreting combined functional runs. Alternating SSFP may be particularly useful at high fields, which worsen susceptibility artifacts in GRE scans, yet provide insufficient BOLD sensitivity for SE scans [16].

Chapter 5

Experimental Confirmation of Alternating SSFP Signal Behavior

5.1 Introduction

In chapter 4, theoretical modeling was used to identify a suitable alternating SSFP implementation. This chapter describes experiments that were conducted to test the theoretically-predicted alternating SSFP signal behaviour, and to compare image quality between alternating and conventional pass-band SSFP acquisitions.

5.2 Methods

5.2.1 Equipment

Experiments were conducted at 4 T using an Oxford magnet, with a body gradient coil provided by Tesla Engineering Ltd., an Agilent DirectDrive console, and a transverse electromagnetic (TEM) head coil for transmit/receive (Bioengineering Inc.). Maximum gradient amplitude and slew rate were limited to 35.5 mT/m and 140 T/m/s, respectively.

5.2.2 Pulse sequences

Pass-band and alternating SSFP were implemented as 3D sequences using phase encoding in the z-direction and interleaved spiral-out acquisitions in-plane (Fig. 5.1). The alternating SSFP pulse sequence was converted to a conventional pass-band SSFP sequence by: 1) holding the RF phase-cycling increment constant between image volumes, 2) substituting the linear catalyzation train with dummy cycles (to maintain a 2:1 pass-band SSFP to alternating SSFP temporal resolution ratio, facilitating analysis), and 3) omitting the flip-down pulse and spoiler gradients at the end of each image volume (i.e., an uninterrupted steady state was maintained at a given

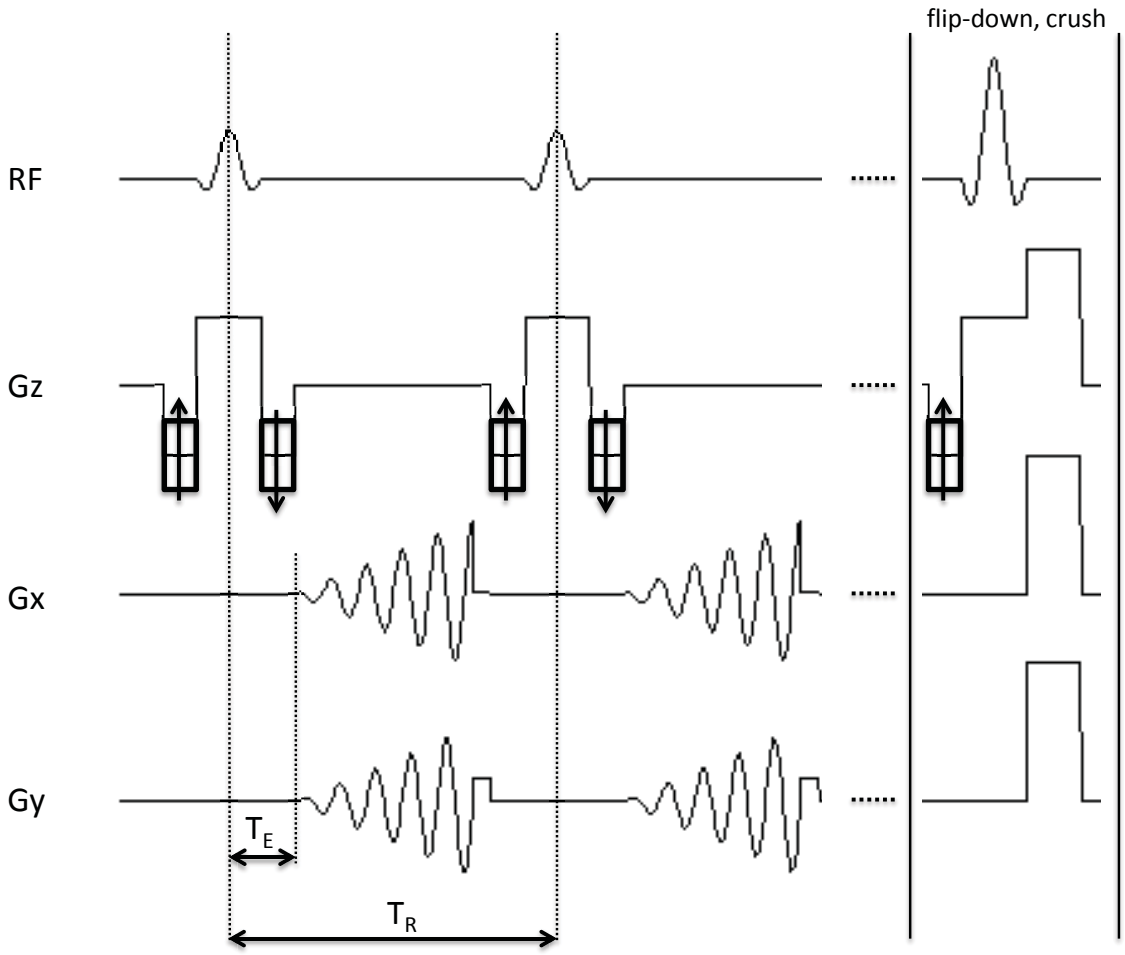

Figure 5.1: Experimental alternating SSFP pulse sequence. A 3D stack-of-spiral **k**-space trajectory was used, with 8 interleaved spiral-out acquisitions in-plane (inner loop), and phase-encoding in the z-direction (outer loop). z-phase encodes were acquired in reverse-centric order. Slab-select-refocus and z-phase encode gradients were combined to reduce the minimum T_R. The RF phase cycling increment was alternated between 0° and 180° each image volume. Each alternating SSFP image volume began with 10-20 linear-ramp RF catalyzation pulses, prior to commencing data acquisition, and ended with a 90°-$\alpha/2$ flip-down RF pulse followed by gradient spoiling.

RF-increment for the entire image timecourse).

5.2.3 Phantom Measurements

Signal time-courses were measured from a magnetic resonance spectroscopy phantom (Model 2152220, General Electric Company, Milwaukee, Wisconsin) ($T_1 = 360$ ms, $T_2 = 190$ ms) shimmed to the water peak. Signal time-courses were obtained by disabling z-phase encode and spiral imaging gradients. Off-resonance was mimicked by deliberately missetting the resonance transmit/receive offset. Measured signal trajectories were compared with those from numerical simulations using the Bloch equations at matched parameters. Bloch simulations used the experimentally measured T_1 and T_2 phantom relaxation times. Images were obtained from a resolution phantom (J1270, J.M. Specialty Parts, San Diego, CA) ($T_1 = 150$ ms, $T_2 = 90$ ms). Identical acquisition parameters were used for signal timecourse and phantom imaging experiments: $T_R = 10.8$ ms, $T_E = 0.8$ ms, $\alpha = 70°$, spiral out (8 interleaves), FOV 240×240×60 mm^3, matrix 64×64×16, $T_{vol} = 3.0$ s (1.5 s per RF phase cycled image volume), 10-pulse linear ramp RF catalyzation (10 dummy cycles for pass-band SSFP).

5.2.4 Human Images

Human images were obtained from a healthy volunteer. Pass-band and alternating SSFP acquisition parameters: $T_R = 10.0$ ms, $T_E = 0.7$ ms, $\alpha = 45°$, spiral out (8 interleaves), FOV 240×240×80 mm^3, matrix 64×64×16, $T_{vol} = 3.0$ s, 20-pulse linear ramp RF catalyzation (20 dummy cycles for pass-band SSFP).

5.2.5 SNR

SNR was estimated by calculating the ratio of the mean signal intensity in an ROI inside the object to that in an ROI in the air, outside of the object. The same signal and air ROIs were used when comparing SNR between alternating and pass-band SSFP.

5.3 Results

5.3.1 Signal timecourses

Theoretical and experimental alternating SSFP signal time-courses [1] agree quite well (Fig. 5.2). Theory curves differed slightly from experiment when transitioning to a new phase cycling increment by having larger oscillation duration when transitioning to the stop-band centre ($\Delta\omega = 0$, black line), and a smaller oscillation amplitude for marginally off-resonant spins ($\Delta\omega = 1/(12T_R)$, blue line).

5.3.2 Images

Similar image quality from a resolution phantom is observed for alternating and pass-band SSFP (Fig. 5.3). The largest percent difference occurs in the stop-band regions and is about 5%. Throughout the majority of the phantom the percent difference is less than 1%. SNR was calculated to be 88 for pass-band SSFP and 84 for alternating SSFP.

Similar image quality from a human volunteer is also observed for alternating and pass-band SSFP (Fig. 5.4). Signal levels in alternating SSFP are approximately 90-100 % and 30-40 % of that from pass-band SSFP in brain tissue and CSF, respectively. Bloch simulations predict an alternating-SSFP-to-pass-band-SSFP signal ratio of 98, 99, and 35 % for grey matter (T_1 = 1350 ms, T_2 = 77 ms [29]), white matter (T_1 = 1043 ms, T_2 = 56 ms [29]), and CSF (T_1 = 4000 ms, T_2 = 2000 ms), respectively. SNR was calculated to be 36 for pass-band SSFP and 31 for alternating SSFP.

Alternating SSFP permits banding-artifact-free pass-band SSFP with 3 s temporal resolution (time to acquire both images needed for banding-artifact removal) (Fig. 5.5).

5.4 Discussion

Excellent agreement between theoretical and experimental signal traces was observed for pass-band spins (Fig. 5.2, 0 s $< t <$ 1.5 s). Differences are apparent for transition- and stop-band spins (Fig. 5.2, 1.5 s $< t <$ 3.0 s, blue and black lines, respectively).

[1] signal time-courses correspond to sections through signal surfaces (e.g., Fig. 4.3) at constant off-resonance frequency

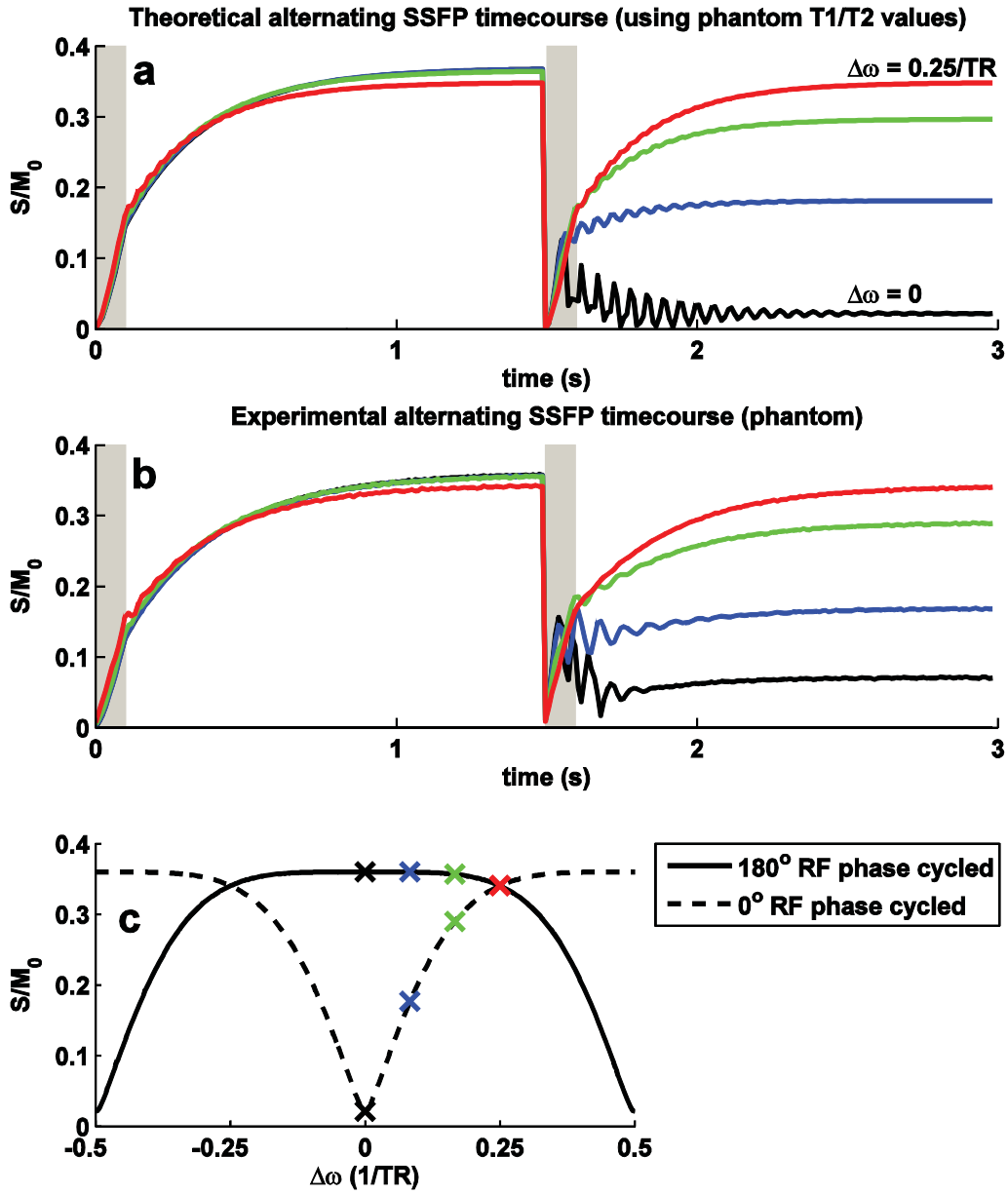

Figure 5.2: Theoretical (a) and experimental (b) alternating SSFP resting signal time-courses ($T_R/T_E/\alpha/T_{vol}$ = 10.8 ms/0.8 ms/70°/3 s). Experimental time-courses were measured from a magnetic resonance spectroscopy phantom; theoretical time-courses were obtained from Bloch simulations using measured phantom T_1 and T_2 values. Time-courses are shown at four off-resonance frequencies whose locations are shown on the pass-band SSFP signal vs. off-resonance profile (c). A global scaling factor was applied to experimental signal intensities so that experimental pass-band SSFP (180° RF phase cycled, $\Delta\omega = 0$) signal intensity matched that from Bloch simulations.

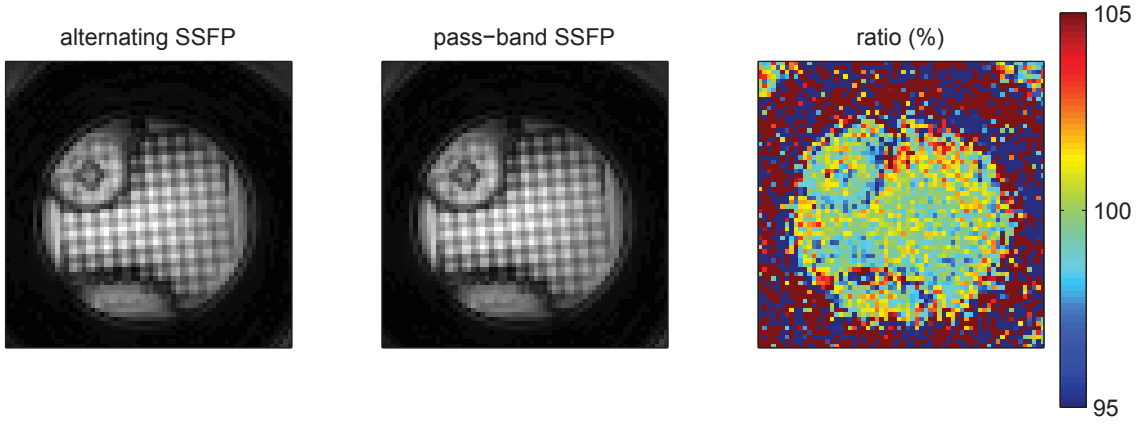

Figure 5.3: Images of a resolution phantom using pass-band SSFP and alternating SSFP (180° RF phase cycled images shown). Also shown is the ratio of alternating SSFP to pass-band SSFP (in %). Acquisition parameters: $T_R = 10.8$ ms, $T_E = 0.8$ ms, $\alpha = 70°$, spiral out (8 interleaves), FOV 240×240×60 mm^3, matrix 64×64×16, T_{vol} = 3.0 s (1.5 s for each RF phase cycled image volume). Alternating SSFP used linear ramp RF catalyzation (10 pulses). Ten "dummy cycles" were inserted in pass-band SSFP to match image volume time with alternating SSFP.

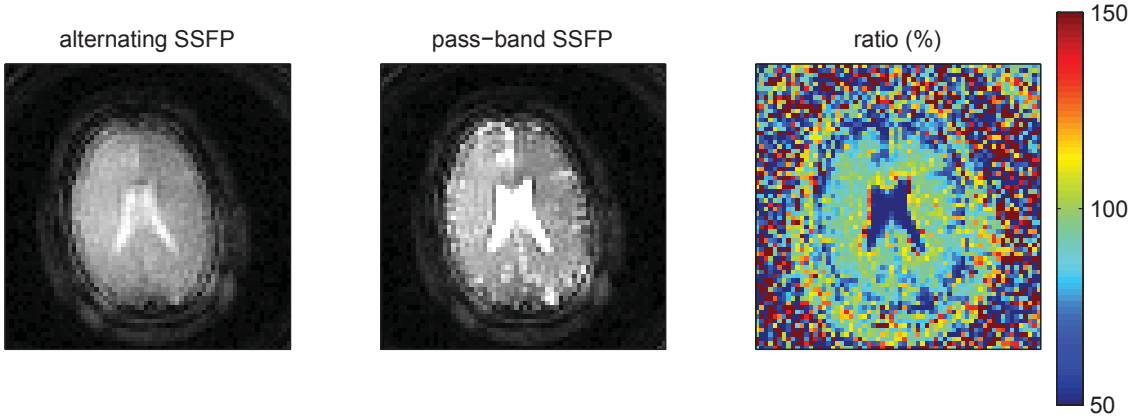

Figure 5.4: Images of a human head using pass-band SSFP and alternating SSFP (180° RF phase cycled images shown). Note that all SSFP images exhibited a fat chemical shift artifact in the form of a "halo" circling the brain, as no fat suppression was used. Also shown is the ratio of alternating SSFP to pass-band SSFP (in %). Acquisition parameters: $T_R = 10.0$ ms, $T_E = 0.7$ ms, $\alpha = 45°$, spiral out (8 interleaves), FOV 240×240×80 mm^3, matrix 64×64×16, $T_{vol} = 3.0$ s (1.5 s for each RF phase cycled image volume). Alternating SSFP used linear ramp RF catalyzation (20 pulses). Twenty "dummy cycles" were inserted in pass-band SSFP to match image volume time with alternating SSFP.

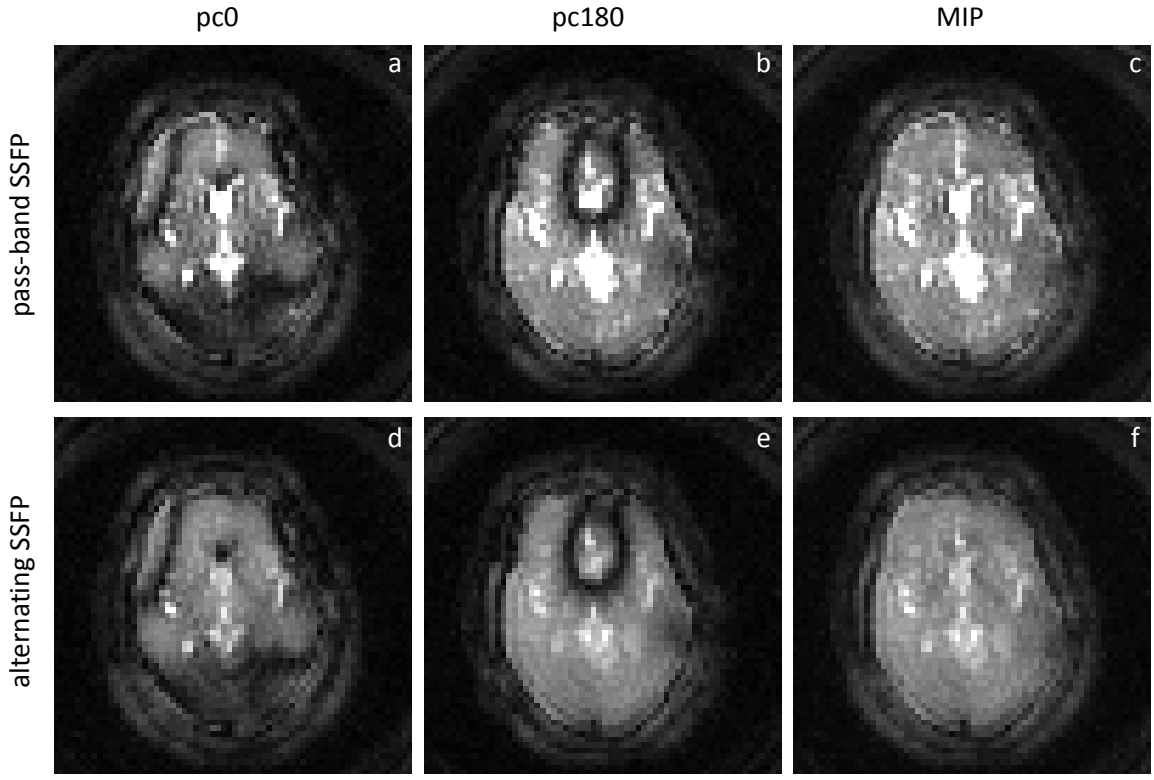

Figure 5.5: An inferior slice containing banding artifacts from the same data set in Fig. 5.4 is shown for pass-band SSFP (top row) and alternating SSFP (bottom row). For both techniques, 0°-RF-phase-cycled (pc0, left column), 180°-RF-phase-cycled (pc180, middle column), and MIP images (right column) are shown. Five seconds of dead-time (dummy cycles) was inserted between the acquisition of complementary pass-band SSFP images (a and b), to ensure acquisition occurred in the steady state. The complementary alternating SSFP images (d and e) needed for banding-artifact removal were consecutively acquired in a total time of 3 s.

Theoretical signal traces assume a perfectly homogeneous magnetic field; experimental signal traces contain spins from a distribution of off-resonance frequencies due to magnetic field inhomogeneity. The balanced SSFP signal magnitude and phase vary more strongly with off-resonance frequency in the transition- and stop-band. Therefore, transition- and stop-band signal traces are expected to be more dependent on the underlying frequency distribution than pass-band signal traces. This may account for the observed differences between theory and experiment.

Alternating SSFP does not result in substantial image artifacts (figs. 5.3 to 5.5), and maintains over 80 % of the SNR of pass-band SSFP. Normally a reduction in image SNR implies a reduction in BOLD sensitivity. However, alternating SSFP also suppresses CSF signal (Fig. 5.4). This should improve BOLD sensitivity, because CSF does not contribute to the BOLD signal but does contribute to the physiological noise. Quantitative BOLD sensitivity comparisons between alternating and pass-band SSFP involving rat hypercapnia and human visual stimulation studies are detailed in chapters 6 and 7, respectively.

5.4.1 Conclusion

Theoretical predictions for the alternating SSFP signal behaviour are in agreement with experiment. Alternating SSFP does not result in image artifacts, maintains over 80 % of the SNR of conventional pass-band SSFP images, and permits banding-artifact-free pass-band SSFP with 3 s temporal resolution.

Chapter 6

Rat Hypercapnia Studies

6.1 Introduction

In chapter 5 experiments were conducted to confirm theoretical predictions for the alternating SSFP signal behaviour, and to verify that alternating SSFP produced images of comparable quality to conventional pass-band SSFP. In this chapter, experiments were conducted to evaluate the BOLD sensitivity of alternating SSFP.

While the target of alternating SSFP is human fMRI, initially alternating SSFP was implemented on a 3 T small animal magnet and tested using a hypercapnia task in a rat model. Rat fMRI permits higher BOLD contrast-to-noise ratio (CNR) than human fMRI because longer scans can be acquired, motion is less pronounced, and task-compliance is not an issue. Higher BOLD CNR allows for the detection of smaller effect sizes, providing greater precision for optimizing acquisitions parameters and comparing pulse sequences.

In this study, experiments were first conducted to confirm Monte Carlo simulation predictions for the optimum flip angle and image combination strategy for alternating SSFP fMRI. Following this, alternating SSFP was compared with balanced SSFP[1] fMRI for: 1) the ability to recover BOLD sensitivity in balanced SSFP stop-band regions of interest (ROIs), and 2) the ability to maintain BOLD sensitivity in balanced SSFP pass-band ROIs.

[1]This study investigated fMRI of the whole brain, which could not be contained in a single pass-band. To avoid confusion, therefore, we avoid the term pass-band SSFP and instead refer to balanced SSFP in high-signal (pass-band) and low-signal (stop-band) regions (which coexist in a single balanced SSFP image when the range of off-resonance frequencies is large).

6.2 Methods

6.2.1 Alternating and balanced SSFP sequences

Alternating SSFP image time-courses consisted of interleaved 0°- and 180°-RF-phase-cycled balanced SSFP image volume acquisitions. Linear-ramp RF-catalyzation [21] (20 pulses) preceded each image volume acquisition to minimize the signal fluctuations caused by changing the RF phase-cycling increment. This consisted of stepping the flip angle (α) from $\alpha/20$ to α over the first 20 RF pulses following an RF-increment change, during which no data was acquired. Each image volume acquisition was terminated with an $\alpha/2$ flip-back pulse [31].[2] This pulse was applied at time T_R after the last pulse in the balanced SSFP RF train to increase the longitudinal magnetization of all pass-band regions, regardless of off-resonance frequency. Gradient spoiling was applied immediately following the flip-back pulse to destroy remaining transverse magnetization.

Alternating SSFP was implemented as a 3D sequence with **k**-space encoding performed using an interleaved stack-of-spiral-out gradient trajectory (Fig. 6.1). Phase encoding in the z-direction was reverse-centric ordered to place the **k**-space centre last in the data acquisition train, where alternating SSFP BOLD sensitivity is maximized according to Monte Carlo simulations (see Chapter 4). Z-phase encodes were paired to minimize eddy-current-induced phase-encode artifacts [66]. Minimizing T_E, which included combining the z-phase encode and slab-select gradients, maximized the readout duty cycle. Alternating SSFP image pairs were combined using maximum intensity projection (MIP) [62] or sum-of-squares (SOS) [63] to produce a single, banding-artifact-free image. The alternating SSFP image volume time was defined as the time to collect both images needed to produce the combined image.

The alternating SSFP pulse sequence was converted to a conventional balanced SSFP sequence by: 1) holding the RF phase-cycling increment constant between image volumes, 2) substituting the linear catalyzation train with 20 "dummy cycles" during which steady state was maintained but no data was acquired (to maintain a 2:1 balanced SSFP to alternating SSFP temporal resolution ratio, facilitating analysis),

[2] I discovered the (90°-$\alpha/2$) pulse after completing the Rat study.

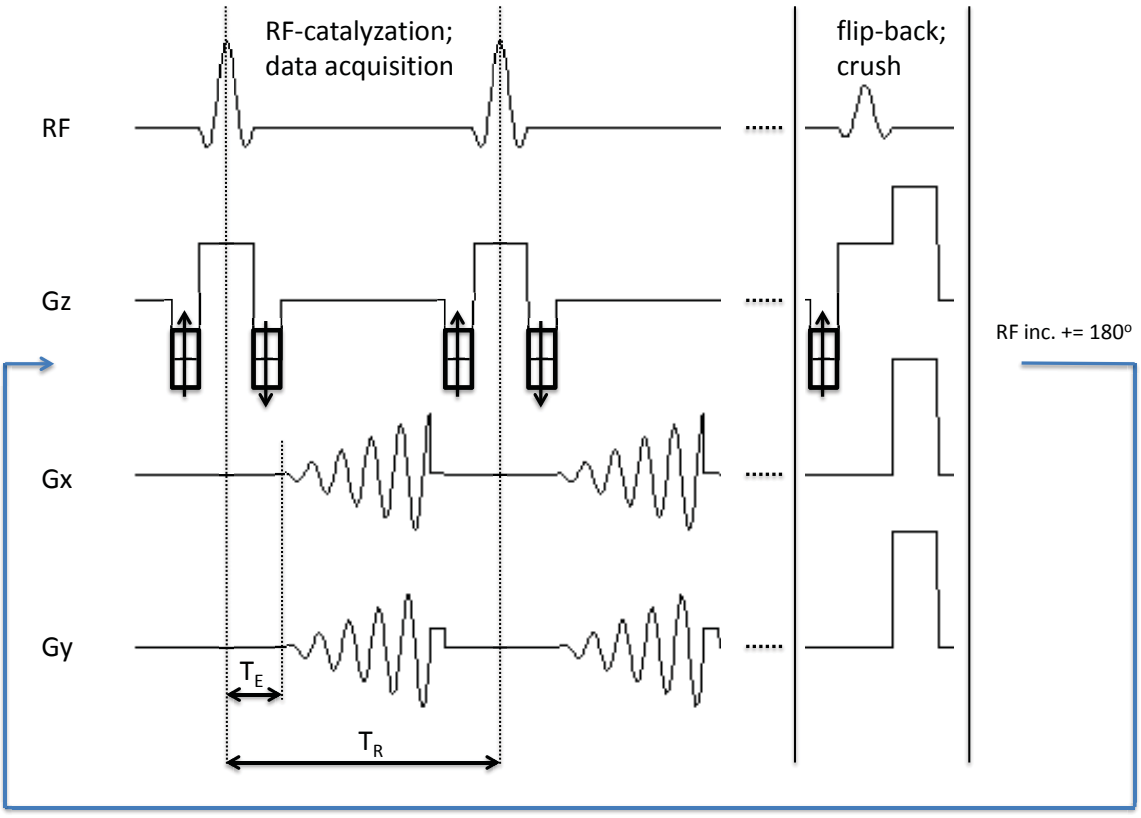

Figure 6.1: Alternating SSFP pulse sequence.

and 3) omitting the flip-back pulse and crusher gradients at the end of each image volume (i.e., an uninterrupted steady state was maintained at a constant RF-increment for the entire image timecourse).

6.2.2 Acquisition

All experimental procedures were approved by local ethics boards and adhered to the guidelines of the Canadian Council on Animal Care. MRI acquisitions were performed using a Magnex Scientific 3 T magnet with 0.2 T/m gradients (Oxford, UK), interfaced with an Agilent DirectDrive Console (Palo Alto, CA). A 52 mm inner diameter quadrature radiofrequency coil, built in-house, was used to transmit and receive.

Six adult male Long-Evans rats (Charles River Laboratories, Wilmington, MA; mean weight: 239 g, range: 221-263 g) were anesthetized via an intraperitoneal injection of urethane (1.6 g/kg). Urethane does not have a significant effect on neurotransmission, neuronal firing, or neurovascular coupling (e.g., [68]). Rats were immobilized using a head holder with ear bars (built in-house). A nose cone was placed over the snout for administration of gases. The hypercapnic challenge was preceded by a 1 min baseline scan during which the rat breathed medical air. This was followed by 4 min of 5 % CO_2 (balance air) alternated with 4 min of medical air, repeated twice (17 min. total). Throughout the experiment, respiration rate was monitored and animal temperature was maintained at approximately 37 $^{\circ}C$ via a feedback-controlled warm air heater system (Small Animal Instruments, Inc., Stony Brook, NY). The hypercapnic challenge was applied 5 times per rat to acquire two balanced SSFP fMRI data sets (with different RF increments), and three alternating SSFP fMRI data sets (with different flip angles). Acquisition parameters are summarized in Table 6.1. Scan order was randomized across animals. Each data set began with the acquisition of several dummy volumes to ensure the establishment of an image-to-image steady state signal level prior to data recording. Following the functional runs, an anatomic image with 200 μm isotropic resolution was acquired using 3D balanced SSFP (T_R = 10 ms, T_E = 5 ms, 50° flip, 160×160×160 matrix, 35×35×32 mm^3 field of view (FOV), 3D Cartesian **k**-space trajectory, MIP combination of 0° and 180° RF phase-cycled acquisitions, 8 image averages, 68 min total acquisition time).

Sequence	Flip angle (°)	RF-increment (°)	T_{vol} (s)
1 balanced SSFP	30	180-180-180-180 ...	1.5
2 balanced SSFP	30	0-0-0-0 ...	1.5
3 alternating SSFP	30	180-0-180-0 ...	3.0*
4 alternating SSFP	45	180-0-180-0 ...	3.0
5 alternating SSFP	60	180-0-180-0 ...	3.0

Table 6.1: Pulse sequence acquisition parameters.
Common to all sequences: 3D acquisition (stack of spirals), whole-brain coverage FOV (x×y×z) = (35×35×24mm^3), 8 shot in-plane spiral-out, 16 z phase encodes, matrix (x×y×z) = (64×64×16), T_R = 10.1 ms, T_E = 0.7 ms. Each image was acquired with a constant RF-increment. In alternating SSFP, the RF-increment was alternated between image volumes.
*Image volume time was defined as the time to collect an image pair in alternating SSFP.

6.2.3 Analysis

Prior to all fMRI analysis, consecutively-acquired balanced SSFP image pairs were averaged, to match the temporal resolution to the alternating SSFP combined-image-volume time (given that two balanced SSFP images can be acquired in the time to collect one alternating SSFP image). FMRI motion correction was performed in Statistical Parametric Mapping [69] with the SPMMouse toolbox [70]. After highpass temporal filtering (Gaussian-weighted least-squares straight line fitting, highpass filter cutoff = 480 s) and spatial smoothing (825 μm full width at half maximum Gaussian kernel), fMRI statistical analysis was performed in the FMRIB Software Library [71] using the general linear model in FEAT [72, 73]. Activation was modeled as a boxcar function representing the hypercapnia paradigm, convolved with a sine basis function (120 s window). A brain mask was automatically generated from the anatomical image by using the segmentation function in SPM [74]. Rat-specific tissue priors were used [70,75]. The resulting gray matter, white matter, and CSF masks were combined to form a brain mask. This brain mask was registered to the functional images and applied as a pre-threshold mask. T-contrasts were calculated comparing hypercapnic and baseline states. Statistical significance was determined using a cluster-level correction for multiple comparisons ($z > 2.3$, $p < 0.05$).

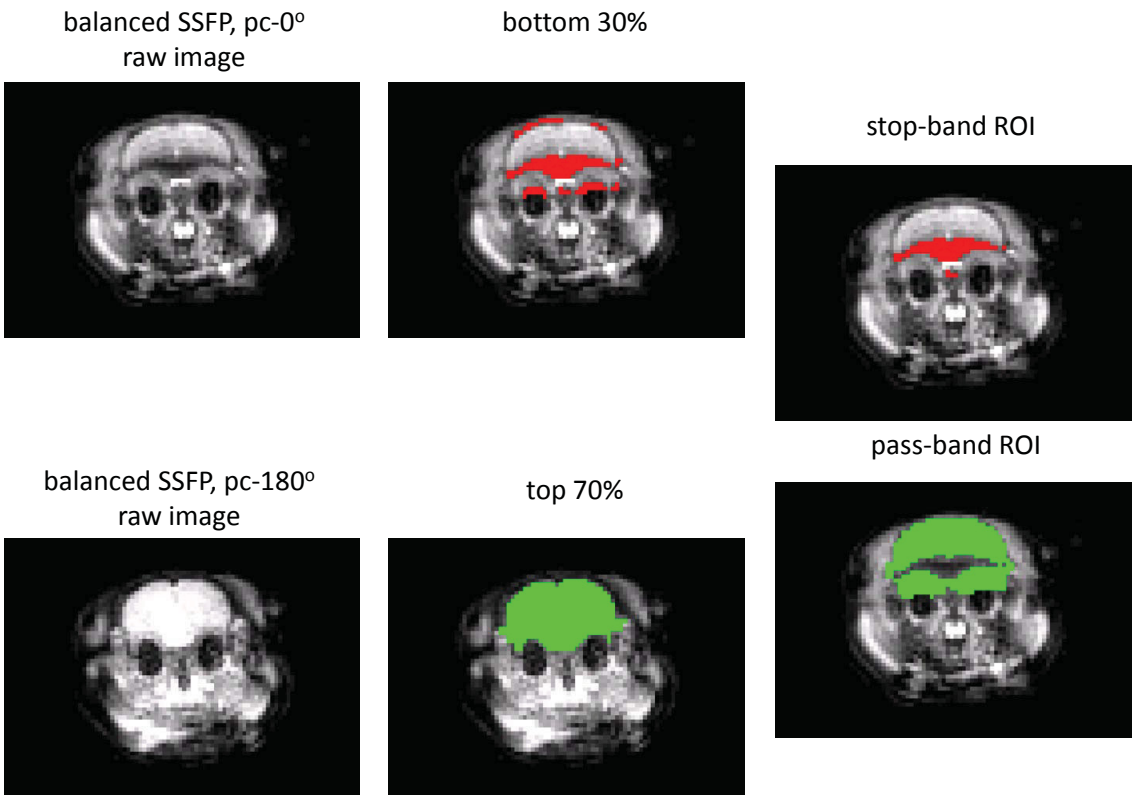

Figure 6.2: Automated stop-band ROI identification method. Co-registered 0° (pc-0°) and 180° (pc-180°) RF-phase-cycled balanced SSFP raw images (representative animal, coronal slice), and overlaid thresholded brain pixel intensity masks (bottom 30 % and top 70 %). Balanced SSFP pc-0° stop-band ROIs were identified as those pixels in the bottom 30 % of the pc-0° image that were also in the top 70 % of the pc-180° image.

ROI Analysis

For each run, functional images were registered to the anatomic b-SSFP image using FSL's FLIRT [76,77] (six degrees of freedom, no search). Registrations were manually evaluated. Registration between the different functional runs was then achieved by concatenating registration parameters, as appropriate.

Alternating SSFP was compared to balanced SSFP in high-signal (pass-band) and low-signal (stop-band) regions of interest (ROIs) (within the brain). Stop-band ROIs were identified as regions of low signal intensity that became regions of high signal intensity when the RF phase-cycling increment was inverted. This procedure, illustrated in Fig. 6.2, was automated: given a pair of 0°- and 180°-RF-phase-cycled images A and B, the stop-band ROI for image A was identified as those pixels in the

bottom 30 % of signal intensities in image A that were also in the top 70 % in image B. Several intensity thresholds were considered, with 30/70 % deemed to provide the best combination of stop-band sensitivity and specificity, based on visual inspection. Each functional run's mean image was used in the ROI generation routine. The pass-band ROI was defined as those pixels not contained in the stop-band ROI. In order to create pass- and stop-band ROIs for alternating SSFP, the functional image time-courses were reconstructed without image combination, and the temporal means of the 180°- and 0°-RF phase-cycled images were calculated separately.

Balanced- and alternating-SSFP scans were compared in the aforementioned stop- and pass-band ROIs. Comparison metrics included: extent of activation (i.e., the percentage of significantly activated voxels in a given ROI), mean z-score, and image signal-to-noise ratio (SNR) (the latter two reported as averages across the entire ROI, not just for voxels surpassing statistical thresholds). Image SNR was estimated by dividing the mean signal within the ROI by the mean signal within an ROI located in the air, outside of the rat. Mean and standard error across animals was reported. In Matlab, one-way ANOVAs and paired t-tests were used to compare metrics between the different flip angles of alternating SSFP, and between alternating and balanced SSFP, respectively.

In general, stop-bands will occur in both the 0° and 180° RF phase-cycled images, unless the entire brain can be shimmed to lie within a single pass-band. Given that we expect whole-brain activation from the hypercapnia manipulation, the fMRI response in stop-band ROIs is expected to be independent of the RF-phase-cycling increment[3] (likewise for pass-band ROIs). Therefore, balanced SSFP metrics in a given ROI were reported as the weighted average (by number of voxels in the ROI) from both phase-cycled scans.

In alternating SSFP, the stop-band region of a given image becomes the pass-band region of the next image. Stop-band metrics were reported from regions that resided in the stop-band ROI from either RF phase-cycled image volume. Pass-band metrics were reported for those regions that did not lie in the stop-band region of either RF phase-cycled image.

[3]Ignoring physiological differences between brain regions/tissue types

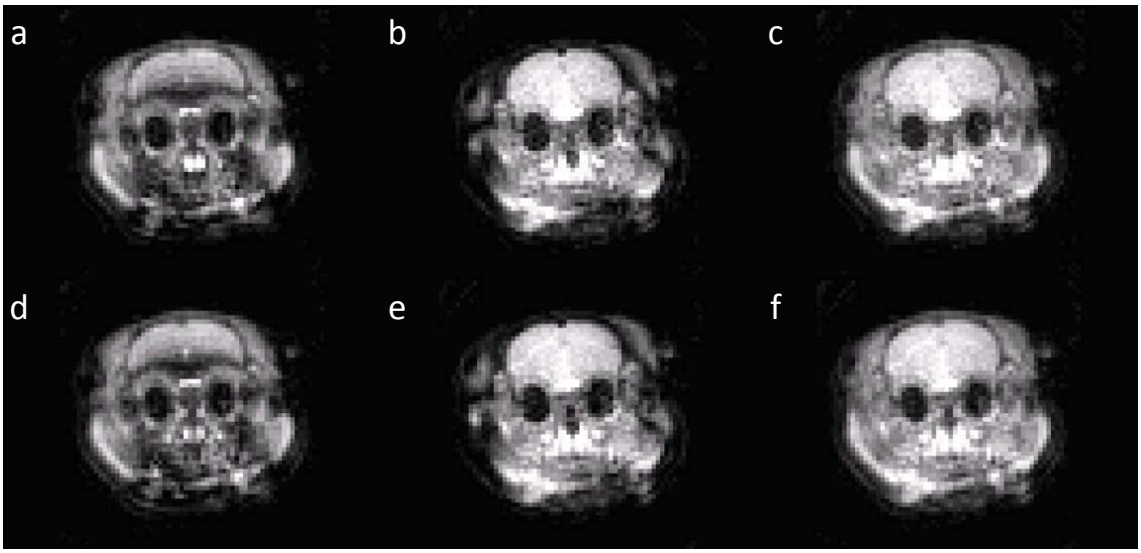

Figure 6.3: Top row: Complementary RF-incremented (0° (a) and 180° (b)) balanced SSFP ($T_R/T_E/\alpha$ = 10 ms/1 ms/30°) coronal images, and MIP combination (c). Bottom row: Complementary RF-incremented (0° (d) and 180° (e)) alternating SSFP ($T_R/T_E/\alpha$ = 10 ms/1 ms/30°) coronal images, and MIP combination (f). All images are of the same slice from the same (representative) animal. The balanced SSFP images were acquired from separate runs of the functional paradigm; the alternating SSFP images were consecutively acquired, separated by 200 ms of RF-catalyzation. Individual balanced SSFP and alternating SSFP images had matched spatial (0.55×0.55×1.5 mm^3) and temporal (1.5 s) resolution.

6.3 Results

Balanced and alternating SSFP raw functional images are shown in Fig. 6.3 (single images; no averaging or combination for either sequence). The 0° and 180° RF phase-cycled balanced SSFP images were obtained from separate runs of the functional paradigm, whereas the alternating SSFP images were acquired consecutively in time (3 s total acquisition time) from a single paradigm run. Alternating SSFP results in comparable image quality and contrast relative to that of balanced SSFP.

In Fig. 6.4, SNR (Fig. 6.4a) and mean z-score (Fig. 6.4b) in stop- and pass-band ROIs is shown for alternating SSFP acquisitions (MIP) at three flip angles. Signal-to-noise ratio significantly decreased with flip angle in both pass- and stop-band ROIs. However, mean z-score in the stop-band ROI trended toward a maximum for α = 45°. Additionally, a significant difference in mean z-score between pass- and stop-band ROIs was observed for α = 30° ($t(5) = 3.0$, $p < 0.05$), but not for higher

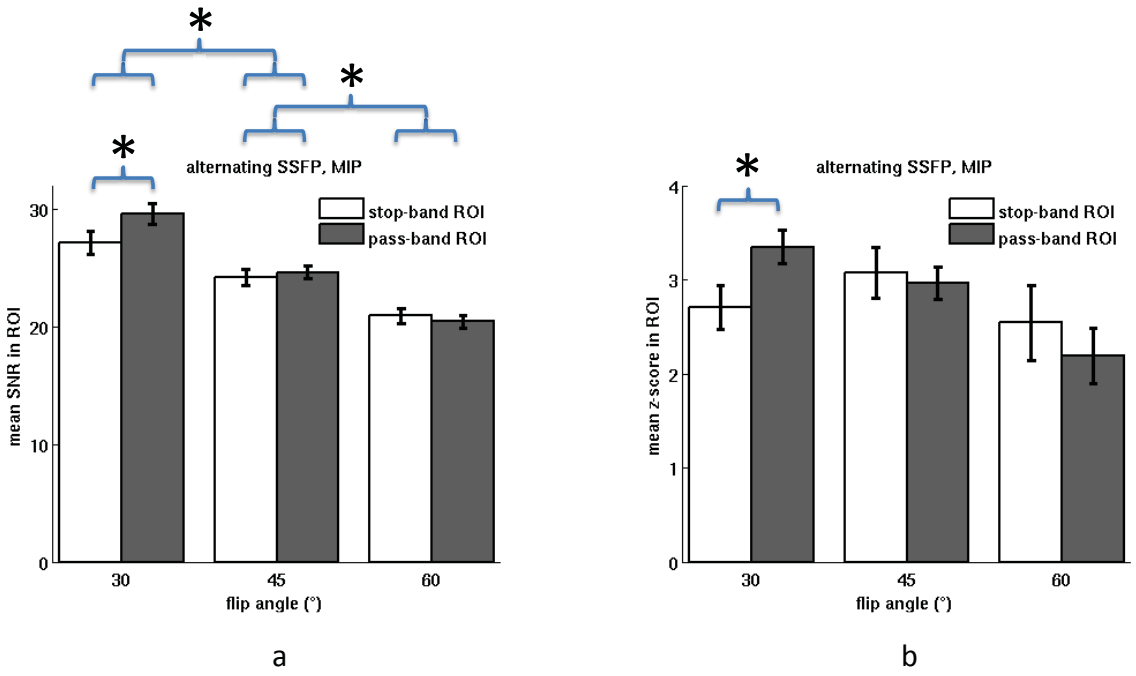

Figure 6.4: Mean SNR (a) and mean z-score (b) in stop- and pass-band ROIs for alternating SSFP (MIP image combination) at three flip angles (α = 30, 45, and 60°). Significant differences ($p < .05$) are indicated with an asterisk.

flip angles. As the goal of alternating SSFP is to provide maximal, uniform BOLD sensitivity across off-resonance frequency (i.e., between pass- and stop-band regions), $\alpha = 45°$ was identified as the optimum flip angle for alternating SSFP, and was used in the remaining figures and comparisons. No significant difference in mean z-scores was observed between MIP and SOS image combination strategies (data not shown).

Balanced and alternating SSFP BOLD functional maps are shown in Fig. 6.5. The 30-40 Hz RMS line-width achieved by performing a whole-brain-voxel shim ($35\times35\times25$ mm^3 voxel) was sufficiently narrow to avoid stop-band artifacts within the brain of most 180° RF phase-cycled (pc-180°) balanced SSFP images. Stop-band artifacts within the brain are visible in balanced SSFP pc-0° images, with concomitant reduced functional sensitivity. Alternating SSFP retains functional sensitivity in the stop-band region, demonstrating a similar activation pattern to that of balanced SSFP pc-180°.

Balanced SSFP pc-0° and alternating SSFP pc-0° (i.e., pre-MIP) raw images with overlaid stop-band ROIs are shown in Fig. 6.6 (top row). Additionally, a balanced

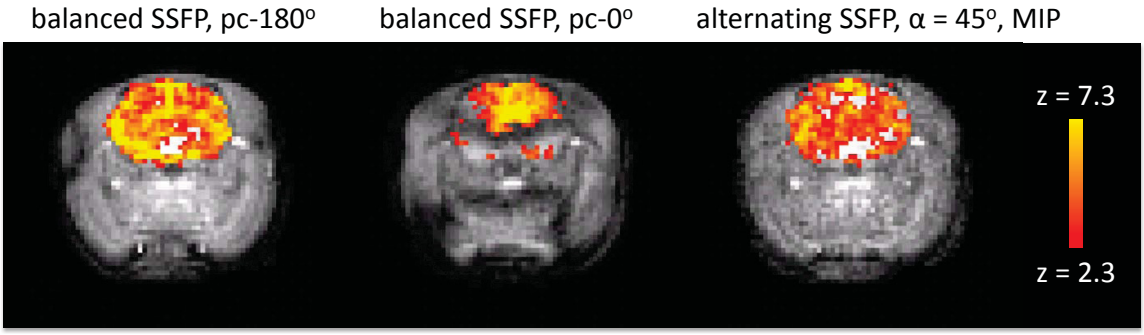

Figure 6.5: BOLD fMRI results (representative animal, coronal slice) for the hypercapnic challenge for balanced SSFP ($\alpha = 30°$, 180° and 0° RF phase-cycled), and alternating SSFP ($\alpha = 45°$, MIP). Z-scores are overlaid on the respective raw functional images. Consecutive balanced SSFP image pairs were averaged prior to fMRI analysis to match temporal resolution with alternating SSFP. This resulted in higher SNR for balanced SSFP raw functional images.

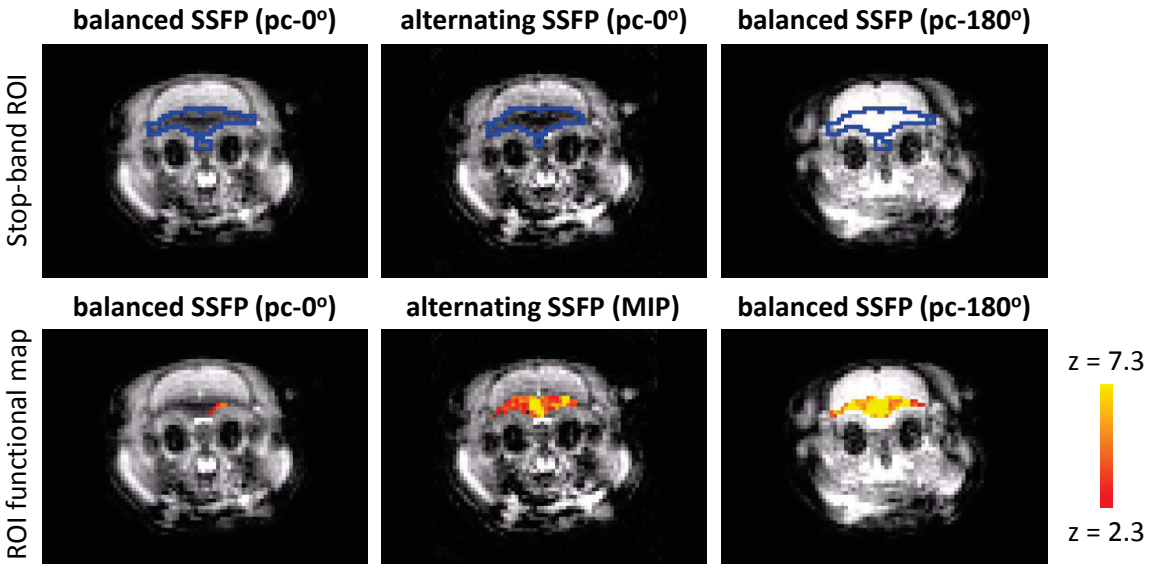

Figure 6.6: Tow row: raw functional images with outlined stop-band ROIs for balanced SSFP (0° RF-phase cycled) and alternating SSFP ($\alpha = 45°$, 0° RF-phase cycled). 180° RF-phase cycled balanced SSFP is also shown, with the balanced SSFP 0° RF-phase cycled stop-band ROI overlaid. Bottom row: fMRI analysis in the ROIs of the top row for balanced SSFP pc-0°, alternating SSFP ($\alpha = 45°$, MIP), and balanced SSFP pc-180°.

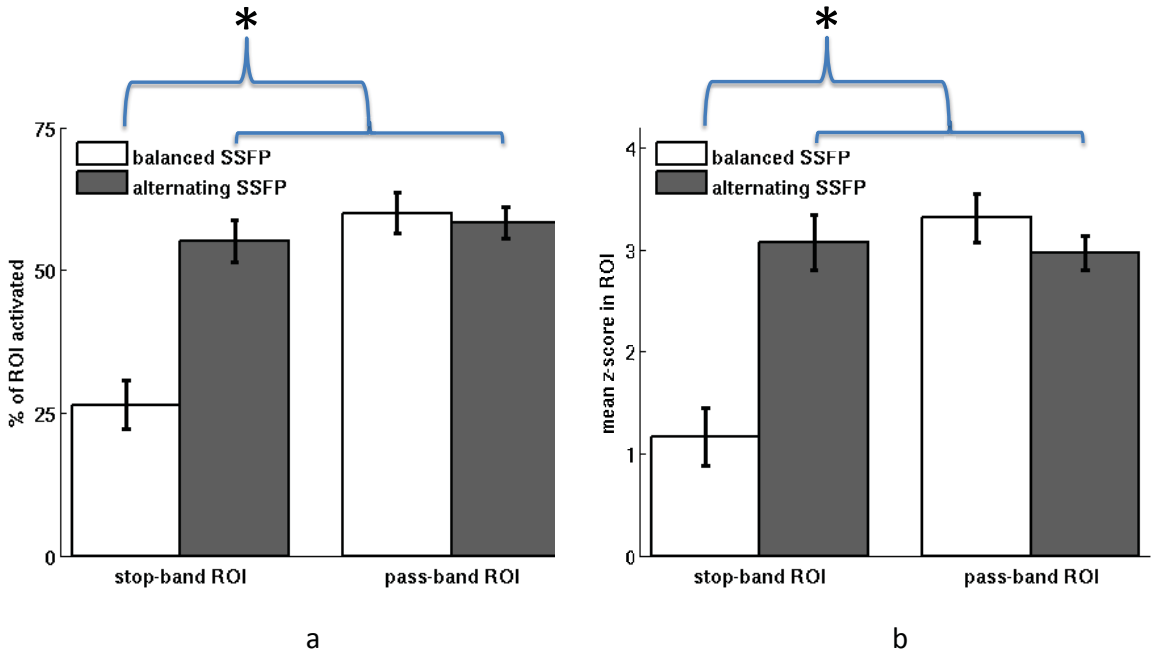

Figure 6.7: Activation extent (a) and mean z-score (b) in pass- and stop-band ROIs for alternating SSFP ($\alpha = 45°$, MIP) and balanced SSFP. Mean and standard error across animals is displayed. Consecutive balanced SSFP image pairs were averaged prior to fMRI analysis to match temporal resolution with alternating SSFP. Significant differences ($p < .05$) are indicated with an asterisk.

SSFP pc-180° raw image is shown with the balanced SSFP pc-0° stop-band ROI overlaid. The enhanced SNR afforded by temporal averaging is apparent in the balanced SSFP images. Despite alternating the RF phase-cycling increment, the stop-band ROIs of balanced pc-0° and alternating SSFP pc-0° are co-localized (Fig. 6.6, top row). BOLD activation maps in the ROIs are shown directly below (Fig. 6.6, bottom row) for balanced SSFP pc-0°, alternating SSFP MIP[4] and balanced SSFP pc-180°. Alternating SSFP recovers BOLD sensitivity in balanced SSFP stop-bands (Fig. 6.6, bottom row). Activation was also recovered by repeating the functional paradigm at a complementary RF phase-cycling increment (pc-180°).

A quantitative comparison of pass- and stop-band activation extent (Fig. 6.7a, Table 6.2) and mean z-score (Fig. 6.7b) was done across animals between alternating SSFP ($\alpha = 45°$, MIP) and balanced SSFP. Alternating SSFP resulted in significantly greater activation extent ($t(5) = 4.4$, $p < 0.01$) and mean z-score ($t(5) = 4.0$, $p <$

[4]i.e., alternating SSFP MIP BOLD activation in the alternating SSFP pc-0° stop-band ROI is overlaid on the alternating SSFP pc-0° raw functional image.

ROI	Sequence	Activation Extent (%)	Mean z-score
pass-band	altSSFP	58 ± 3	3.0 ± 0.2
pass-band	bSSFP	60 ± 4	3.3 ± 0.2
stop-band	altSSFP	55 ± 4	3.1 ± 0.3
stop-band	bSSFP	26 ± 4	1.2 ± 0.3

Table 6.2: Summary statistics for the ROI analysis (mean ± standard error across animals). Consecutive balanced SSFP image pairs were averaged prior to fMRI analysis to match temporal resolution with alternating SSFP.

0.05) compared to balanced SSFP in stop-band ROIs. In pass-band ROIs, there was no significant difference between alternating SSFP and balanced SSFP for either activation extent ($t(5) = 0.4$, $p = 0.7$) or mean z-score ($t(5) = 1.7$, $p = 0.2$). Additionally, alternating SSFP in stop-band ROIs and balanced SSFP in pass-band ROIs were not significantly different in terms of either activation extent ($t(5) = 1.4$, $p = 0.2$) or mean z-score ($t(5) = 1.0$, $p = 0.4$).

6.4 Discussion

Monte Carlo simulations (see Chapter 4) predicted that alternating SSFP could provide whole-brain, banding-artifact-free balanced SSFP fMRI from a single paradigm run, while maintaining the majority of the BOLD sensitivity of conventional balanced SSFP. This work tested this prediction by experimentally comparing the BOLD sensitivity of alternating SSFP with conventional balanced SSFP, for which a hypercapnic challenge in a rat model was used.

6.4.1 Comparison with Monte Carlo Simulations

The goal of alternating SSFP is to provide maximal, uniform BOLD sensitivity across off-resonance frequency (i.e., between pass- and stop-band regions). Monte Carlo simulations (see Fig. 4.5 on page 79) found that using $\alpha = 45°$, while decreasing SNR, increased stop-band BOLD sensitivity and resulted in more uniform BOLD sensitivity across off-resonance frequency. Experimental results are consistent with these findings. Increasing the flip angle beyond 30° was found to reduce SNR (Fig. 6.4a), however, stop-band BOLD sensitivity trended toward a maximum at $\alpha = 45°$ (Fig. 6.4b).

Additionally, significant differences in mean z-score between pass- and stop-band regions were only observed at low flip angle (Fig. 6.4b).

6.4.2 Alternating SSFP vs. balanced SSFP

We found the stop- and pass-band ROIs of balanced and alternating SSFP images (with matched RF phase-cycling increment) to be co-localized (Fig. 6.6, top row). This suggests that, despite alternating the RF phase-cycling increment every 1.5 s, a steady state similar to that of balanced SSFP was attained with alternating SSFP. Combining the consecutively acquired (complementary RF phase-cycled) alternating SSFP images was found to eliminate banding artifacts (Fig. 6.3), resulting in pass-band contrast across the entire off-resonance frequency spectrum.

We found that alternating SSFP resulted in similar functional contrast to that of balanced SSFP in the pass-band, across the entire off-resonance frequency spectrum (Fig. 6.7, Table 6.2). No significant difference in activation extent or mean z-score was found between balanced SSFP in the pass-band and alternating SSFP in the pass- or stop-band. Additionally, alternating SSFP resulted in significantly greater activation extent and mean z-score compared to balanced SSFP in the stop-band.

Figure 6.5 suggests significantly reduced z-scores for alternating SSFP compared to balanced SSFP in the pass-band, however, we did not observe this to be the case across animals (Fig. 6.7, Table 6.2). We found the relative sensitivity estimates for alternating and balanced SSFP to depend on analysis method. When only active ($z > 2.3$) voxels were considered (i.e., those displayed in fMRI activation maps), alternating SSFP had significantly reduced sensitivity (approximately 15 % less) compared to balanced SSFP in the pass-band. However, when all voxels (not just those above threshold) were considered (as was the case for all of the analysis presented in the results section of this paper), no significant difference between alternating SSFP and balanced SSFP in the pass-band was observed.

We believe that considering all voxels is best, as considering only supra-threshold voxels can result in biased comparisons. As an example, consider two sequences, A and B, which result in z-scores of 2.4 and 2.2 throughout the brain, respectively. An analysis considering only supra-threshold ($z > 2.3$) voxels would indicate a 100 % reduction in sensitivity by choosing sequence B instead of A, whereas an analysis

considering all voxels would indicate an 8 % reduction. Of course, if a large population of truly inactive voxels exists, including all voxels in an analysis will reduce the apparent difference in sensitivity between sequences. We obtained mean z-scores of 3.0 or greater (Table 6.2) across all voxels, however, and therefore do not suspect this to be the case.

6.4.3 Conclusion

This work demonstrates that alternating SSFP can provide whole-brain, banding-artifact-free pass-band SSFP fMRI in a rat model, without requiring a repeat run of the functional paradigm. Alternating SSFP may provide a practical alternative to GRE-EPI for whole-brain functional imaging applications limited by signal dropout in humans.

Chapter 7

Human Studies

7.1 Introduction

In chapter 6 the high BOLD CNR afforded by rat fMRI was used to demonstrate the efficacy of alternating SSFP for BOLD fMRI, and optimize acquisition/reconstruction parameters. In this chapter, experiments were conducted to demonstrate the efficacy of alternating SSFP for measuring stimulus-evoked BOLD signal changes in humans.

Human fMRI is more difficult than rat fMRI. Shorter paradigms, subject motion, and reduced task-compliance all conspire to reduce BOLD CNR. Additionally, we wish to demonstrate the ability to detect stimulus-evoked BOLD signal changes, which permit mapping of brain function. However, this further reduces BOLD CNR because the stimulus-evoked BOLD response is weaker than that from hypercapnia [78].

We hypothesize that alternating SSFP will result in uniform BOLD sensitivity across off-resonance frequency (i.e., in balanced SSFP pass- and stop-bands). This is critical for whole-brain applications, as the strong magnetic field inhomogeneities in the orbitofrontal and inferior temporal cortex prevent whole-brain coverage with a single pass-band. To test our hypothesis, however, we want to use a robust task that results in BOLD activation in a magnetically-homogeneous region. This allows for the deliberate placement of a stop-band within the active ROI to unambiguously determine if alternating SSFP recovers BOLD sensitivity from balanced SSFP stop-bands. Conversely, the active ROI can be entirely contained in the balanced SSFP pass-band, by inverting the RF phase cycling increment, to determine if alternating SSFP maintains BOLD sensitivity in balanced SSFP pass-bands. Thus we validate alternating SSFP's ability to recover stop-band BOLD sensitivity, and maintain pass-band BOLD sensitivity, in visual cortex using a checkerboard task.

7.2 Methods

7.2.1 Data Acquisition

Eight healthy adult volunteers were scanned under a research protocol approved by the Capital District Health Authority Research Ethics Board. Each participant provided written, informed consent prior to participation and received compensation for participating. Data was acquired on a 4 T MRI system consisting of a superconducting magnet (Oxford Instruments), body gradient coil (Tesla Engineering Ltd.), transverse electromagnetic (TEM) head coil for transmit/receive (Bioengineering Inc.), and a Varian/Agilent DirectDrive console. Maximum gradient amplitude and slew rate were limited to 35.5 mT/m and 140 T/m/s, respectively.

All studies used a block design visual stimulation paradigm consisting of 20 s of visual stimulation alternated with 20 s of rest. The task began and ended with a rest block and had a total duration of 5 min. E-Prime (Psychology Software Tools, Inc.) was used to present stimuli, which were projected onto a screen mounted inside the magnet bore, and viewed through a mirror mounted on the head coil. A black/white annular checkerboard pattern reversing at 8 Hz was used for visual stimulation. Rest blocks consisted of a grey background. A red cross fixation point was present in both stimulation and rest blocks. In an effort to enhance subject focus, the red cross turned green for one second at random (on average once every ten seconds), and subjects were instructed to press a button on a response pad when this occurred.

Each subject completed four repetitions of the 5 min visual stimulation paradigm to compare alternating SSFP, balanced SSFP (180°-RF-phase-cycled (pc180)), balanced SSFP (0°-RF-phase-cycled (pc0)), and GRE. Scan order was counter-balanced across subjects. A pc0 balanced SSFP pre-scan was used to adjust the balanced SSFP centre frequency to place a stop-band in the visual cortex. This also ensures the visual cortex is approximately centered in the pass-band of pc180 scans. This centre frequency was then used for all alternating and balanced SSFP acquisitions.

Alternating SSFP consisted of a timecourse of interleaved pc180 and pc0 balanced SSFP image volume acquisitions. Each alternating SSFP image volume acquisition began with linear-ramp RF catalyzation (20 pulses), and ended with a 90°-$\alpha/2$ flip-down RF pulse and gradient spoiling, to reduce signal oscillations associated with

changing the RF phase cycling increment. Balanced SSFP consisted of a timecourse of image volume acquisitions from an uninterrupted steady state at a constant (180° or 0°) RF-phase-cycling increment. Twenty "dummy" T_R cycles, during which steady state was maintained but no data was acquired, were inserted at the beginning of each balanced SSFP image volume to match the image acquisition rate to alternating SSFP. All SSFP variants used 3D interleaved stack-of-spiral-out **k**-space trajectories (phase-encoding in the z-dimension) with the following acquisition parameters: $T_R = 10.1$ ms, $T_E = 0.7$ ms, 8 interleaved spirals, 240x240x80 mm^3 field of view, 64x64x16 matrix, 1.5 s per RF-phase-cycled image volume. A 30° flip angle was used for balanced SSFP acquisitions, which is approximately the signal-optimizing flip angle for grey matter at 4 T. A 45° flip angle was used for alternating SSFP acquisitions, which is predicted to maximize alternating SSFP BOLD sensitivity at 4 T (see Chapter 4).

GRE was implemented as a 2D sequence (slice selection in the z-dimension) with interleaved spiral-out acquisition in plane: $T_R = 1000$ ms, $T_E = 15$ ms, 2 interleaved spirals, 240x240 mm^2 field of view, sixteen 5 mm slices, flip angle = 60°. For registration purposes, a single, whole-brain functional image volume was acquired prior to each functional run, using the same pulse sequence as the corresponding functional run, but having twice the number of slices. Following the four functional runs a 3D magnetization prepared fast low angle shot T_1-weighted anatomic image was acquired for each subject ($T_R = 11$ ms, $T_E = 5$ ms, inversion time = 500 ms, flip angle = 11°, 256×256×64 matrix, 240×240×192 mm^3 field of view, 5 min 25 s scan-time).

7.2.2 Data Analysis

Prior to fMRI analysis, a banding-artifact-free alternating SSFP image timecourse was created by maximum intensity projection (MIP) of consecutively acquired pc0 and pc180 image volumes. Separate pc0 and pc180 alternating SSFP image timecourses, created by discarding every second image volume, were also analyzed. A temporally downsampled pc180 balanced SSFP image timecourse was also created in this manner. This data set was compared with the pc180 alternating SSFP image timecourse, to determine the effect of alternating between steady states on BOLD sensitivity, on a per-image basis. Note that this analysis is intended to gain a better understanding of alternating SSFP BOLD sensitivity, and not to recommend one approach over

another. The intended application of alternating SSFP - fMRI in which the entire ROI cannot be contained within a single pass-band - is distinct from balanced SSFP; they are complementary approaches.

Data were analyzed using the FSL software package [71]. Pre-processing steps included high pass-filtering (40 s high-pass filter cutoff), spatial smoothing (6 mm FWHM), and within-run motion correction (GRE data only). SSFP data were not motion-corrected to avoid aligning fluctuating SSFP bands [7]. All raw data sets were visually inspected to ensure that motion was minimal. fMRI analysis was done using the fMRI expert analysis tool (FEAT, v6.00). Activation was modeled as a boxcar function, representing the task, convolved with the double-gamma HRF. Temporal derivative terms were included in the model to allow for small variations in response onset and offset between brain regions and subjects.

The four functional runs acquired from each subject were co-registered using FLIRT [77] (rigid body alignment, 6 degrees of freedom). This was done using a two-step procedure: 1) the first image in each functional run was registered to the corresponding whole-brain functional image volume, and 2) the whole-brain functional image volumes were registered to the first whole-brain functional image volume. These registration steps were then concatenated into a single transformation and used to co-register all functional image volumes.

Occipital Lobe ROI Analysis

For each subject, alternating and balanced SSFP fMRI data sets were compared in an ROI created from the GRE fMRI data set. This ROI was created by choosing the largest cluster from the cluster-thresholded ($z > 5.0$, $p < .05$) GRE fMRI data set (Fig. 7.1). This cluster was localized to the occipital lobe and contained 86-98 % (range across subjects) of the total number of active voxels. Smaller clusters, which were not localized to the occipital lobe, were excluded from the ROI. The mean z-score and activation extent (percentage of voxels having $z > 2.3$) were compared between alternating SSFP and balanced SSFP in this ROI. This analysis was also carried out at the group level in the same manner.

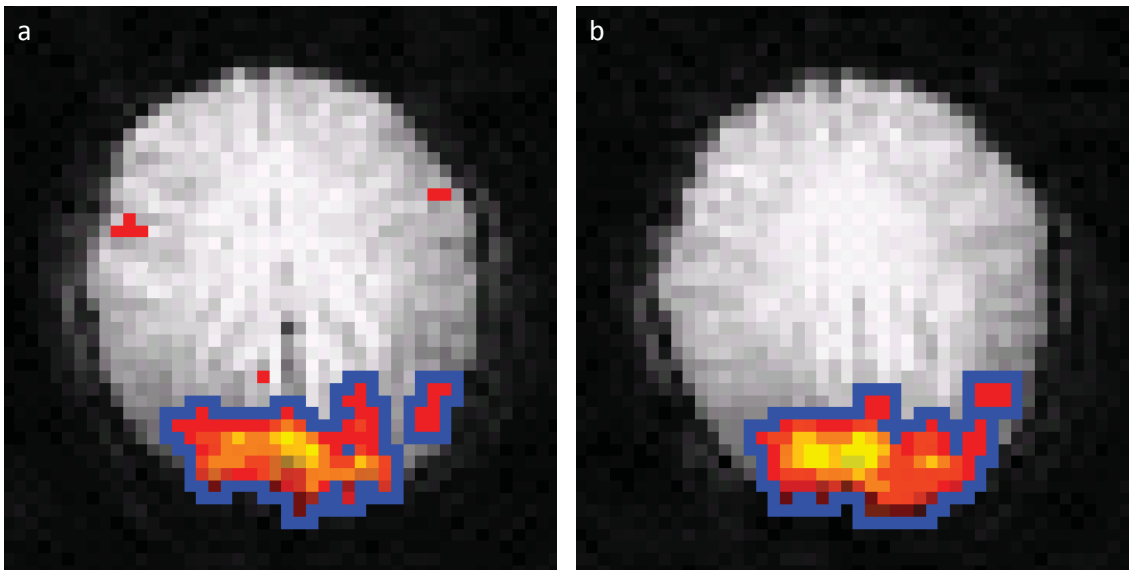

Figure 7.1: Occipital ROI definition. The occipital ROI was identified as the largest activation cluster from the cluster-thresholded ($z > 5.0$, $p < .05$) GRE fMRI data set. Shown are GRE functional images (representative subject; two adjacent slices) with overlaid activation map (red-yellow) and occipital ROI (outlined in blue). Slice (a) contains three active regions that were not included in the ROI (red pixels not outlined in blue).

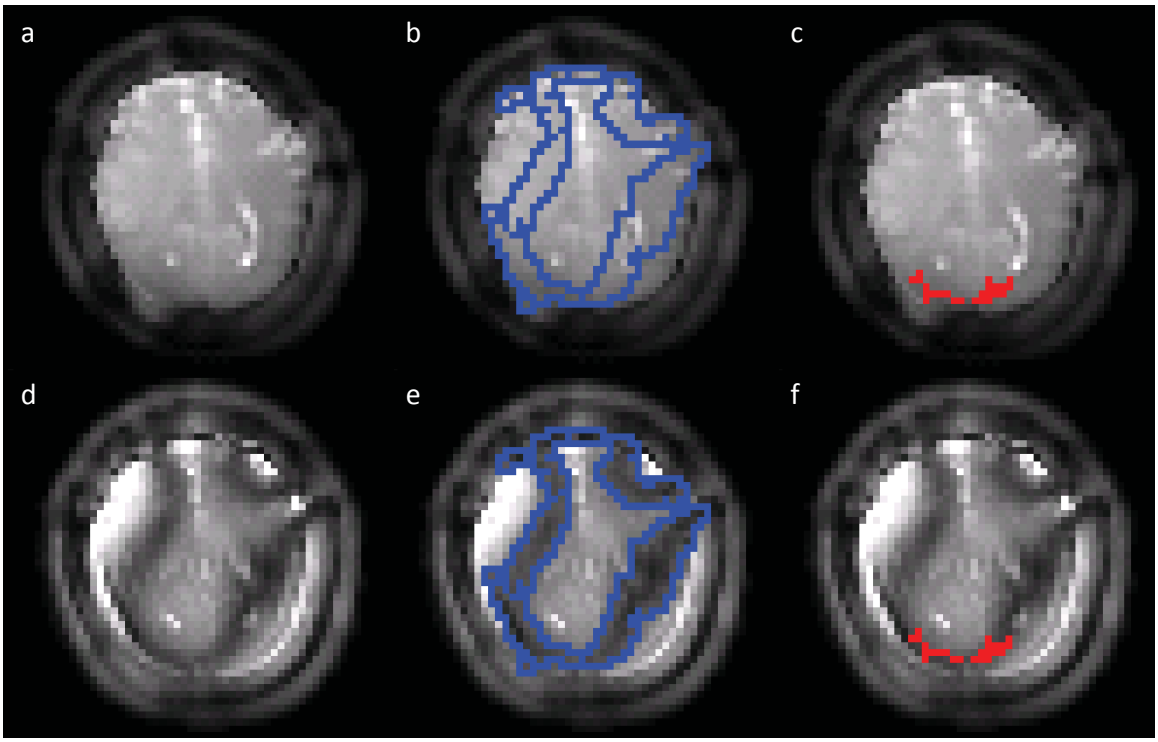

Figure 7.2: Stop-band ROI identification (representative subject). Note that all SSFP images exhibited a fat chemical shift artifact in the form of a "halo" circling the brain, as no fat suppression was used. (a, d) co-registered balanced SSFP mean functional images (a: pc180, d: pc0). (e) stop-bands (outlined in blue) were identified as regions having low signal in (d) but not in (a). (b) stop-band ROI overlaid on the pc180 scan. (c, f) stop-band ROI analysis was restricted to the region of overlap between the stop-band ROI and the occipital ROI (shaded in red).

Stop-band ROI Analysis

The SSFP centre frequency was set to deliberately place a stop-band in the visual cortex during pc0 acquisitions. This was done to determine if alternating SSFP was capable of recovering BOLD sensitivity from stop-bands.

Stop-band ROIs were identified as regions of low signal intensity in pc0 acquisitions that were not regions of low signal intensity in pc180 acquisitions, using the algorithm illustrated in Fig. 6.2 on page 97. Stop-band ROIs are simultaneously centre-of-pass-band ROIs for the opposite (pc180) acquisition.

Balanced SSFP stop-band ROIs were identified from the mean functional images (time average of functional image volumes) of the pc0 and pc180 timecourses (Fig. 7.2). It was possible to determine stop-band location from the mean functional

images because stop-band signal fluctuations were about a fixed point in space (no drift). Alternating SSFP stop-band ROIs were identified from the mean functional images of the separated pc0 and pc180 alternating SSFP timecourses. Stop-band ROI analysis was restricted to voxels that were contained in both the occipital ROI and the stop-band ROI (Fig. 7.2c, f).

7.3 Results

7.3.1 Individual- and Group-level Activation Maps

Activity was detected in the occipital lobe for all subjects and sequences (Fig. 7.3). In two subjects no activity was detected upon analyzing the pc0 alternating SSFP image timecourse separately. Because the visual cortex was easily contained in a single pass-band: 1) the alternating SSFP activation map from MIP image combination of both RF-phase-cycled images (Fig. 7.3g) was very similar to that from analyzing the pc180 image timecourse separately (Fig. 7.3f), and 2) reduced activation was observed for pc0 scans (Fig. 7.3a, e).

Robust activation was observed at the group level (Fig. 7.4) for all pc180 SSFP scans and for GRE. pc0 data sets were not analyzed at the group level as stop-band location varied between subjects.

7.3.2 Alternating SSFP vs. balanced SSFP in the Occipital ROI

To compare alternating SSFP (pc180) and balanced SSFP (pc180) at matched temporal resolution, isolating the effect on BOLD sensitivity of alternating the RF-phase-cycling increment, a temporally down-sampled balanced SSFP pc180 image timecourse was generated by discarding every second image volume. This reduced the mean z-score in the occipital ROI by a factor of approximately $\sqrt{2}$ at both the individual and group levels (tables 7.1 and 7.2, respectively, bal-pc180 vs. bal-pc180-half).

At the individual-level, the mean z-score and activation extent from alternating SSFP (pc180) were, on average, 83 % and 82 % of that from balanced SSFP (pc180) at matched temporal resolution (i.e., with half of the balanced SSFP data discarded)

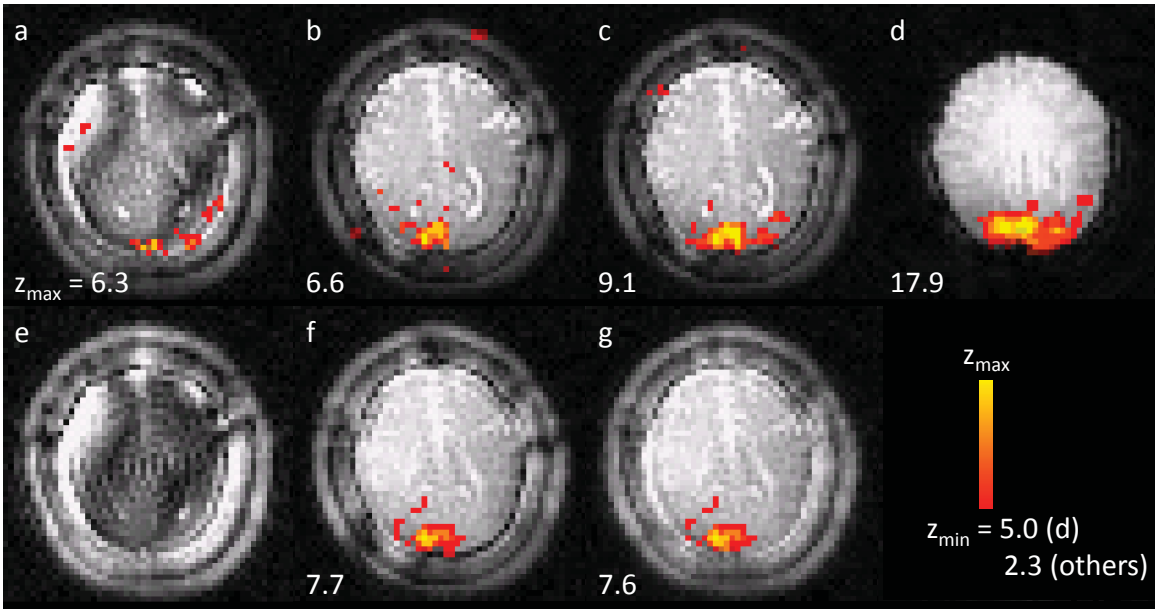

Figure 7.3: Cluster-thresholded ($p < .05$) activation maps from visual stimulation at 4 T overlaid on corresponding raw functional images (representative subject). A z-statistic threshold of 2.3 was used to identify clusters for all sequences except GRE (d) which used 5.0 due to large activation extent. Note that no ROI restriction has been applied to these maps. Maps are shown for: a) b-SSFP (pc0), b) b-SSFP (pc180) with half of the data discarded to match the temporal resolution to (f) (this was done to compare the BOLD sensitivity of the alternating SSFP pc180 pseudo steady state to the fully established balanced SSFP pc180 steady state), c) b-SSFP (pc180) (i.e., not downsampled), d) GRE, e) alternating SSFP (analysis of pc0 image timecourse), f) alternating SSFP (analysis of pc180 image timecourse), and g) alternating SSFP (analysis of MIP image combination timecourse). The top of the color scale (z_{max}) is shown at the bottom left corner of the corresponding image. GRE scans were used to identify active brain regions, in which balanced and alternating SSFP were compared. These results are not intended as a comparison of the relative BOLD sensitivities of SSFP and GRE scans, however, as SSFP scans were not optimized for comparison with GRE (see discussion).

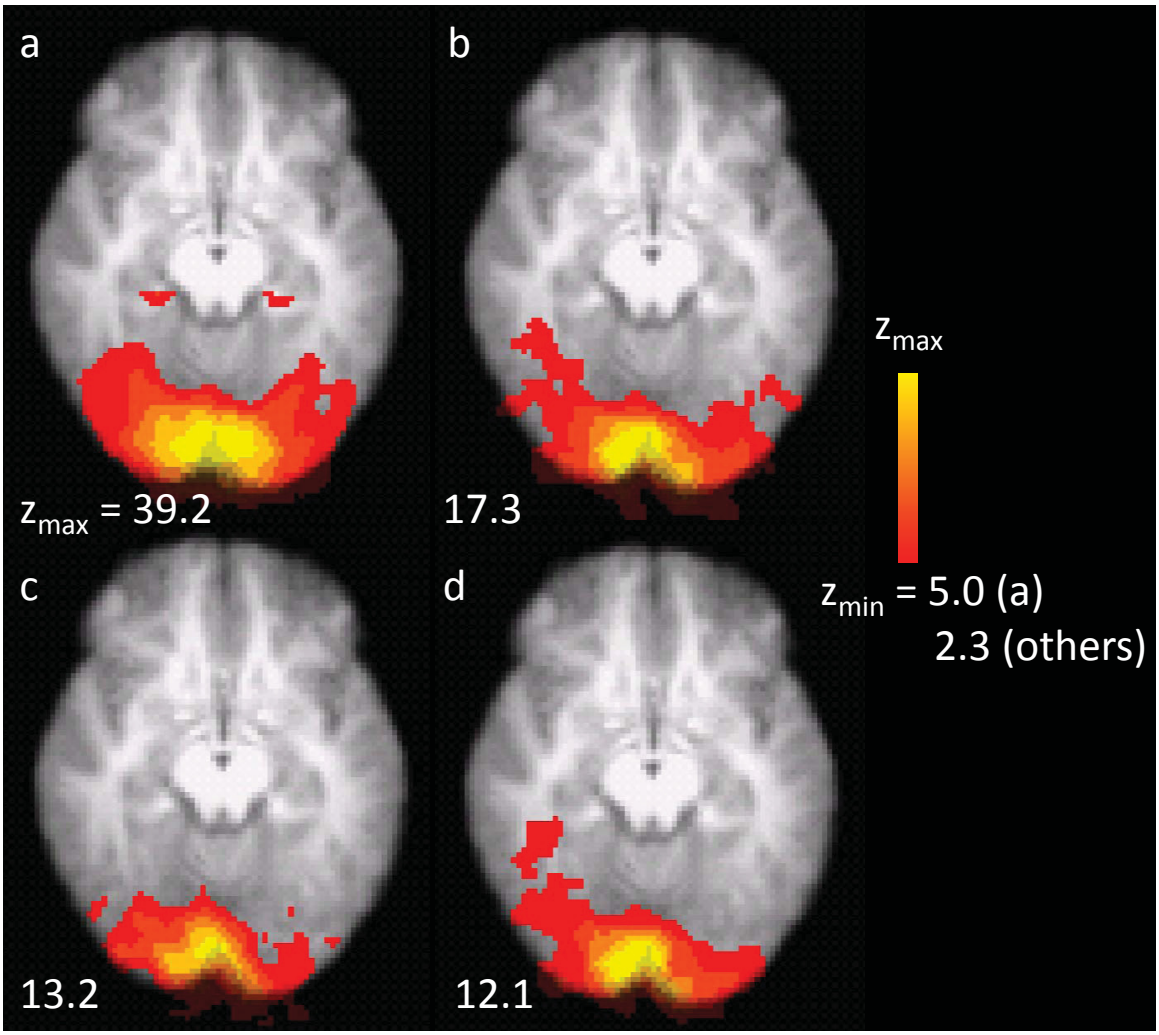

Figure 7.4: Cluster-thresholded ($p < .05$) group-level activation maps from visual stimulation at 4 T overlaid on the MNI 152 standard brain. A z-statistic threshold of 2.3 was used to identify clusters for all sequences except GRE (a) which used 5.0 due to large activation extent. Note that no ROI restriction has been applied to these maps. Maps are shown for: a) GRE, b) balanced SSFP (pc180), c) alternating SSFP (analysis of pc180 image timecourse), and d) balanced SSFP (pc180) with one-half of the data discarded to match the temporal resolution to (c). The group-level activation map for alternating SSFP using MIP image combination of both RF-phase-cycled images is very similar to (c), as the entire visual cortex was contained in the pass-band of pc180 acquisitions, and is not shown. The top of the color scale (z_{max}) is shown at the bottom left corner of the corresponding image. GRE scans were used to identify active brain regions, in which balanced and alternating SSFP were compared. These results are not intended as a comparison of the relative BOLD sensitivities of SSFP and GRE scans, however, as SSFP scans were not optimized for comparison with GRE (see discussion).

Sequence	z-score	Extent (%)
alt-pc180	1.5 ± 0.1	28 ± 3
bal-pc180	2.6 ± 0.2	50 ± 3
bal-pc180-half	1.8 ± 0.1	35 ± 2
alt-pc180/bal-pc180-half (%)	83 ± 6	82 ± 8

Table 7.1: Summary statistics for the individual-level occipital ROI analysis. The occipital ROI contained 670 ± 30 voxels. Mean z-score (unthresholded) and activation extent (the percentage of voxels having $z > 2.3$) were computed in the occipital ROI for: alternating SSFP (analysis of pc180 image timecourse) (alt-pc180), pc180 balanced SSFP (bal-pc180), and pc180 balanced SSFP with one-half of the data discarded to match the temporal resolution to alt-pc180 (bal-pc180-half). The ratio of alt-pc180 to bal-pc180-half was computed for each metric for each subject (bottom row). This ratio was computed to compare the BOLD sensitivity of the alternating SSFP pseudo steady state to the fully established steady state, and not to recommend one technique over the other - the intended applications of alternating and balanced SSFP are distinct. Values reported in this table are mean ± standard error across subjects.

(table 7.1, alt-pc180/bal-pc180-half). At the group-level, the mean z-score and activation extent from alternating SSFP (pc180) were both 84 % of that from balanced SSFP (pc180) at matched temporal resolution (table 7.2, alt-pc180/bal-pc180-half).

7.3.3 Alternating SSFP vs. balanced SSFP in the Stop-band ROI

Alternating and balanced SSFP were compared in stop-band ROIs (for pc0 scans) which are simultaneously centre-of-pass-band ROIs (for pc180 scans) (table 7.3). Significantly ($p < .05$) reduced z-scores and activation extent were observed in the stop-band, compared to the pass-band-centre, for alternating SSFP (table 7.3, alt-pc0 vs. alt-pc180) and balanced SSFP (table 7.3, bal-pc0 vs. bal-pc180). Despite having one-half of the temporal resolution, alternating SSFP (analysis of pc180 image timecourse) resulted in significantly ($p < .05$) greater z-scores and activation extent compared to balanced SSFP (pc0).

Although the entire visual cortex is easily covered in a single pass-band, banding artifacts were observed in the frontal and inferior temporal lobes with pc180 balanced SSFP, which were eliminated with alternating SSFP MIP (Fig. 7.5).

Sequence	z-score	Extent (%)
alt-pc180	3.1	54
bal-pc180	5.2	75
bal-pc180-half	3.6	64
alt-pc180/pc180half (%)	84	84

Table 7.2: Summary statistics for the group-level occipital ROI analysis. The occipital ROI contained 18608 voxels. Mean z-score (unthresholded) and activation extent (the percentage of voxels having $z > 2.3$) were computed in the occipital ROI for: alternating SSFP (analysis of pc180 image timecourse) (alt-pc180), pc180 balanced SSFP (bal-pc180), and pc180 balanced SSFP with one-half of the data discarded to match the temporal resolution to alt-pc180 (bal-pc180-half). The ratio of alt-pc180 to bal-pc180-half was computed for each metric (bottom row). This ratio was computed to compare the BOLD sensitivity of the alternating SSFP pseudo steady state to the fully established steady state, and not to recommend one technique over the other - the intended applications of alternating and balanced SSFP are distinct.

7.4 Discussion

The goal of this study was to demonstrate the ability of alternating SSFP to detect stimulus-evoked BOLD signal changes in humans, and to compare the BOLD sensitivity of alternating SSFP to conventional balanced SSFP in pass- and stop-band regions. The visual cortex is ideally suited for this purpose, because of its robust BOLD response combined with its magnetic field homogeneity, which allows the experimenter to carefully position the stop-band. It should be noted, however, that one would not choose alternating SSFP to study the visual cortex, because it can be entirely contained within a single pass-band. In such cases using alternating rather than balanced SSFP needlessly reduces BOLD sensitivity (i.e., by reducing the temporal resolution by a factor of two, as well as reducing BOLD sensitivity, per image, by about 20 %). Rather, alternating SSFP is designed for imaging applications in which the entire ROI cannot be contained within a single pass-band (e.g., whole-brain applications).

In this study, we used a 2D GRE sequence to identify active brain regions, in which 3D alternating and balanced SSFP sequences were compared. We have avoided, however, making comparisons between GRE and SSFP sequences. We feel that our SSFP acquisitions must be optimized before a meaningful comparison can be made. In particular, eddy-current-induced artifacts limited the SSFP data acquisition duty

Sequence	z-score	Extent (%)
alt-pc0	0.4 ± 0.2	9 ± 4
alt-pc180	1.7 ± 0.2	32 ± 4
bal-pc0	0.7 ± 0.3	20 ± 5
bal-pc180	2.2 ± 0.3	43 ± 6

Table 7.3: Summary statistics for the stop-band ROI analysis. The overlap between the balanced SSFP stop-band ROI and the occipital ROI was 190 ± 30 voxels. The overlap between the alternating SSFP stop-band ROI and the occipital ROI was 260 ± 30 voxels. Mean z-score (unthresholded) and activation extent (the percentage of voxels having $z > 2.3$) were computed in the region of overlap between the stop-band ROI and the occipital ROI for: alternating SSFP (analysis of pc0 image timecourse) (alt-pc0), alternating SSFP (analysis of pc180 image timecourse) (alt-pc180), balanced SSFP (pc0) (bal-pc0), and balanced SSFP (pc180) (bal-pc180). Values reported in this table are mean $\pm$ standard error across subjects.

cycle (the fraction of the T_R cycle during which imaging gradients are applied) to one-half of its potential value. Eddy currents are more detrimental to 3D sequences, such as SSFP, where they perturb the steady state magnetization, than 2D sequences, such as GRE, where transverse magnetization is not preserved between T_R cycles. Additionally, fat chemical shift artifacts likely reduced the temporal SNR of SSFP scans. Fat chemical shift artifacts are more prominent in SSFP than GRE because the T_2/T_1 contrast of SSFP scans produces hyper-intense fat signal. We feel that steps to minimize eddy currents and suppress fat signal should be incorporated into our SSFP sequences before a quantitative comparison with GRE is made. Suggested approaches for doing so are discussed in chapter 8. Note that all SSFP sequences used the same imaging gradient trajectory and no fat suppression, and should therefore be subject to the same eddy currents and fat chemical shift artifacts.

For alternating SSFP to be worthwhile it must significantly recover BOLD sensitivity from balanced SSFP stop-bands, despite having one-half of the temporal resolution (i.e., after MIP image combination of alternating SSFP image pairs to eliminate stop-bands, the temporal resolution of alternating SSFP is one-half that of balanced SSFP). We found this to be the case; alternating SSFP resulted in significantly ($p < .05$) higher z-scores and activation extent in stop-band ROIs vs. balanced SSFP (table 7.3, alt-pc180 vs. bal-pc0). One alternating SSFP pass-band has more

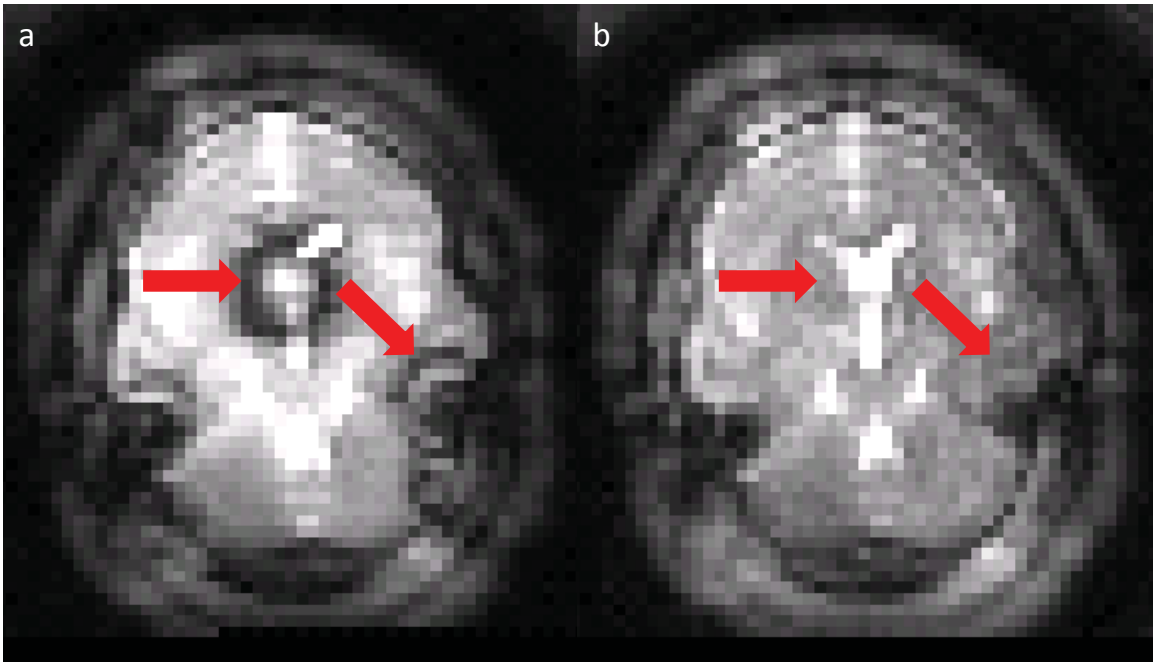

Figure 7.5: Elimination of stop-bands with alternating SSFP. An inferior slice from the functional image volume is shown for: a) balanced SSFP (pc180), and b) alternating SSFP (MIP image combination). The red arrows highlight stop-bands in balanced SSFP that are absent in alternating SSFP.

BOLD sensitivity than two balanced SSFP stop-bands; alternating SSFP is worthwhile.

Of course, stop-band BOLD sensitivity can be recovered with balanced SSFP by acquiring at a complementary RF-phase-cycling increment (table 7.3, bal-pc180 vs. bal-pc0), but this requires a repeat run of the functional paradigm, resulting in an effective temporal resolution on the order of minutes. This is prohibitively slow for the majority of investigations into brain function in psychology and neuroscience.

We found larger stop-band ROIs for alternating SSFP (260 ± 30 voxels) compared to balanced SSFP (190 ± 30 voxels). Alternating SSFP acquisitions used a higher flip angle (45°) than balanced SSFP acquisitions (30°) and this is consistent with the broadening of the SSFP stop-band with increased flip angle.[1]

Our results are in agreement with previous Monte Carlo simulations (chapter 4) suggesting that alternating SSFP maintains the majority of BOLD sensitivity of pass-band SSFP, per image. Our results differ from a rat hypercapnia study (chapter 6)

[1]This can be observed in Fig. 4.3 on page 76 where the width of the low-signal region centered at $\Delta\omega = 0$ ($1.5\text{ s} < t < 3.0\text{ s}$) increases with flip angle (b-d).

that reported no sensitivity reduction for alternating SSFP relative to pass-band SSFP. The reason for this discrepancy is unclear.

7.4.1 Conclusion

In conclusion, alternating SSFP permits the consecutive acquisition of 0°- and 180°-RF-phase-cycled balanced SSFP images, with the pass-band of each image having 80 % of the BOLD sensitivity found in full steady state (conventional balanced SSFP). These images can then be combined to produce whole-brain, banding-artifact-free balanced SSFP fMRI from a single paradigm run, with a temporal resolution comparable to that of GRE-EPI.

Alternating SSFP may allow fMRI in SFG regions not possible with GRE acquisitions due to signal dropout. However, we found reduced BOLD sensitivity for alternating SSFP compared to GRE. Nevertheless, alternating SSFP should employ eddy current mitigation and fat suppression before a quantitative comparison with GRE is made. Future work is needed to determine if alternating SSFP performs better than spin-echo methods (in terms of BOLD sensitivity or image distortion), which also eliminate GRE signal dropout at the expense of BOLD sensitivity.

Chapter 8

Future Work and Conclusion

8.1 Future Work

8.1.1 Suppression of Fat Signal

4 T human SSFP images exhibited a fat chemical shift artifact in the form of a "halo" surrounding the brain (Fig. 7.3). This is sub-optimal, as displaced fat signal makes image registration difficult. Going forward, some type of fat suppression should be incorporated into the alternating SSFP pulse sequence.

Perhaps the most common fat-suppression technique is the selective excitation and gradient-spoiling of the fat signal, prior to exciting and gradient-encoding the unperturbed water signal. Suppression of fat signal is more difficult with SSFP sequences, however, because of the zero-gradient-area requirement. Nonetheless, fat saturation in this form has been successfully incorporated into a continuously running 3D SSFP sequence [56]. This was achieved by periodically interrupting the balanced SSFP RF train with an $\alpha/2$ flip-back pulse, to store the steady state magnetization along the z-axis. Conventional selective excitation/gradient-spoiling fat saturation was then applied, after which an $\alpha/2$ flip-down pulse was used to recall the steady state magnetization. This method may be compatible with alternating SSFP. It should first be verified, however, that this method does not round the alternating SSFP BOLD contrast vs. off-resonance frequency profile, as $\alpha/2$ flip-down/back pulses are less effective for off-resonant spins.

Selective excitation of only the water signal has also been demonstrated for balanced SSFP [79]. This was a achieved using a 3.6 ms spatial-spectral RF pulse, combining both spatial and spectral selectivity. Spatial-spectral pulses may be particularly compatible with alternating SSFP. One of the main drawbacks of spatial-spectral RF pulses for conventional balanced SSFP is that they have a relatively long duration, which increases the minimum T_R. Using a longer T_R can introduce

banding artifacts into an otherwise banding-artifact-free region of interest. This is not a problem for alternating SSFP, as banding artifacts are corrected with image combination.

8.1.2 Eddy-current reduction with segmented EPI

We found the readout duty cycle of SSFP acquisitions at 4 T to be limited by eddy-current-induced image artifacts. Eddy currents are electric currents induced in the conducting parts of the MRI system by the changing magnetic fields produced by the gradient coil. Eddy currents create undesirable magnetic fields that modify the B_0 field, causing image artifacts.

All 4 T SSFP acquisitions in this work used 8 spiral interleaves to cover a 64×64 matrix. This matrix could have been covered with 4 spiral interleaves, without changing the T_R (i.e., doubling the image acquisition rate or doubling the number of slices acquired per unit time), were it not for eddy currents (Fig. 8.1). Eddy currents that varied from one T_R cycle to the next were found to be particularly problematic. These disturb the steady state because they cause spin isochromats to precess through a different angle each T_R. Conversely, steady state can be maintained in the presence of a consistent eddy current.

Similar gradient trajectories result in similar eddy currents. Going forward, segmented EPI may be better suited for balanced SSFP than interleaved spiral. The gradient trajectories of consecutive EPI segments are more similar than those of consecutive spiral interleaves[1], and should result in more consistent eddy currents (Fig. 8.2). EPI may permit higher duty-cycle and SNR for both balanced and alternating SSFP acquisitions.

8.1.3 Acceleration

Alternating SSFP is compatible with the most common MR image acquisition acceleration techniques, namely parallel imaging [80–82] and compressed sensing [83].

Parallel imaging and compressed sensing both permit the reconstruction of MR images from undersampled **k**-space data. Parallel imaging requires multiple receiver coils that have different spatial sensitivity patterns. The spatial information inherent

[1] particularly for **k**-space acquisitions having 4 or less segments

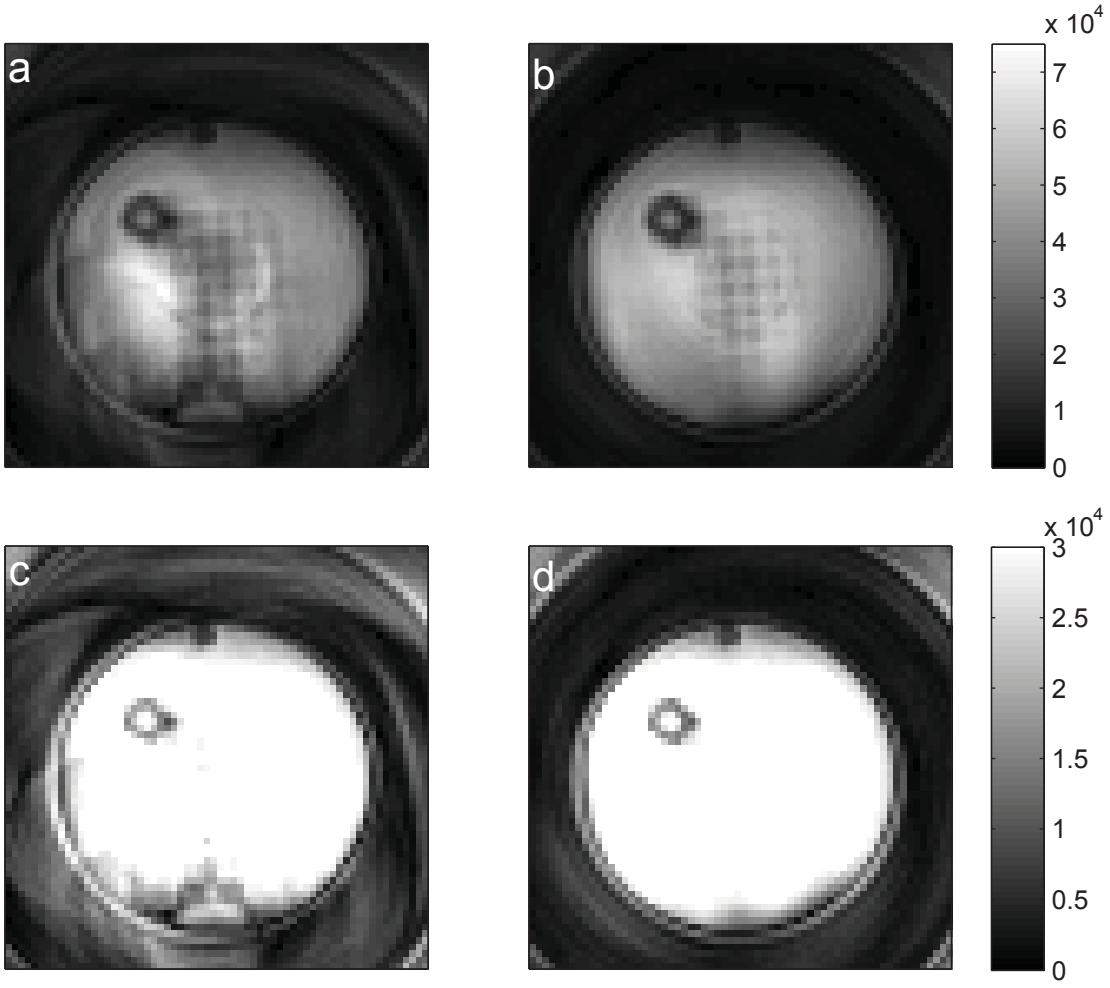

Figure 8.1: (a) 4-shot pass-band SSFP image ($T_E = 1.0$ ms, $T_R = 10.1$ ms, $\alpha = 70°$, 4 spiral interleaves, FOV = 240x240x80 mm^3, matrix = 64x64x32, 1.5 s/image volume). **k**-space was acquired with spiral interleaves as the inner loop and z phase-encodes as the outer loop. (b) fabricated 4-shot pass-band SSFP image. Matched acquisition parameters to (a), except that the same spiral interleave was acquired every T_R cycle. The image acquisition was repeated four times, once for each spiral interleave. The **k**-space data from the four acquisitions was then combined to produce a fabricated acquisition free from eddy current artifacts associated with cycling between spiral interleaves. Note that no averaging was performed (i.e., only 1/4 of the data from the four images was used). (c) and (d) show images (a) and (b), respectively, at low window and level (matched) to highlight signal displaced outside of the object.

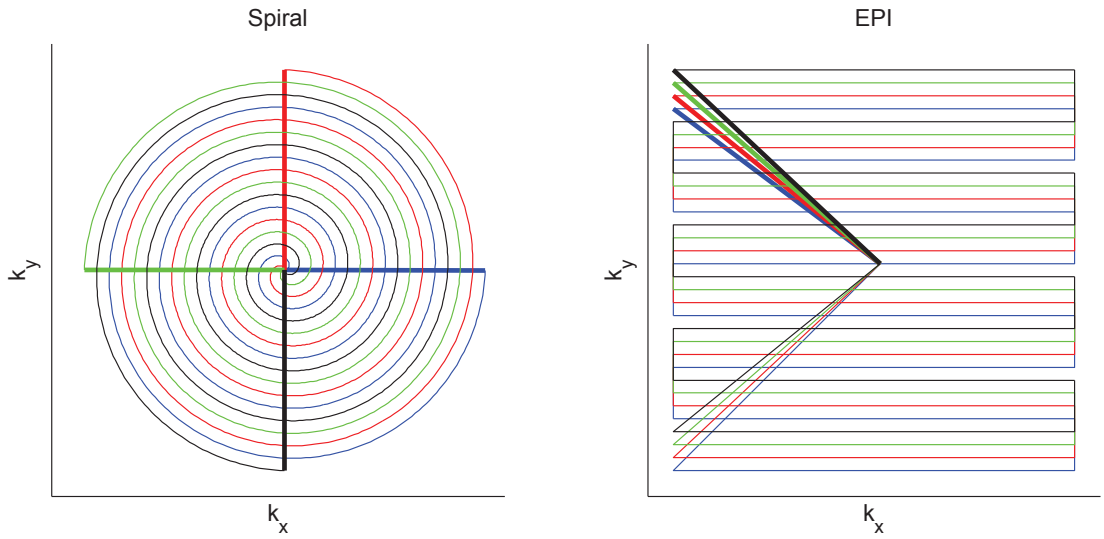

Figure 8.2: 4-shot spiral and EPI **k**-space trajectories. The return to the centre of **k**-space for each shot is highlighted (thick line). The direction of the applied gradient needed to return to the centre of **k**-space differs more between shots for spiral than for EPI.

in the coil sensitivity patterns is taken advantage of to reduce the amount of **k**-space data needed to reconstruct an image[2]. Compressed sensing is a signal-processing-based acceleration technique that, unlike parallel imaging, does not require specialized hardware. Compressed sensing takes advantage of the sparsity[3] of many MR images to constrain the (otherwise underdetermined) undersampled image reconstruction problem.

It should be noted that acceleration would be best-applied to alternating SSFP for the purpose of increasing spatial resolution or spatial coverage, rather than reducing the image volume acquisition time. This is because alternating SSFP BOLD contrast is suppressed following RF catalyzation, and sufficient time must be allowed for BOLD contrast to recover before encoding low-spatial-frequency image information or BOLD sensitivity will be sacrificed.

[2]by up to a factor equal to the number of receiver coils
[3]in the image domain or in a transform domain such as wavelet coefficients

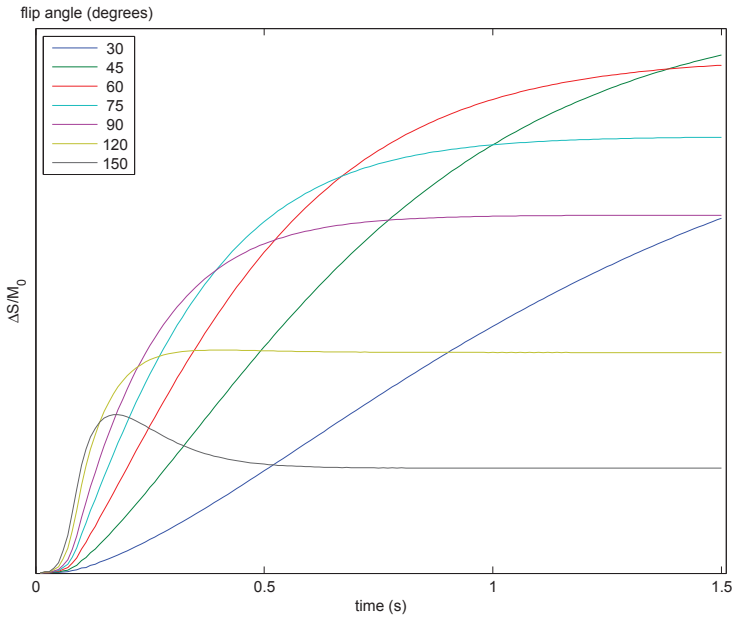

Figure 8.3: Bloch-simulated alternating SSFP BOLD contrast growth in the pass-band centre (T_R = 10 ms, $T_E = T_R/2$, T_{vol} = 3 s, T_1 = 1400 ms, T_2 = 70 ms, ΔR_2 = -.5s^{-1}). Alternating SSFP BOLD contrast recovers more quickly, early on, at high flip angle, but peaks at the **k**-space centre (t = 1.5 s) for $\alpha \approx 45°$.

8.1.4 BOLD contrast maximization with a variable flip angle scheme

We found alternating SSFP BOLD contrast to recover more quickly, early on, at high flip angle (Fig. 8.3). However, peak BOLD contrast at the **k**-space centre occurred for $\alpha \approx 45°$. Previous work has used a variable flip angle scheme to maximize the area under the balanced SSFP signal vs. time curve [84]. It may be possible to use a similar approach to maximize alternating SSFP BOLD contrast. High flip angles could be used early in the RF train to accelerate BOLD contrast recovery. Flip angles could be tapered to 45° later in the RF train to avoid plateauing at reduced BOLD sensitivity.

8.2 Conclusion

This work has developed a new pulse sequence, alternating SSFP, and demonstrated its ability to provide rapid, banding-artifact-free balanced SSFP fMRI. Alternating SSFP permits the consecutive acquisition of 0°- and 180°-RF-phase-cycled balanced SSFP images, with the pass-band of each image having 80 % of the BOLD sensitivity

found in full steady state (conventional balanced SSFP). These images can then be combined to produce whole-brain, banding-artifact-free balanced SSFP fMRI from a single paradigm run with 3 s temporal resolution. Previous whole-brain balanced SSFP fMRI applications required two runs of the functional paradigm, resulting in prohibitive temporal resolution. Alternating SSFP removes this restriction, providing a temporal resolution comparable to that of GRE-EPI.

Alternating SSFP may allow functional MRI in SFG regions not possible with GRE acquisitions, due to signal dropout, and SE acquisitions, due to low BOLD sensitivity. However, we found reduced BOLD sensitivity for alternating SSFP compared to GRE acquisitions, and future work is needed to determine if alternating SSFP performs better than spin-echo methods (which also eliminate signal dropout at the expense of reduced BOLD sensitivity relative to GRE). Nevertheless, the BOLD sensitivity achievable with alternating SSFP may be higher than reported here. In particular, the alternating SSFP readout duty-cycle was limited to one-half of its maximum value by eddy-current artifacts. Eddy-current mitigation through alternate **k**-space trajectories and/or improved compensation strategies have the potential to double the image acquisition rate, providing an expected $\sqrt{2}$-increase in BOLD sensitivity.

Appendix A

A.1 Alternating SSFP Contrast Growth

Alternating SSFP BOLD contrast is given by the difference in signal (Eq. 4.2) between active (subscript A) and resting (subscript R) states

$$\begin{aligned}\Delta S &= S_A - S_R \\ &= \Delta S_{stst} - \exp(-R^*_{1,R}t)(S_{stst,A}\exp(-\Delta R_2 \sin^2(\alpha/2)t) - S_{stst,R})\end{aligned} \tag{A.1}$$

where ΔS_{stst} is the steady state contrast level ($S_{stst,A} - S_{stst,R}$), and the active and resting R_1^* ($R_1^* = 1/T_1^*$) relaxation rates are given by

$$\begin{aligned}R^*_{1,R} &= R_1 \cos^2(\alpha/2) + R_2 \sin^2(\alpha/2) \\ R^*_{1,A} &= R^*_{1,R} + \Delta R_2 \sin^2(\alpha/2)\end{aligned} \tag{A.2}$$

For $|\Delta R_2| \sin^2(\alpha/2)t << 1$[1] , Eq. A.1 can be approximated as

$$\begin{aligned}\Delta S &\approx \Delta S_{stst} - \exp(-R^*_{1,R}t)(S_{stst,A}(1 - \Delta R_2 \sin^2(\alpha/2)t) - S_{stst,R}) \\ &= \Delta S_{stst}(1 - \exp(-R^*_{1,R}t)) - \exp(-R^*_{1,R}t)S_{stst,A}(-\Delta R_2 \sin^2(\alpha/2)t)\end{aligned} \tag{A.3}$$

Equation 4.4 follows from Eq. A.3 with $1/T_1^* = R^*_{1,R}$ and $S_{stst} = S_{stst,A} \approx S_{stst,R}$.

[1] Actually this restriction on t is overly conservative. Equation A.3 is derived using the approximation $\exp(-\Delta R_2 \sin^2(\alpha/2)t) \approx 1 - \Delta R_2 \sin^2(\alpha/2)t$, but it holds for large t as well because the $\exp(-R^*_{1,R}t)$ term goes to zero with t faster than the error grows with t in the above approximation.

Bibliography

[1] Ed Bullmore. The future of functional MRI in clinical medicine. *Neuroimage*, 62(2):1267–1271, 2012.

[2] Massachusetts General Hospital. Brain anatomy. `http://www2.massgeneral.org/livingwithtsc/affects/brain-popup_anatomy.htm`, 2013. Online; accessed 24-October-2013.

[3] J Michael Tyszka and Adam N Mamelak. Quantification of B_0 homogeneity variation with head pitch by registered three-dimensional field mapping. *Journal of Magnetic Resonance*, 159(2):213–218, 2002.

[4] Jin Hyung Lee, Serge O Dumoulin, Emine U Saritas, Gary H Glover, Brian A Wandell, Dwight G Nishimura, and John M Pauly. Full-brain coverage and high-resolution imaging capabilities of passband b-SSFP fMRI at 3T. *Magnetic Resonance in Medicine*, 59(5):1099–1110, 2008.

[5] Song Lai and Gary H Glover. Three-dimensional spiral fMRI technique: A comparison with 2D spiral acquisition. *Magnetic resonance in medicine*, 39(1):68–78, 1998.

[6] Gary H Glover et al. 3D z-shim method for reduction of susceptibility effects in BOLD fMRI. *Magnetic Resonance in Medicine*, 42(2):290–299, 1999.

[7] Karla L Miller, Stephen M Smith, Peter Jezzard, Graham C Wiggins, and Christopher J Wiggins. Signal and noise characteristics of SSFP FMRI: a comparison with GRE at multiple field strengths. *Neuroimage*, 37(4):1227–1236, 2007.

[8] Qing X Yang, Bernard J Dardzinski, Shizhe Li, Paul J Eslinger, and Michael B Smith. Multi-gradient echo with susceptibility inhomogeneity compensation (mgesic): Demonstration of fMRI in the olfactory cortex at 3.0 T. *Magnetic resonance in medicine*, 37(3):331–335, 1997.

[9] Qing X Yang, Gerald D Williams, Roger J Demeure, Timothy J Mosher, and Michael B Smith. Removal of local field gradient artifacts in T_2^*-weighted images at high fields by gradient-echo slice excitation profile imaging. *Magnetic resonance in medicine*, 39(3):402–409, 1998.

[10] ZH Cho and YM Ro. Reduction of susceptibility artifact in gradient-echo imaging. *Magnetic resonance in medicine*, 23(1):193–200, 1992.

[11] Nan-kuei Chen and Alice M Wyrwicz. Removal of intravoxel dephasing artifact in gradient-echo images using a field-map based RF refocusing technique. *Magnetic resonance in medicine*, 42(4):807–812, 1999.

[12] V Andrew Stenger, Fernando E Boada, and Douglas C Noll. Three-dimensional tailored RF pulses for the reduction of susceptibility artifacts in T_2^*-weighted functional MRI. *Magnetic resonance in medicine*, 44(4):525–531, 2000.

[13] Chun-yu Yip, Jeffrey A Fessler, and Douglas C Noll. Advanced three-dimensional tailored RF pulse for signal recovery in T_2^*-weighted functional magnetic resonance imaging. *Magnetic resonance in medicine*, 56(5):1050–1059, 2006.

[14] Hai Zheng, Tiejun Zhao, Yongxian Qian, Claudiu Schirda, Tamer S Ibrahim, and Fernando E Boada. Multi-slice parallel transmission three-dimensional tailored RF (PTX 3DTRF) pulse design for signal recovery in ultra high field functional MRI. *Journal of Magnetic Resonance*, 228:37–44, 2013.

[15] David G Norris. Principles of magnetic resonance assessment of brain function. *Journal of Magnetic Resonance Imaging*, 23(6):794–807, 2006.

[16] David G Norris. Spin-echo fMRI: The poor relation? *Neuroimage*, 62(2):1109–1115, 2012.

[17] CV Bowen, RS Menon, and JS Gati. High field balanced-SSFP fMRI: a BOLD technique with excellent tissue sensitivity and superior large vessel suppression. In *Proceedings of the 13th Annual Meeting of ISMRM, Miami Beach, FL, USA*, page 119, 2005.

[18] Karla L Miller. FMRI using balanced steady-state free precession (SSFP). *NeuroImage*, 62(2):713–719, 2012.

[19] M Deimling and O Heid. Magnetization prepared true FISP imaging. In *Proceedings of the 2nd Annual Meeting of ISMRM, San Francisco*, page 495, 1994.

[20] Brian A Hargreaves, Shreyas S Vasanawala, John M Pauly, and Dwight G Nishimura. Characterization and reduction of the transient response in steady-state MR imaging. *Magnetic resonance in medicine*, 46(1):149–158, 2001.

[21] Vibhas S Deshpande, Yiu-Cho Chung, Qiang Zhang, Steven M Shea, and Debiao Li. Reduction of transient signal oscillations in true-FISP using a linear flip angle series magnetization preparation. *Magnetic resonance in medicine*, 49(1):151–157, 2003.

[22] Karla L Miller and Peter Jezzard. Modeling SSFP functional MRI contrast in the brain. *Magnetic Resonance in Medicine*, 60(3):661–673, 2008.

[23] Taek Soo Kim, Jongho Lee, Jin Hyung Lee, Gary H Glover, and John M Pauly. Analysis of the BOLD characteristics in pass-band bSSFP fMRI. *International journal of imaging systems and technology*, 22(1):23–32, 2012.

[24] Jerrold L Boxerman, Leena M Hamberg, Bruce R Rosen, and Robert M Weisskoff. MR contrast due to intravascular magnetic susceptibility perturbations. *Magnetic Resonance in Medicine*, 34(4):555–566, 1995.

[25] E Mark Haacke, Robert W Brown, Michael R Thompson, and Ramesh Venkatesan. *Magnetic resonance imaging: physical principles and sequence design*, volume 1. Wiley-Liss New York:, 1999.

[26] Paul T. Callaghan. *Principles of nuclear magnetic resonance microscopy*. Oxford University Press, 1993.

[27] Nicolaas Bloembergen, Edward Mills Purcell, and Robert V Pound. Relaxation effects in nuclear magnetic resonance absorption. *Physical Review*, 73(7):679, 1948.

[28] John Pauly, Patrick Le Roux, Dwight Nishimura, and Albert Macovski. Parameter relations for the Shinnar-Le Roux selective excitation pulse design algorithm [NMR imaging]. *Medical Imaging, IEEE Transactions on*, 10(1):53–65, 1991.

[29] David G Norris. High field human imaging. *Journal of Magnetic Resonance Imaging*, 18(5):519–529, 2003.

[30] Ray Freeman and HDW Hill. Phase and intensity anomalies in Fourier transform NMR. *Journal of Magnetic Resonance (1969)*, 4(3):366–383, 1971.

[31] Klaus Scheffler. On the transient phase of balanced SSFP sequences. *Magnetic resonance in medicine*, 49(4):781–783, 2003.

[32] Patrick Le Roux. Simplified model and stabilization of SSFP sequences. *Journal of Magnetic Resonance*, 163(1):23–37, 2003.

[33] Peter Jezzard, Paul M Matthews, and Stephen M Smith. *Functional MRI an introduction to methods*. Oxford University Press, 2001.

[34] Richard B Buxton and Lawrence R Frank. A model for the coupling between cerebral blood flow and oxygen metabolism during neural stimulation. *Journal of Cerebral Blood Flow & Metabolism*, 17(1):64–72, 1997.

[35] CT Crit TW Moonen and P Peter A Bandettini. *Functional MRI*. Springer Verlag, 2000.

[36] Timothy Q Duong, Essa Yacoub, Gregory Adriany, Xiaoping Hu, Kâmil Uurbil, and Seong-Gi Kim. Microvascular BOLD contribution at 4 and 7 T in the human brain: Gradient-echo and spin-echo fMRI with suppression of blood effects. *Magnetic resonance in medicine*, 49(6):1019–1027, 2003.

[37] KJ Friston, P Jezzard, and R Turner. Analysis of functional MRI time-series. *Human Brain Mapping*, 1(2):153–171, 1994.

[38] PA Bandettini and RW Cox. Contrast in single trial fMRI: interstimulus interval dependency and comparison with blocked strategies. In *Proceedings of the ISMRM 6th Annual Meeting, Sydney*, page 161, 1998.

[39] RL Savoy, PA Bandettini, KM OCraven, KK Kwong, TL Davis, JR Baker, RM Weisskoff, and BR Rosen. Pushing the temporal resolution of fMRI: Studies of very brief visual stimuli, onset variability and asynchrony, and stimulus-correlated changes in noise. In *Program of SMR presented at 3rd Annual Meeting, Nice, France*, 1995.

[40] Adrian T Lee, Gary H Glover, and Craig H Meyer. Discrimination of large venous vessels in time-course spiral blood-oxygen-level-dependent magnetic-resonance functional neuroimaging. *Magnetic Resonance in Medicine*, 33(6):745–754, 1995.

[41] Peter A Bandettini and Eric C Wong. Effects of biophysical and physiologic parameters on brain activation-induced R2* and R2 changes: Simulations using a deterministic diffusion model. *International Journal of Imaging Systems and Technology*, 6(2-3):133–152, 1995.

[42] Peter A Bandettini and Eric C Wong. Magnetic resonance imaging of human brain function: principles, practicalities, and possibilities. *Neurosurgery Clinics of North America*, 8(3):345, 1997.

[43] ZS Saad, KM Ropella, GJ Carman, and EA DeYoe. Temporal phase variation of FMR signals in vasculature versus parenchyma. In *Proc Soc Magn Reson Med. New York, New York*, volume 1, page 1834, 1996.

[44] Dov Malonek and Amiram Grinvald. Interactions between electrical activity and cortical microcirculation revealed by imaging spectroscopy: Implications for functional brian mapping. *Science*, 272:551–554, 1996.

[45] Anna Devor, Istvan Ulbert, Andrew K Dunn, Suresh N Narayanan, Stephanie R Jones, Mark L Andermann, David A Boas, and Anders M Dale. Coupling of the cortical hemodynamic response to cortical and thalamic neuronal activity. *Proceedings of the National Academy of Sciences of the United States of America*, 102(10):3822–3827, 2005.

[46] Stephen A Engel, Gary H Glover, and Brian A Wandell. Retinotopic organization in human visual cortex and the spatial precision of functional MRI. *Cerebral cortex*, 7(2):181–192, 1997.

[47] Ravi S Menon, Seiji Ogawa, John P Strupp, and Kâmil Uurbil. Ocular dominance in human V1 demonstrated by functional magnetic resonance imaging. *Journal of Neurophysiology*, 77(5):2780–2787, 1997.

[48] Jerrold L Boxerman, Peter A Bandettini, Kenneth K Kwong, John R Baker, Timothy L Davis, Bruce R Rosen, and Robert M Weisskoff. The intravascular contribution to fmri signal change: monte carlo modeling and diffusion-weighted studies in vivo. *Magnetic Resonance in Medicine*, 34(1):4–10, 1995.

[49] S Ogawa, RS Menon, DW Tank, SG Kim, H Merkle, JM Ellermann, and K Ugurbil. Functional brain mapping by blood oxygenation level-dependent contrast magnetic resonance imaging. A comparison of signal characteristics with a biophysical model. *Biophysical Journal*, 64(3):803–812, 1993.

[50] Dmitriy A Yablonskiy and E Mark Haacke. Theory of NMR signal behavior in magnetically inhomogeneous tissues: the static dephasing regime. *Magnetic Resonance in Medicine*, 32(6):749–763, 1994.

[51] Klaus Scheffler, Erich Seifritz, Deniz Bilecen, Ramesh Venkatesan, Jürgen Hennig, Michael Deimling, and E Mark Haacke. Detection of BOLD changes by means of a frequency-sensitive trueFISP technique: preliminary results. *NMR in Biomedicine*, 14(7-8):490–496, 2001.

[52] Karla L Miller, Brian A Hargreaves, Jongho Lee, David Ress, R Christopher deCharms, and John M Pauly. Functional brain imaging using a blood oxygenation sensitive steady state. *Magnetic resonance in medicine*, 50(4):675–683, 2003.

[53] Karla L Miller, Stephen M Smith, Peter Jezzard, and John M Pauly. High-resolution FMRI at 1.5 T using balanced SSFP. *Magnetic resonance in medicine*, 55(1):161–170, 2006.

[54] Jon-Fredrik Nielsen, Daehyun Yoon, and Douglas C Noll. Small-tip fast recovery imaging using non-slice-selective tailored tip-up pulses and radiofrequency-spoiling. *Magnetic Resonance in Medicine*, 2012.

[55] Hao Sun, Jeffrey A Fessler, Douglas C Noll, and Jon-Fredrik Nielsen. Strategies for improved 3D small-tip fast recovery imaging. *Magnetic Resonance in Medicine*, 2013.

[56] Klaus Scheffler, Oliver Heid, and Jürgen Hennig. Magnetization preparation during the steady state: Fat-saturated 3D TrueFISP. *Magnetic resonance in medicine*, 45(6):1075–1080, 2001.

[57] Rohan Dharmakumar, Xiuling Qi, Juimiin Hong, and Graham A Wright. Detecting microcirculatory changes in blood oxygen state with steady-state free precession imaging. *Magnetic resonance in medicine*, 55(6):1372–1380, 2006.

[58] Rohan Dharmakumar, Juimiin Hong, Jean H Brittain, Donald B Plewes, and Graham A Wright. Oxygen-sensitive contrast in blood for steady-state free precession imaging. *Magnetic resonance in medicine*, 53(3):574–583, 2005.

[59] Paul A Bottomley, Thomas H Foster, Raymond E Argersinger, and Leah M Pfeifer. A review of normal tissue hydrogen NMR relaxation times and relaxation mechanisms from 1-100 MHz: dependence on tissue type, NMR frequency, temperature, species, excision, and age. *Medical physics*, 11:425, 1984.

[60] Helmut W Fischer, Peter A Rinck, Yves van Haverbeke, and Robert N Muller. Nuclear relaxation of human brain gray and white matter: analysis of field dependence and implications for MRI. *Magnetic resonance in medicine*, 16(2):317–334, 1990.

[61] Jiongjiong Wang, David C Alsop, Lin Li, John Listerud, Julio B Gonzalez-At, Mitchell D Schnall, and John A Detre. Comparison of quantitative perfusion imaging using arterial spin labeling at 1.5 and 4.0 tesla. *Magnetic Resonance in Medicine*, 48(2):242–254, 2002.

[62] JW Casselman, R Kuhweide, M Deimling, Willy Ampe, Idesbald Dehaene, and Luc Meeus. Constructive interference in steady state-3DFT MR imaging of the inner ear and cerebellopontine angle. *American journal of neuroradiology*, 14(1):47–57, 1993.

[63] Neal K Bangerter, Brian A Hargreaves, Shreyas S Vasanawala, John M Pauly, Garry E Gold, and Dwight G Nishimura. Analysis of multiple-acquisition SSFP. *Magnetic resonance in medicine*, 51(5):1038–1047, 2004.

[64] O Bieri and K Scheffler. Effect of diffusion in inhomogeneous magnetic fields on balanced steady-state free precession. *NMR in Biomedicine*, 20(1):1–10, 2007.

[65] Peter Schmitt, Mark A Griswold, Peter M Jakob, Markus Kotas, Vikas Gulani, Michael Flentje, and Axel Haase. Inversion recovery TrueFISP: quantification of T_1, T_2, and spin density. *Magnetic resonance in medicine*, 51(4):661–667, 2004.

[66] O Bieri, M Markl, and K Scheffler. Analysis and compensation of eddy currents in balanced SSFP. *Magnetic resonance in medicine*, 54(1):129–137, 2005.

[67] Graham A Wright, Bob S Hu, and Albert Macovski. Estimating oxygen saturation of blood in vivo with MR imaging at 1.5 T. *Journal of Magnetic Resonance Imaging*, 1(3):275–283, 1991.

[68] Joanna K Huttunen, Olli Gröhn, and Markku Penttonen. Coupling between simultaneously recorded BOLD response and neuronal activity in the rat somatosensory cortex. *Neuroimage*, 39(2):775–785, 2008.

[69] Keith J Worsley and Karl J Friston. Analysis of fMRI time-series revisited-again. *Neuroimage*, 2(3):173–181, 1995.

[70] SJ Sawiak, NI Wood, GB Williams, AJ Morton, and TA Carpenter. SPMMouse: A new toolbox for SPM in the animal brain. In *Proc Intl Soc Mag Res Med*, volume 1086, 2009.

[71] Stephen M Smith, Mark Jenkinson, Mark W Woolrich, Christian F Beckmann, TE Behrens, Heidi Johansen-Berg, Peter R Bannister, Marilena De Luca, Ivana Drobnjak, David E Flitney, et al. Advances in functional and structural MR image analysis and implementation as FSL. *Neuroimage*, 23:S208, 2004.

[72] Mark W Woolrich, Brian D Ripley, Michael Brady, and Stephen M Smith. Temporal autocorrelation in univariate linear modeling of FMRI data. *Neuroimage*, 14(6):1370–1386, 2001.

[73] KJ Worsley. Statistical analysis of activation images. *Functional MRI: an introduction to methods*, 14:251–270, 2001.

[74] J. Ashburner and K.J. Friston. Image segmentation. In R.S.J. Frackowiak, K.J. Friston, C. Frith, R. Dolan, K.J. Friston, C.J. Price, S. Zeki, J. Ashburner, and W.D. Penny, editors, *Human Brain Function*. Academic Press, 2nd edition, 2003.

[75] SJ Sawiak, D Caprioli, E Merlo, D Theobald, BJ Everitt, TW Robbins, TA Carpenter, and JW Dalley. Voxel-based morphometry in assessing a rat model of impulsivity: agreement with targeted western blot analysis. In *Proceedings of the 17th Meeting of the ISMRM, Melbourne*, 2011.

[76] Mark Jenkinson and Stephen Smith. A global optimisation method for robust affine registration of brain images. *Medical image analysis*, 5(2):143–156, 2001.

[77] Mark Jenkinson, Peter Bannister, Michael Brady, and Stephen Smith. Improved optimization for the robust and accurate linear registration and motion correction of brain images. *Neuroimage*, 17(2):825–841, 2002.

[78] Richard D Hoge, Jeff Atkinson, Brad Gill, Gérard R Crelier, Sean Marrett, and G Bruce Pike. Investigation of BOLD signal dependence on cerebral blood flow and oxygen consumption: the deoxyhemoglobin dilution model. *Magnetic Resonance in Medicine*, 42(5):849–863, 1999.

[79] Jing Yuan, Bruno Madore, and Lawrence P Panych. Fat–water selective excitation in balanced steady-state free precession using short spatial–spectral RF pulses. *Journal of Magnetic Resonance*, 208(2):219–224, 2011.

[80] Daniel K Sodickson and Warren J Manning. Simultaneous acquisition of spatial harmonics (SMASH): fast imaging with radiofrequency coil arrays. *Magnetic Resonance in Medicine*, 38(4):591–603, 1997.

[81] Klaas P Pruessmann, Markus Weiger, Markus B Scheidegger, Peter Boesiger, et al. SENSE: sensitivity encoding for fast MRI. *Magnetic resonance in medicine*, 42(5):952–962, 1999.

[82] Mark A Griswold, Peter M Jakob, Robin M Heidemann, Mathias Nittka, Vladimir Jellus, Jianmin Wang, Berthold Kiefer, and Axel Haase. Generalized autocalibrating partially parallel acquisitions (GRAPPA). *Magnetic Resonance in Medicine*, 47(6):1202–1210, 2002.

[83] Michael Lustig, David Donoho, and John M Pauly. Sparse MRI: The application of compressed sensing for rapid MR imaging. *Magnetic resonance in medicine*, 58(6):1182–1195, 2007.

[84] Pauline W Worters and Brian A Hargreaves. Balanced SSFP transient imaging using variable flip angles for a predefined signal profile. *Magnetic Resonance in Medicine*, 64(5):1404–1412, 2010.